

**An Investigation into the Charge Storage Mechanism and Cycling
Performance of Mn_2O_3 as the Cathode Material for Zinc-ion Batteries**

by

Qingping Hou

A thesis submitted in partial fulfillment of the requirements for the degree of

Master of Science
in

CHEMICAL ENGINEERING

Department of Chemical and Materials Engineering
University of Alberta

© Qingping Hou, 2022

Abstract

There has been increasing research interest to develop next generation energy storage devices to replace or at least complement lithium-ion batteries (LIBs), because of their potential safety issues and resource deficiencies. Aqueous rechargeable zinc-ion batteries (ZIBs) are becoming one of the most promising alternatives because of their safe operation without risk of catching fire or exploding, cost competitiveness, eco-friendliness, high theoretical capacity, impressive long term cycling stability, and superior rate capability. Mn is one of the most abundant metals in the earth's crust. Mn oxide is widely used in various applications, such as deoxidization and desulfurization, catalysts and battery materials due in part to the multiple oxidation states (+2, +3, and +4) of Mn. For battery materials, the diversity of Mn oxide crystal structures and crystal phases allow Mn oxide to combine with other metal ions and store energy easily. Mn-based ZIB electrode materials have been widely studied and utilized for many years.

The purpose of this work is to synthesize high purity and highly crystalline Mn oxide and to use the synthesized Mn oxide to develop high performing cathode materials for ZIBs and investigate the discharge/charge mechanism behind the Mn oxide cathode materials. The first study is focused on synthesis of desired Mn oxide material. The synthesis method is based on the method used to fabricate cathode materials for LIBs and sodium-ion batteries (SIBs), established in the author's previously study. The Mn oxide precursor was obtained through precipitation of an acidic Mn sulfate solution reacting with a basic aqueous solution consisting of sodium hydroxide and ammonia with a fixed molar ratio under controlled temperature and pH conditions. The final product was formulated through high temperature calcination of the precursor precipitate. The final product was characterized using scanning electron microscopy (SEM), energy dispersive X-ray

spectroscopy (EDS), X-ray photoelectron spectroscopy (XPS), and X-ray diffraction (XRD). Depending on the calcination temperature, the final product was identified as hausmannite Mn_3O_4 , bixbyite Mn_2O_3 , or a mixture of Mn_3O_4 and Mn_2O_3 . Since the electrochemical performance and reaction mechanism of Mn_3O_4 as the cathode material in ZIBs was already studied by a previous group member, Arjun Dhiman, Mn_2O_3 was chosen for further study in this thesis.

The second study used the synthesized Mn_2O_3 as the cathode material for ZIBs with an emphasis on investigating the electrochemical performance and charge storage mechanism behind the material. The electrodes were prepared by uniformly spreading a slurry, containing Mn_2O_3 (70 wt%), acetylene carbon (20 wt%), and polyvinylidene fluoride (pVdF, 10 wt%) as the binder, onto a graphite carbon current collector. CR2032 coin cells were assembled in air using the Mn_2O_3 composite cathode, Zn foil as the anode, Whatman glass fiber paper (GF/D) as the separator, and 2 M ZnSO_4 with 0.2 M MnSO_4 aqueous solution as the electrolyte. Cyclic voltammetry (CV) and galvanostatic discharge–charge (GCD) profiles were obtained from 1 V to 1.9 V vs Zn/Zn^{2+} at multiple scan rates and current densities. The electrode delivered discharge capacities of 375, 341, 289, 205, 113, and 65 mAh/g at 50, 100, 200, 500, 1000, and 2000 mA/g, respectively. Through a combination of transmission electron microscopy (TEM), selected area electron diffraction (SAED), rotating ring-disk electrode (RRDE) measurements, atomic absorption spectroscopy (AAS), XRD, and multiple electrochemical testing methods, a mechanism involving conversion reactions is proposed for the Mn_2O_3 electrode.

Preface

This thesis is focused on the synthesis, characterization, and electrochemical testing of Mn_2O_3 for use as a cathode for ZIBs. It should be noted that the charge storage mechanism revealed by this work is the first of its kind in the literature related to Mn_2O_3 as a cathode material in ZIBs. The research is presented in Chapter 4 and Chapter 5, along with any supporting information for this work.

Chapter 4 summarizes the work involved in synthesizing high purity and highly crystalline Mn oxide. Chapter 5 summarizes the work done with the synthesized Mn_2O_3 for use as cathodes in ZIBs. Dr. Ivey performed the TEM analysis through this work and provided support with editing. Dr. Wendy Tran performed the RRDE test. Dr. Shiraz Merali performed the AAS tests. Chapter 6 includes a several tests for other Mn oxides synthesized via the method in Chapter 4. Chapter 7 concludes the work completed and provides future work and suggestions for utilizing Mn_2O_3 as the cathode material in ZIBs.

A version of Chapter 5 of this thesis has been submitted for publication as follows:

Chapter 5: Q. Hou, T. N. T. Tran, Z. Abedi, D. G. Ivey, An Investigation into the Charge Storage Mechanism and Cycling Performance of Mn_2O_3 as the Cathode Material for Zinc-ion Batteries, *Batteries and Supercaps*, submitted April 2022.

Dedication

I dedicate to my friends and parents who have helped to make me into a better person and a better man. I also want to thank my fiancée, Zhu Zhao, for unconditional love and support through all this time. Thank you so much.

Acknowledgements

First, I would like to thank my supervisor, Dr. Douglas Ivey, for his ongoing support, feedback, and encouragement throughout my whole time of study. I would like to thank him for his continuous support even though I delayed my project research for months. He is a great man and a perfect supervisor who guided me through my study and made me a better person.

I would like to thank all the Ivey Research Group members for their guidance, support, and friendship. I would like to thank Wendy Thuy, Zahra Abedi, Matthew Labbe, Mark Cui, and Maosen Zhao for their friendship and help with experiments.

I would like to thank Mr. Shiraz Merali and Dr. Anqiang He for their technical support and input.

I am grateful to Canada's Natural Sciences and Engineering Research Council (NSERC RGPIN-2018-04488) for research funding.

I would like to acknowledge the support of my family, friends, and my future wife for their continued support in all things. Without their support, I would not be able to pass through the global pandemic, COVID-19, easily.

Finally, I would like to thank all frontline medical staff and related faculty of the University of Alberta. Thank you for risking your life and time to protect us and give me the chance to finish my Master's studies.

Table of Contents

Chapter 1: Introduction	1
Chapter 2: Literature Review	3
2.1 Aqueous metal-ion battery	3
2.2 Aqueous zinc-ion battery	6
2.2.1 Cathode materials for aqueous Zin-ion batteries (aZIBs)	7
2.2.2 Anode materials for aZIBs	16
2.2.3 Electrolyte for aZIBs	18
2.3 Thesis research topic	19
2.3.1 Review of using Mn_2O_3 as cathode materials in aZIBs	19
2.3.2 Thesis objectives	21
Chapter 3: Electrochemical and Characterization methods	23
3.1 Galvanostatic charge-discharge (GCD)	23
3.2 Cyclic voltammetry (CV)	23
3.3 X-ray diffraction (XRD)	24
3.4 X-ray photoelectron spectroscopy (XPS)	24
3.5 Scanning electron microscopy (SEM) and energy dispersive x-ray spectroscopy (EDS)	25
3.6 Transmission electron microscopy (TEM)	26
3.7 Rotating disk electrode (RDE) and Rotating ring-disk electrode (RRDE)	27
3.8 Atomic absorption spectroscopy (AAS)	28
Chapter 4: Mn oxide synthesis	29
4.1 Synthesis method	29
4.2 Electrochemical performance of Mn_3O_4 as the cathode material of aZIBs	32

Chapter 5: Charge storage mechanism and cycling performance of Mn₂O₃ -----	35
5.1 Introduction -----	35
5.2 Experimental section -----	36
5.3 Results and discussion -----	37
5.3.1. Structure and morphology -----	37
5.3.2. Electrochemical performance -----	39
5.3.3 Mechanism investigation -----	42
5.4 Conclusion -----	60
5.5 Supporting information -----	61
Chapter 6: Conclusions and recommendations -----	71
6.1 Conclusion -----	69
6.1.1 Synthesis method and products -----	69
6.1.2 Charge storage mechanism and cycling performance of Mn ₂ O ₃ -----	69
6.2 Future works and recommendations -----	70
6.2.1 Synthesis method and products -----	70
6.2.2 An Investigation into the Charge Storage Mechanism and Cycling Performance of Mn ₂ O ₃ as the Cathode Material for Zinc-ion Batteries -----	70
References -----	72

List of Tables

Table 2.1. Common intercalation ionic radii [17] -----	4
Table 2.2. electrochemical performance comparison of previous studies of bixbyite Mn_2O_3 as the cathode for ZIBs -----	21
Table 2.3. Charge storage mechanism comparison of previous studies of bixbyite Mn_2O_3 as the cathode for ZIBs -----	21
Table 5.1. Battery cycling performance comparison for this work and previous studies of bixbyite Mn_2O_3 as the cathode in ZIBs -----	40
Table 5.2. Charge storage mechanism comparison for this work and previous studies of bixbyite Mn_2O_3 as the cathode for ZIBs -----	57

List of Figures

Figure 1.1 Schematic illustration of the electrochemical principle of aZIB [4]. -----	2
Figure 2.1. Mn oxide crystal structures: a) β -MnO ₂ ; b) R- MnO ₂ ; c) γ - MnO ₂ ; d) α - MnO ₂ ; e) romanechite-type MnO ₂ ; f) todorokite-type MnO ₂ ; g) δ - MnO ₂ (layered-type); h) λ - MnO ₂ (spinel-type) [44]. -----	8
Figure 2.2. Schematic illustration of Zn ²⁺ intercalation processes in γ -MnO ₂ [47]. -----	10
Figure 2.3. Schematic illustration of the proposed charge/discharge process for EMD [69]-----	14
Figure 2.4. Schematic illustration of the phenomena observed on Zn electrodes in (a) alkaline and (b) mild aqueous electrolytes. [79]. -----	17
Figure 2.5 Crystal structure of alpha-Mn ₂ O ₃ . -----	20
Figure 4.1 Illustration of material synthesise method. -----	29
Figure 4.2 XRD patterns of different calcination temperatures. -----	30
Figure 4.3 SEM image and EDS spectra of the Mn ₃ O ₄ powder after 400 °C calcination -----	31
Figure 4.4 SEM image and EDS spectra of the Mn ₂ O ₃ powder after 800 °C calcination -----	31
Figure 4.5. a) Cyclic Voltammetry(CV) results at 0.5mV/s scan rate of Mn ₃ O ₄ as cathode material. b) Enlarged CV oxidization peaks area at potential window of 1.5-1.7V. c) Enlarged CV reduction peaks area at potential window of 1.1-1.5V. d) GCD cycling test under an applied 30mA/g specific current density. e) Cell cyclability results at an applied specific current of 200mA/g. f) rate capability test results at various applied current densities. -----	33
Figure 5.1. Microstructural characterization for as fabricated Mn ₂ O ₃ . (a) XRD pattern; (b) XPS high-resolution Mn 3s spectrum; (c) SEM secondary electron (SE) image of Mn ₂ O ₃ powder; (d) STEM annular dark field (ADF) image, EDS maps for Mn and O, and SAED pattern from the particle shown. The electron diffraction pattern is close to a [221] zone axis for bixbyite. -----	38
Figure 5.2. (a) CV curves at 0.25 mV s ⁻¹ . (b) GCD curves at 50, 100, 200, 500, 1000, and 2000 mA/g. (c) Rate capability tests at 50, 100, 200, 500, 1000, and 2000 mA/g and then again at 100 and 50 mA/g. (d) Galvanostatic charge–discharge electrochemical performance at 500 mA/g for	

200 cycles. (e) Galvanostatic charge–discharge electrochemical performance at 2000 mA/g for 1100 cycles. ----- 41

Figure 5.3. (a) GCD curve for the 15th (discharge only) and 16th (charge and discharge) cycles at 200 mA/g. (b) XRD patterns of the cathode for the stages indicated in (a). (c) XRD patterns of the cathode for the discharge conditions in (b) for the 2-theta range of 30° to 50°; the patterns are further enlarged on the right displaying the 2-theta range of 32° to 54° making the (222) peak from Mn₂O₃ more visible. Note the (411) peak for Mn, which was used as an internal standard to quantify any Mn₂O₃ peak shifting. ----- 44

Figure 5.4 Ex-situ SEM images for the various stages shown in Fig. 5.3 during GCD at 200 mA/g. (a) Fully charged state of the 15th cycle; (b) before the first discharge plateau of the 15th cycle; (c) first discharge plateau of the 15th cycle; (d) turning point between the two discharge plateaus of the 15th cycle; (e) second discharge plateau of the 15th cycle; (f) after the second discharge plateau of the 15th cycle; (g) close to full discharge of the 15th cycle; (h) fully discharged state of the 15th cycle; (i) first charge plateau of the 16th cycle; (j) second charge plateau of the 16th cycle; (k) fully charged state of the 16th cycle; (l) fully discharged stage of the 16th cycle. ----- 45

Figure 5.5 Ex-situ STEM ADF images, EDS maps, overall EDS spectra and SAED patterns of the Mn₂O₃ electrode at different stages of discharge and charge: (a) First discharge plateau (position (c)) of the 15th cycle; (b) second discharge plateau (position (e)) of the 15th cycle; (c) fully discharged state of the 15th cycle (position (h)); (d) first charge plateau stage of the 16th cycle (position (i)); (e) fully charged stage of the 16th cycle (position (k)). Note that the C, H and Z labels for the diffraction patterns correspond to carbon, hetaerolite, and ZHS, respectively. ----- 49

Figure 5.6 XRD patterns of the cathode for 2-theta in the 80° to 85° range for the stages shown. ----- 52

Figure 5.7 Ex-situ STEM ADF image, EDS maps, overall EDS spectrum, SAED pattern, and HRTEM image of the electrode with a Ti current collector at position (d) (turning point) of discharge for the 15th cycle. ----- 53

Figure 5.8 Mn-Zn-H₂O Pourbaix diagram with ZnMn₂O₄ phase boundaries; redrawn from [105]. ----- 54

Figure 5.9 RRDE profile for the Mn_2O_3 electrode with a scan rate at 1 mV s^{-1} in $2 \text{ M ZnSO}_4 + 0.2 \text{ M MnSO}_4$ solution, stirred at 900 rpm with the Pt ring electrode maintained at $1.91 \text{ V vs Zn/Zn}^{2+}$. -----	56
Figure 5.10 AAS results showing the Mn concentration in the electrolyte after various battery cycles. -----	56
Figure 5.11 JCPDS 41-1442, Bixbyite Mn_2O_3 standard PDF card. -----	61
Figure 5.12 JCPDS 75-2078, graphitic carbon standard PDF card. -----	62
Figure 5.13 JCPDS 44-0673, $\text{ZHS} \cdot 4\text{H}_2\text{O}$ standard PDF card. -----	63
Figure 5.14 JCPDS 39-0689, $\text{ZHS} \cdot 3\text{H}_2\text{O}$ standard PDF card. -----	64
Figure 5.15 JCPDS 89-4252 Mn standard PDF card. -----	65
Figure 5.16 JCPDS 24-1113, hetaerolite ZnMn_2O_4 standard PDF card. -----	66
Figure 5.17 Indexing of the SAED pattern in Fig. 5.4a. -----	67
Figure 5.18 Ex-situ STEM ADF images, EDS maps, and SAED patterns of the electrode with a Ti current collector at different stages of discharge and charge: (a) Fully charged stage of the 16 th cycle (position a). (b) Fully discharged state of the 15 th cycle (position h). -----	68

List of Acronyms and Abbreviations

aLIB	Aqueous Lithium-ion Battery
aZIB	Aqueous Zinc-ion Battery
AAS	Atomic Absorption Spectroscopy
BF	Bright Field
BSE	Back Scattered Electron
CP	Carbon Paper
CuHCF	Copper Hexacyanoferrate
CV	Cyclic Voltammetry
DF	Dark Field
EDS	Energy Dispersive Spectroscopy
EELS	Electron Energy Loss Spectroscopy
GCD	Galvanostatic Charge and Discharge
HAADF	High Angle Annular Dark Field
HR-TEM	High Resolution Transmission Electron Microscopy
LIB	Lithium-ion Battery
LiTFSI	Bis(trifluoromethanesulfonyl)imide
MIB	Magnesium-ion Battery
Ni-MH	Nickel Metal-Hydride
Ni-Cd	Nickel Cadmium
PVDF	Polyvinylidene Fluoride
RDE	Rotating Disk Electrode
RRDE	Rotating Ring-disk Electrode
SAED	Selected Area Electron Diffraction
SE	Secondary Electron
SEM	Scanning Electron Microscopy
SHE	Standard Hydrogen Electrode
SIB	Sodium-ion Battery
STEM	Scanning Transmission Electron Microscopy

TEM	Transmission Electron Microscopy
XAS	X-ray Absorption Spectroscopy
XPS	X-ray Photoelectron Spectroscopy
XRD	X-ray Diffraction
ZIB	Zinc-ion Battery
ZHS	Zinc Hydroxide Sulfate

Chapter 1: Introduction

Easily exploitable traditional fossil fuels are being depleted and they contribute to the decline in air quality [1]. Therefore, it is imperative that efficient, new, clean, and sustainable energy options are found to replace traditional energy sources [2,3]. Batteries have been widely studied as energy devices that can convert chemical energy into electrical energy. Currently, the most widely used batteries or energy storage/conversion devices include LIBs [4], lead-acid batteries [5], nickel-cadmium batteries [6], and fuel cells [7]. The devices, mentioned above, all have some shortcomings, which limit their development. In the case of lithium-ion batteries, there is concern about the supply of lithium. Also, safety concerns, environmental problems, and the cost of electrode materials are other critical issues associated with lithium-ion batteries [8]. Lead-acid batteries have large volumes, low specific energy densities, poor cycle performance, and their own environmental problems [9]. Nickel-cadmium batteries have a memory effect and contribute to environmental pollution [10]. Other energy storage/conversion devices such as fuel cells are expensive and the current technology is not very mature [11]. As such, none of these batteries or energy storage/conversion devices can fully satisfy the requirements of a secondary battery.

Aqueous zinc-ion batteries (aZIBs), shown schematically in Fig. 1.1, have attracted researchers' attention due to their low cost, long life, and high safety. An aqueous secondary ion battery uses an aqueous solution as the electrolyte. The aqueous electrolyte is safe, easy to prepare, and has high ion conductivity. Therefore, aqueous secondary ion batteries are considered to be promising candidates for large-scale energy storage systems. During the past ten years, aqueous secondary ion batteries have received increasing attention for power grid applications and for wearable devices and biocompatibility [12,13].

This work aims to synthesize an alternative cathode material (Mn_2O_3) for aZIBs and analyze the electrochemical performance and energy storage mechanism(s) of the assembled aZIB cells. Detailed thesis motivation and objectives will be provided in Section 2.3.2. This thesis consists of 6 chapters, with Chapter 1 (current chapter) as the Introduction. A literature review of the aqueous metal-ion battery system, including pre-existing cathode materials for aZIBs (especially Mn-based cathode materials), common anode materials, and common aqueous electrolyte components, are discussed in Chapter 2. Brief summaries of all electrochemical and characterization techniques used in this work are provided in Chapter 3. A complete discussion of

the synthesis methods for the Mn oxides explored in this work, Mn_2O_3 and Mn_3O_4 , and the electrochemical performance of Mn_3O_4 are discussed in Chapter 4. The central component of the thesis work is a detailed investigation of the energy storage mechanism(s) and electrochemical performance of Mn_2O_3 as the cathode material for aZIBs, and is discussed in Chapter 5. Conclusions, future work suggestions, and recommendations for Mn_2O_3 as the cathode material of aZIBs will be provided in Chapter 6.

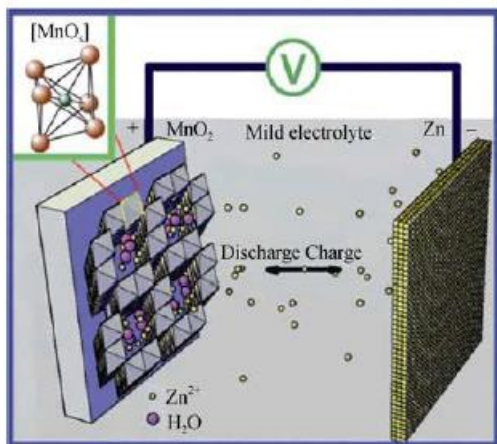


Figure 1.1 Schematic illustration of the electrochemical principle of an aZIB [4].

Chapter 2: Literature review

2.1 Aqueous metal-ion batteries

LIBs provide many conveniences for modern life [14,15], but their safety issues have become increasingly prominent. For example, in 2006, several Dell laptops caught fire and exploded. In 2013, several Tesla electric automobiles exploded after a collision and Samsung mobile phones caught fire and exploded [16]. One reason for potential accidents is that the organic electrolyte of commercial LIBs is flammable, which can lead to fires or even explosions. In order to prevent the occurrence of these events, researchers have tried to replace the flammable and explosive organic electrolytes with safer aqueous electrolytes. As such, aqueous secondary batteries have become a growing area of research. However, aqueous electrolytes have their own problems which hinder the development of aqueous batteries:

1. The electrochemical window of water is small ($\approx 1.23\text{V}$).
2. There are side reactions with water or oxygen.
3. Co-deposition of protons can occur along with the intercalation of metal ions.
4. Dissolution of electrode materials in aqueous electrolytes [17] can severely restrict the choice of electrode materials.

Thus far, most of the intercalation-type electrode materials used in aqueous batteries can be traced back to the corresponding organic electrolyte battery system. Aqueous lithium-ion batteries (aLIBs) have attracted a lot of attention due to their solid research foundation in organic electrolytes. Because of limited lithium reserves, researchers have gradually turned their attention to other metal-ion aqueous batteries because of abundant reserves of Na, K, Zn, Mg, Ca, and Al. Among these potential aqueous ion batteries, aZIBs have attracted much attention due to their higher theoretical specific capacity (820 mAh/g). The electrochemical performance of a battery is closely related to the ion radius for intercalation and extraction. Table 2.1 lists the radius of various metal ions.

The aLIB was first proposed by Dahn et al [18] of Dalhousie University in Canada in 1994. The battery uses LiMn_2O_4 as the cathode material, VO_2 as the anode material, and the electrolyte contains 5 mol/L LiNO_3 and 0.001 mol/L LiOH . By adjusting the concentration of LiOH in the

electrolyte so that the pH is 11, the hydrogen evolution potential is reduced, and the battery can function. Since 1994, aLIBs have attracted much attention. The stable voltage window of an aqueous electrolyte (~1.23 V) is much narrower than an organic electrolyte (>3.0 V) used in commercial LIBs. In 2015, Wang et al [19] reported a "water-in-salt" electrolyte, where the electrolyte was composed of 21 mol/kg of lithium bistrifluoromethanesulfonate (LiTFSI) in an aqueous solution, with LiMn_2O_4 as the cathode. The battery, assembled with Mo_6S_8 as the anode, had an open circuit voltage of 2.3 V and excellent cycle stability. The capacity retention rate was 68% for 100 cycles at a current density of 0.15 C, and the capacity retention rate reached 52% for 1000 cycles at a current density of 4.5 C. At the same time, the electrochemical stability window was expanded to about 3.0 V (1.9-4.9 V vs. Li^+/Li), which was a revolutionary advancement. Since then, research on aqueous LIBs has flourished. This electrolyte system provided new research ideas for aLIBs and other aqueous ion batteries.

Table 2.1. Common intercalation ionic radii [17]

Ion	Radius (nm)
Li^+	0.076
Na^+	0.102
K^+	0.138
Zn^{2+}	0.074
Mg^{2+}	0.072
Ca^{2+}	0.100
Al^{3+}	0.054

Sodium resources in the earth's crust are more abundant than lithium resources. Similar to aLIBs, research on aSIBs has also attracted significant attention. ASIBs use a sodium salt aqueous solution as the electrolyte to broaden the electrochemical window [20-22]. Wang et al [20] utilized a 0.26 mol/L NaCF_3SO_3 solution as the electrolyte and $\text{Na}_{0.66}[\text{Mn}_{0.66}\text{Ti}_{0.34}]\text{O}_2$ as the anode. The anode was assembled with $\text{NaTi}_2(\text{PO}_4)_3$ to form a full battery, showing excellent electrochemical performance. The Coulombic efficiency was as high as 99.2% at 0.2 C for 350 cycles. The power

density was 31 Wh/kg at a current density of 1 C. The capacity retention rate after 1500 cycles was 92.7%. Wu et al [23] synthesized $\text{NaTi}_2(\text{PO}_4)_3$ as an electrode material for aLIBs using a microwave method. The discharge specific capacity at a current density of 15.7 mA/g was 85 mAh/g, which is 64% of the theoretical specific capacity. The capacity decayed quickly. Subsequently, Wu et al [24] used $\text{NaTi}_2(\text{PO}_4)_3$ coated graphene as an aqueous sodium-ion battery (aSIB) cathode material and the discharge specific capacity was still as high as 130 mAh/g at 0.1 C and at 133 mA/g current density. The capacity retention rate after 100 cycles was 86%.

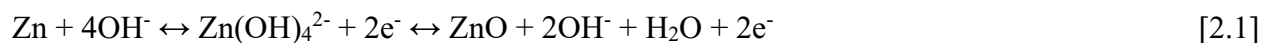
For aqueous potassium-ion batteries (aKIBs), the development of high-performance electrode materials is limited by the large ionization potential and the large radius of K^+ (0.138 nm). So far, the most valuable cathode materials for aKIBs are Prussian blue analogs [25-27]. Cui et al [25] conducted a comprehensive study, including copper hexacyanoferrate (CuHCF) and iron hexacyanoferrate (FeHCF). Among them, CuHCF showed good rate performance at 49.8 mA/g with specific capacity of 59.14 mAh/g and specific capacity of 40.1 mAh/g at 4980 mA/g current density. The cycling performance was good with a capacity retention rate of 83% after 40,000 cycles at 1020 mA/g current density and a Coulombic efficiency of 99.7% [25]. Generally, the discharge capacity of Prussian blue analogs is relatively low (<60 mAh/g). In 2016, Su et al [28] prepared potassium iron (II) hexacyanoferrate dehydrated nanocubes ($\text{K}_2\text{Fe}[\text{Fe}(\text{CN})_6] \cdot 2\text{H}_2\text{O}$), which have a high K^+ content, as the cathode material for aKIBs. With two single-electron redox processes, the compound exhibited a specific discharge capacity of up to 120 mAh/g.

Rechargeable non-aqueous magnesium-ion batteries (MIBs) have a low reduction potential (-2.37 V vs. SHE) and a large volumetric capacity (3833 mAh/cm³), which is higher than 2046 mAh/cm³ for lithium metal, due to its non-dendritic characteristics. The MIB has been considered as an up-and-coming energy storage/conversion battery system [29-32]. However, the development of non-aqueous MIBs is affected by the scarcity of electrolytes (humidity sensitivity, limited electrochemical stability, and strong corrosivity) and cathode materials (because of the slow diffusion of Mg^{2+} in the host material due to strong electrostatic interactions) [32-34]. As early as 1993, Novák et al [35-37] showed that the preferential solvation of Mg^{2+} by water molecules seemed to facilitate the intercalation of Mg^{2+} into V_2O_5 . However, until now, aqueous MIBs have not received much attention.

In summary, aqueous ion batteries have developed rapidly in recent years due to the advantages of safe use, low cost, and the use of aqueous solutions as electrolytes. ALIBs have higher energy density, but lithium resources are relatively scarce and other monovalent ion batteries have been proposed. However, compared with Li⁺, Na⁺ and K⁺ have a much larger ionic radius, and the interaction between the guest ion and the host skeleton hinders the reversible intercalation/extraction of the ion. Therefore, the number of electrode materials for sodium-ion and KIB is low. Among the multivalent metal-ion batteries, the aZIB has a higher energy density due to the high capacity of the metallic Zn anode. aZIBs are the most promising alternative to LIBs as the next generation of electrical energy storage equipment due to their electrolytes being inorganic salts, pollution-free, and safe. Research and development of other aqueous secondary batteries, such as magnesium-ion and calcium-ion batteries, are in the initial stages and the electrode materials used for these batteries are very limited.

2.2 Aqueous zinc-ion battery (aZIB)

The aZIB consists of a Zn anode (Section 2.2.2), an aqueous electrolyte (Section 2.2.3), and a cathode material that can storage and release, usually by intercalation and de-intercalation, Zn²⁺ (Section 2.2.1). The early aZIBs were assembled in aqueous alkaline electrolytes. The most common example is Ni-Zn batteries. Under alkaline electrolyte conditions, the battery is based on the Zn anode reaction [38]:



and the cathode reaction [39]:



The use of metallic Zn as the anode material is prone to producing dendrites under alkaline electrolyte conditions and the electrode hydrogen evolution reaction (HER) is significant. Zn is the metal with the lowest electrochemical reduction standard potential, -0.763 V, in aqueous solutions. Zn also is an active metal, which is stable in water and aqueous solutions, with a high energy density and high theoretical capacity (5855 mAh/cm³ and 820 mAh/g). In addition, Zn is abundant, has low toxicity, and can be processed simply. Therefore, a low cost, highly safe, environmentally friendly, and high power secondary aZIB is a promising replacement application in green battery system [40,41].

The electrolytes for aZIBs usually are usually mild aqueous solutions with low toxicity, low corrosion rates and are relatively safe; most of them are Zn-based weak acid solutions. In alkaline Zn batteries, the electrolyte usually contains a high concentration KOH solution. The formation of Zn dendrites and ZnO leads to severe capacity attenuation and lower Coulombic efficiency, which reduces the capacity of the Zn anode [42]. Also, strong acidic electrolytes will bring about the corrosion of the Zn anode and current collectors, resulting in poor long-term reliability [42]. Therefore, neutral or mildly acidic electrolytes seem preferable for implementation in ZIBs. The common Zn electrolyte salts studied so far include ZnSO_4 , $\text{Zn}(\text{NO}_3)_2$, $\text{Zn}(\text{CH}_3\text{COO})_2$, $\text{Zn}(\text{ClO}_4)_2$, and ZnCl_2 [43, 44, 45, 46, 47].

The process of assembling and disassembling aZIBs is fairly simple. The battery assembly process does not need the use a glove box. The costs for Zn metal and Zn salts are relatively low and the mild electrolyte solutions and non-toxic electrode materials are environmentally friendly. The above advantages have made the development of neutral aZIBs a global effort and have made ZIBs a strong possibility for large-scale electrical energy storage. Compared with the radius of Li^+ , the radius of Zn^{2+} (0.074 nm) is relatively small; however, it is not easy to find a suitable intercalation electrode material because the electrostatic interaction between Zn^{2+} and the cathode material is much larger than that for Li^+ . So far, research on aZIBs is still in its infancy.

2.2.1 Cathode Materials for aZIBs

The aZIB cathode materials mainly include Mn-based materials, vanadium-based materials, and Prussian blue analog materials.

As the tenth most abundant element in the earth's crust, Mn (Mn) is easily to find on the surface of the earth. During the past 150 years, Mn oxide has been widely used as a deoxidizer, desulfurizer, additives in steelmaking, catalysts, and electrode materials. Because Mn has multiple valence states (+2, +3, and +4), it has diverse crystal structures in oxide/hydroxide minerals. During the past 20 years, Mn-based oxides have been used in aZIBs. Examples include MnO , MnO_2 , Mn_2O_3 , and Mn_3O_4 .

Among these oxides, MnO_2 has been the most studied. MnO_2 has different crystal forms and the basic structural unit of Mn dioxide for all crystal forms is the $[\text{MnO}_6]$ octahedron. The

oxygen atoms occupy six corners of an octahedron, and the Mn atom is located in the center of the octahedron. MnO₆ octahedra are connected to each other by sharing vertices or sharing edges, leading to different crystal types of MnO₂, as shown in Fig. 2.1. Common MnO₂ cathode materials of ZIBs can be divided into three types of structures:

Tunnel-type: pyrolusite (β -MnO₂, 1*1 tunnel, Fig. 2.1a), rhombic ore (ramsdellite R-MnO₂, 1*2 tunnel, Fig. 2.1b), hexagonal Mn oxide (γ -MnO₂, 1*1 and 1*2 tunnels, Fig. 2.1c), fennelite (α -MnO₂, 2*2 tunnels, Fig. 2.1d), MnO₂ with romanechite structure (2*3 tunnels, Fig. 2.1e), and MnO₂ with todorokite structure (3*3 tunnels, Fig. 2.1f).

Layer-type: birnessite with layered structure (δ - MnO₂, Fig. 2.1g).

3-D-type: λ -MnO₂ with a three-dimensional structure (Fig. 2.1h).

These oxides, with different structures, are used as electrodes in aZIBs and exhibit different reaction mechanisms [48,49].

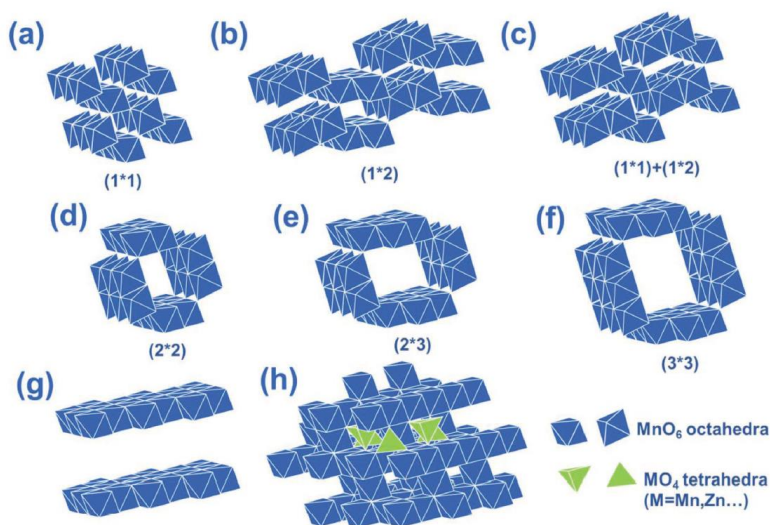


Figure 2.1. Mn oxide crystal structures: a) β -MnO₂; b) R-MnO₂; c) γ -MnO₂; d) α -MnO₂; e) romanechite-type MnO₂; f) todorokite-type MnO₂; g) δ -MnO₂ (layered-type); h) λ -MnO₂ (spinel-type) [49].

γ -MnO₂ was first used as a cathode material for ZIBs in 2003. Kumar et al [50] observed that Zn²⁺ ions from the Zn(CF₃SO₃)₂ gel polymer electrolyte could be reversibly intercalated/de-intercalated into the γ -MnO₂ tunnel structure. For aqueous electrolytes, such as Zn(NO₃)₂ or ZnSO₄

solutions, research results show that the reaction mechanism in alkaline electrolytes is H^+ intercalation into $\gamma\text{-MnO}_2$ [51]. Afraqi et al.'s work [52], proposed a novel charge storage mechanism for $\gamma\text{-MnO}_2$ in aZIBs. Data analysis from in-situ X-ray absorption spectroscopy (XAS) and in-situ synchrotron XRD, based on the near-edge structure, indicated that Mn^{4+} in MnO_2 was reduced to Mn^{3+} and Mn^{2+} during discharge. After charging the cell, the oxidation state of Mn returned to the original $\gamma\text{-MnO}_2$ state, which is Mn^{4+} . Spinel-type $ZnMn_2O_4$, tunnel type $\gamma\text{-Zn}_x\text{MnO}_2$ ($0 < x < 1$), and layered type $Zn_y\text{MnO}_2$ ($0 < y < 1$) were formed in sequence during the discharge process. These results indicated that Zn^{2+} intercalation into MnO_2 occurred, as shown in Fig. 2.2. Afraqi divided the discharge curve of $\gamma\text{-MnO}_2$ into three stages according to the data from in-situ tests; an early stage, an intermediate stage, and a final stage. During the early stage of the discharge process, part of the $\gamma\text{-MnO}_2$ transforms to spinel type $ZnMn_2O_4$. During the intermediate stage, in addition to further spinel type $ZnMn_2O_4$ formation, a tunnel type $\gamma\text{-Zn}_x\text{MnO}_2$ phase is formed due to Zn intercalation. In the final stage, a part of the fully inserted tunnel structure expands and folds into layered $Zn_y\text{MnO}_2$, so that the fully discharged material shows co-phases of spinel type, tunnel type, and layered type $ZnMnO_2$. After recharging the cell, almost all the above discharge co-phases are restored to the original $\gamma\text{-MnO}_2$, which indicates that Zn^{2+} can be reversibly inserted/extracted with 1*1 and 1*2 tunnel structure $\gamma\text{-MnO}_2$.

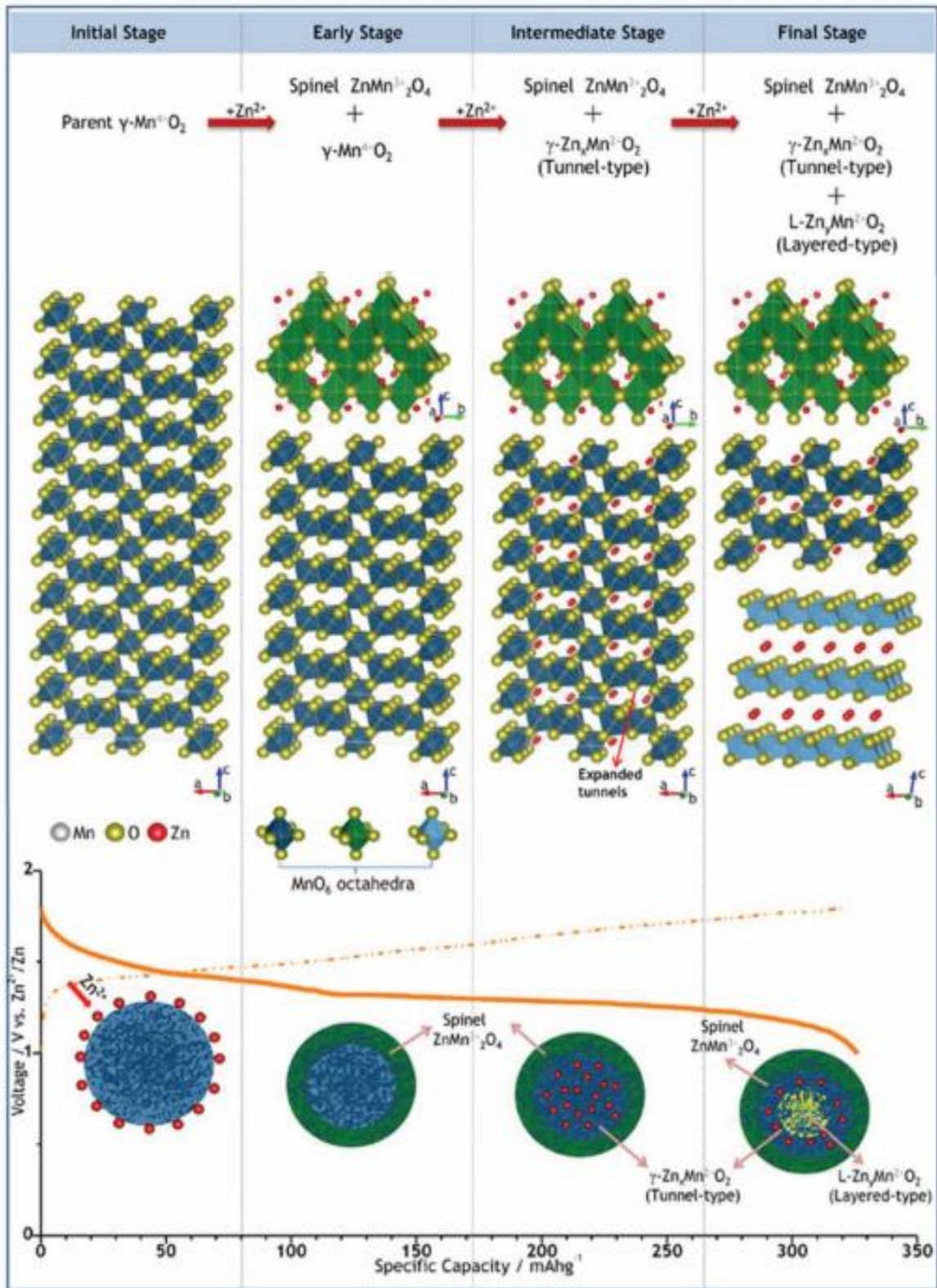


Figure 2.2. Schematic illustration of Zn^{2+} intercalation processes in $\gamma\text{-MnO}_2$ [52].

α -MnO₂ with 2*2 tunnels has received increasing interest as an electrode in aZIBs [53]. In 2009, α -MnO₂ was first applied to aZIBs and achieved a specific capacity of 210 mAh/g at 1 C. The C-rate is a measure of the rate at which a battery is discharged relative to its rated capacity. For example, a battery rated at 1 A-h, will deliver 1 A of current for 1 h, or the same battery will deliver 500 mA in 2 h. Compared with the theoretical capacity 616 mAh/g, the achieved specific capacity of the cell is fairly low. According to reference [54], due to the relatively large pores and stable structure of α -MnO₂ with 2*2 tunnels, the discharge capacity efficiency was maintained at almost 100% when it was cycled 100 times at a large current density of 6 C [55]. It was speculated that as the valence state of Mn decreases, Zn²⁺ is inserted into the cathode during the discharge process, according to Reaction 2.3. γ -MnO₂ also shares this reaction; however, the structure is different, resulting in the formation of a different phase of ZnMn₂O₄.



In this way, layered type ZnMn₂O₄ (Zn-birnessite) is formed during the discharge process and ZnMn₂O₄ disappears during the charging process, resulting in reformation of α -MnO₂. The reversibility between Mn⁴⁺ and Mn³⁺ has been verified by ex-situ synchrotron XAS [56], which showed that α -MnO₂ undergoes reversible intercalation and extraction of Zn²⁺. This kind of mechanism is defined as a (de)intercalation process.

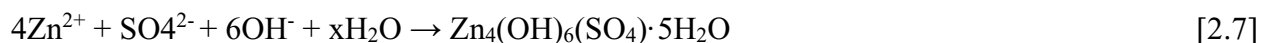
In subsequent studies, a Zn²⁺ intercalation mechanism was proposed as an electrochemical phase transformation with reversibility. A phase change from tunnel α -MnO₂ to a Zn-birnessite structure occurred [57]. During discharge, a layered structure ZnMn₃O₇·3H₂O, similar to Zn-birnessite, is formed [58]. During this reaction, due to the Jahn-Teller effect, about 1/3 of the Mn in the electrode is dissolved in the electrolyte. The discharge process is given in Reactions 2.4 and 2.5, but there is a complete reformation of α -MnO₂ after charging (Reaction 2.6).



Therefore, with the continuous intercalation of Zn²⁺, Mn⁴⁺ is reduced to Mn³⁺, and then, due to the dissolution of Mn²⁺ (Reaction 2.5), the bridged double strands of the MnO₆ unit are gradually

destroyed. In this process, a Zn-birnessite structure is formed. During the charging process, the dissolved Mn^{2+} can be deintercalated from the layered structure to produce the tunnel structure, and the structure of $\alpha\text{-MnO}_2$ is restored.

In addition to the previous Zn^{2+} intercalation reaction mechanism (Reaction 2.1), a reversible precipitation/dissolution conversion reaction mechanism based on $\text{Zn}_4(\text{OH})_6\text{SO}_4 \cdot x\text{H}_2\text{O}$ (Zn hydroxide sulfate or ZHS) formation has been proposed, which is generated from sulphate ions in the electrolyte, i.e., from ZnSO_4 (Reaction 2.7). The process is caused by a change in pH during the Mn dissolution reaction (Reaction 2.8) [59]. The $\text{Zn}_4(\text{OH})_6\text{SO}_4 \cdot x\text{H}_2\text{O}$ phase is considered as the discharge product. According to in-situ XRD and electrode characterization, it has been found that ZHS can be washed away by acetic acid during the discharge process, which indicates that this precipitate is formed on the surface of $\alpha\text{-MnO}_2$. There is no Zn^{2+} intercalation into the tunnels of $\alpha\text{-MnO}_2$. The utilization of atomic absorption spectroscopy (AAS) and in-situ pH measurement of the electrolyte further demonstrated that the precipitation process is reversible and triggered by pH changes in the electrolyte. Due to the Jahn-Teller effect, Mn^{3+} produced by MnO_2 (Reaction 2.2) is prone to disproportionation (Reaction 2.5) during the discharge process.



There is another explanation for ZHS formation, which involves H^+ intercalation with $\alpha\text{-MnO}_2$ (Reaction 2.10). Water splits to produce OH^- (Reaction 2.9), which further reacts with ZnSO_4 and water molecules to form ZHS (Reaction 2.8) [60]. In Pan's work, during discharge, the original $\alpha\text{-MnO}_2$ nanofibers are transformed into short nanorods and nanoparticle aggregates. The particles, after discharge, were identified as MnOOH by ex-situ high resolution transmission electron microscopy (HR-TEM) and XRD. ZHS was detected in the discharge electrode by nuclear magnetic resonance (NMR) spectroscopy and XRD, so that ZHS formation (Reaction 2.10) should occur after H^+ intercalation. After the charging process, the lattice spacings of the nanorods and nanoparticle aggregates are restored to the original $\alpha\text{-MnO}_2$ lattice spacings. These results indicate that there is a reversible discharge/charge behavior between $\alpha\text{-MnO}_2$ and MnOOH /ZHS.



It is worth noting that the XRD pattern for the ZHS phase has multiple peaks overlapping with the Zn-birnessite peaks reported above, and more analytical methods are needed to determine the mechanism of Zn^{2+} behavior in α - MnO_2 . Recently, in order to further explain the mechanism, cathode materials prepared based on $Zn_4(OH)_6SO_4 \cdot 5H_2O$ were studied [61]. In general, although the charge/discharge mechanism of α - MnO_2 is controversial, significant progress has been made in α - MnO_2 cathode materials. The development cost is low and operation is fast and straightforward, so that environmentally friendly α - MnO_2 may become a suitable cathode material [62].

For 3*3 tunnel type, todorokite-type, MnO_2 , because of the abundant tunnel spaces, various cations and water molecules can be easily accommodated in the host framework. Therefore, theoretically, the cycle performance and rate performance are better than those for traditional 2*2 tunnel structures. Lee et al [63] investigated todorokite MnO_2 as a potential cathode material in ZIBs. They studied the behavior of Zn^{2+} intercalated into the tunnel structure. In fact, the formation of large tunnels is usually through the expansion of MnO_6 layers and ion exchange. In addition, more ions and water molecules in the tunnels can ensure the stability of the structure during Zn ion intercalation and provide more space for Zn^{2+} migration. Unfortunately, XRD analysis of the discharge electrode has not been done in detail to explain the structural changes, and the mechanism of Zn^{2+} deintercalation is still unclear.

Work has also been done in Ivey's Research Group regarding the discharge/charge mechanisms of tunnel type MnO_2 . Tran et al [64] studied electrolytic manganese dioxide (EMD), which consists of 53% ϵ - MnO_2 , 34% ramsdellite, and 13% γ - MnO_2 . As mentioned above, ramsdellite (R- MnO_2) has a (1*2) tunnel structure, while both γ - MnO_2 and ϵ - MnO_2 have intergrown (1*1) and (1*2) tunnels from pyrolusite and ramsdellite, respectively. In general, ϵ - MnO_2 has a more disordered structure than γ - MnO_2 . RRDE studies, XRD, and SEM/TEM all revealed that aZIB cells utilizing EMD undergo a multi-step process during operation. Zn^{2+} ions are either intercalated to generate spinel-type $ZnMn_2O_4$ or inserted into MnO_2 tunnels to form tunnel-type Zn_xMnO_2 during discharge. When the saturation limit for Zn^{2+} intercalation in the MnO_2 tunnels ($Zn_{0.5}MnO_2$) is reached, $Zn_{0.5}MnO_2$ is disproportionated, resulting in the creation of zinc hydroxide sulphate (ZHS). Mn^{2+} ions, produced from disproportionation, are deposited electrochemically on hetaerolite to generate chalcophanite ($ZnMn_3O_7 \cdot 3H_2O$). During charging,

layered chalcophanite increasingly covers the electrode surface, whereas the initial ramsdellite amount of EMD vanishes during cycling. A schematic illustration of EMD cycling and the charge storage mechanism is shown in Fig. 2.3.

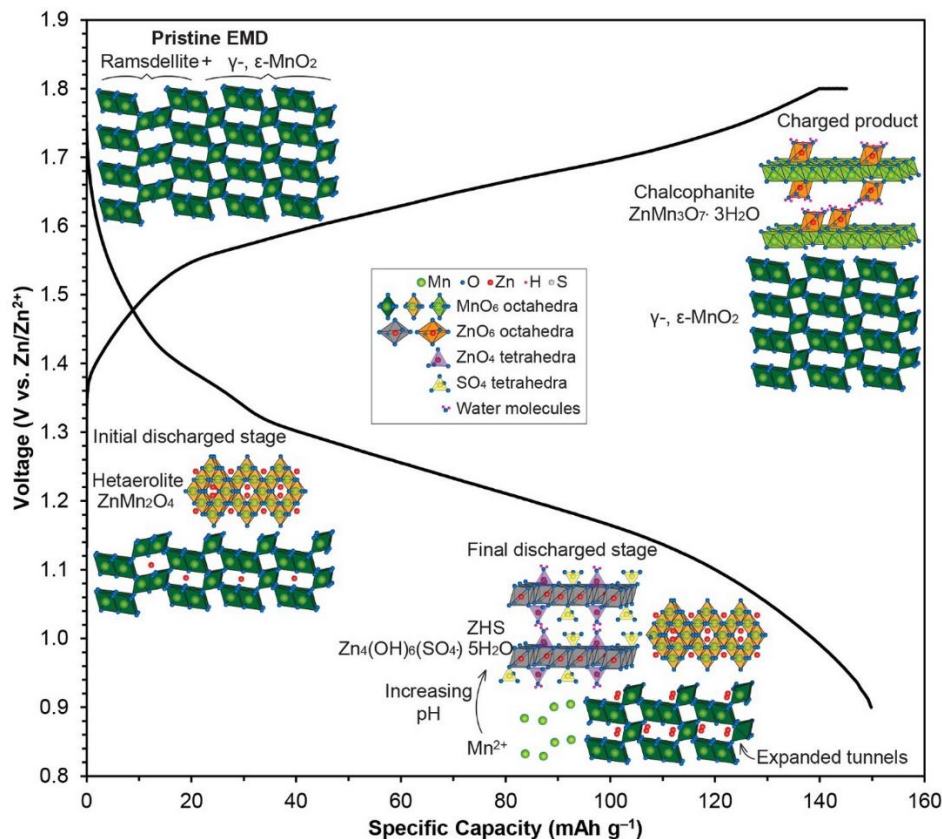


Figure 2.3. Schematic illustration of the proposed charge/discharge process for EMD. [64].

δ -MnO₂, with a layered structure and nanoflake morphology, has been synthesized and used in aqueous ZIBs. After the battery was discharged, spinel ZnMn₂O₄ appeared, and no other irreversible phases such as ZnO, MnOOH, Mn₃O₄, and Mn₂O₃ were detected. At the same time, a significant amount of Zn content (Zn:Mn = 0.59:1) was found in the electrode in the fully discharged state [65]. Therefore, it was concluded that part of the layered structure of δ -MnO₂ was transformed into spinel ZnMn₂O₄. Hydrated δ -MnO₂ (K_{0.11}MnO₂·0.7H₂O) has also been studied using non-aqueous electrolytes [66]. It is speculated that layered δ -MnO₂ has no proton participation in Zn²⁺ intercalation and can reversibly transform between MnO₂ and Zn_xMnO₂ (0 < x < 1). However, after long term cycling, fast capacity fade and cell resistance changes were observed, which could be due to the dissolution of Mn²⁺ by the Jahn-Teller effect, the

decomposition of electrolyte, and the precipitation of irreversible phases on the anode. These results make the reaction mechanism of Zn^{2+} in $\delta\text{-MnO}_2$ still unclear.

For the 3D spinel structure, $\lambda\text{-MnO}_2$, it is difficult for Zn^{2+} to be intercalated due to the limitation of its structure. The internal space of the structure is theoretically not suitable for the insertion of Zn^{2+} because of high electrostatic repulsion [55]. $\lambda\text{-MnO}_2$ synthesized by simply leaching LiMn_2O_4 had a specific capacity of 442.6 mAh/g at a current density of 13.8 mA/g [67], which is over 2/3 of the theoretical capacity of MnO_2 (616 mAh/g). According to Yuan et al [67], the intercalation of Zn^{2+} into $\lambda\text{-MnO}_2$ appears to be happening and the intercalation amount is high. However, the detailed intercalation mechanism is still not clear for $\lambda\text{-MnO}_2$. At the same time, spinel-type ZnMn_2O_4 and MnMn_2O_4 (Mn_3O_4) are being studied for aZIBs. Ideal spinel ZnMn_2O_4 (ZMO) does not appear to be suitable for Zn^{2+} intercalation because the electrostatic repulsion of Zn^{2+} in the crystal lattice is relatively large, so a Mn cation defect spinel ZMO ($\text{ZnMn}_{1.86}\text{Y}_{0.14}\text{O}_4$, Y is the defect vacancy) has been prepared and the capacity retention rate after 500 cycles at a current density of 500 mA/g is 94% [68]. The formation of Mn ion vacancies reduces the electrostatic repulsion of Zn^{2+} , leading to a rapid kinetic process. More importantly, various methods have shown that the electrochemical behavior of ZMO is caused by Zn^{2+} intercalation rather than H^+ intercalation (Reaction 2.11).



A study in recent years has shown that $\beta\text{-MnO}_2$ nanorods can be transformed into spinel ZnMn_2O_4 after several cycles, and this spinel phase can be cycled more than 200 times [69]. The conversion of $\beta\text{-MnO}_2$ to other crystalline phases has also been reported [70].

Another spinel-type Mn oxide, Mn_3O_4 (MnMn_2O_4), has been used in aZIBs [71, 72]. There is a two-step reaction mechanism for ZIBs using Mn_3O_4 cathodes. The first discharge potential plateau likely involves intercalation of Zn^{2+} and possibly H^+ , followed by a conversion reaction forming ZHS during the second discharge potential plateau. The reverse occurs on charge.

According to the literature, Zn^{2+} can also be inserted into $\alpha\text{-Mn}_2\text{O}_3$ [73, 74, 75, 76, 77, 78]. Detailed discussion of this material will be done in Sections 2.3 and 5.2.

In summary, there are many Mn-based oxide materials used in aZIBs, which exhibit unique charging and discharging processes. However, the reaction mechanism(s) are far from being understood. In addition to Mn-based materials, vanadium-based materials and Prussian blue analog cathode materials are also widely used in aZIBs. These materials are not discussed in this review, since the focus of the thesis is Mn oxide.

2.2.2 Anode Materials for aZIBs

Currently, metallic Zn is the most common anode material, such as in various primary alkaline batteries, Zn-air batteries, Zn-Ni batteries, and Zn-Ag secondary batteries. Compared with lithium, sodium, and potassium, Zn's main advantage is that it is relatively stable and reversible in aqueous media [80,81]. Therefore, it can be directly used as an anode material for aqueous batteries [82]. Its theoretical specific capacity is 820 mAh/g [83-55], which is a much larger capacity than any other ion battery negative material (intercalation/extraction or organic electrode). On the other hand, because of its high overpotential for hydrogen evolution, metallic Zn has a lower oxidation-reduction potential (-0.76V vs. SHE) in aqueous electrolytes [86]. Metallic Zn combines the advantages of high capacity, low reduction-oxidation potential, abundant reserves, and non-toxicity and is considered to be the most promising anode material in large-scale energy storage systems. It can be applied to aZIBs and plays important roles in hybrid aqueous systems. These systems usually consist of Zn anodes and various cathode materials, which can store most metal ions, and use Zn and other metal ion salts in the aqueous electrolyte [83,87]. The reactions of the Zn anode can be written as Reactions 2.12 and 2.13.

Discharge process:



Charge process:



Metal Zn anodes, however, are limited in terms of commercial use in secondary batteries because they are hindered by the generation of Zn dendrites and that have a low plating/stripping efficiency [83-85,88]. The growth of Zn dendrites is particularly serious in alkaline Zn-Mn, Zn-

Ni, and Zn-air secondary batteries. Generally, Zn dendrites are easily produced at the anode and the mechanism has been extensively studied [88,89]. Fig. 2.4 summarizes the common problems encountered in alkaline (Fig. 2.4a) and mild-pH media (Fig. 2.4b) [90]. Some typical problems, such as shape change and ZnO passivation, encountered in alkaline electrolytes are not serious in mildly acidic electrolytes because of the different Zn electrode reaction mechanisms. The most common problems, such as dendrite growth and H₂ evolution, are the main reasons for the occurrence of irreversible reactions in ZIBs, which reduces the Coulombic efficiency of Zn electrodes and deteriorates their performance.

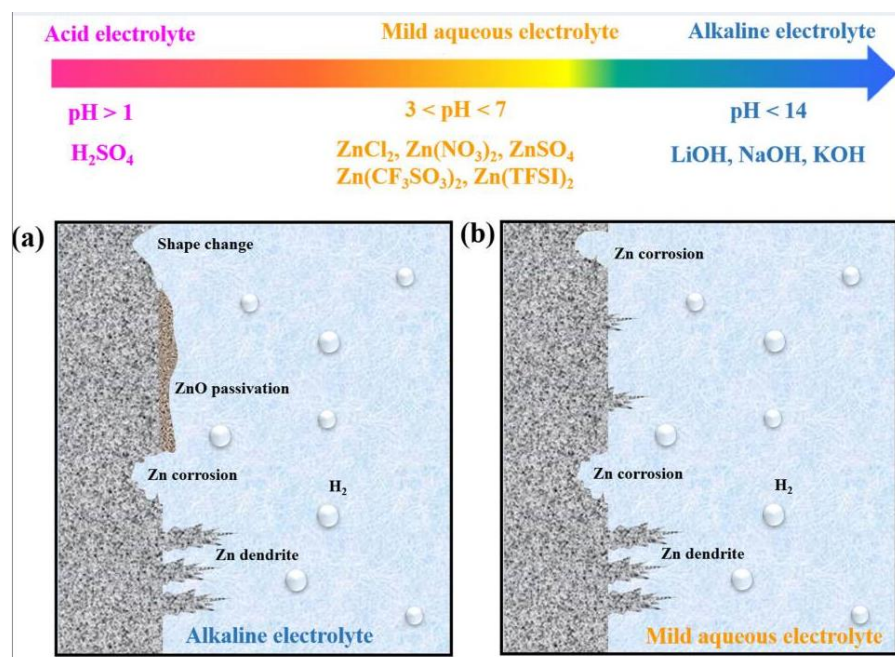


Figure 2.4 Schematic illustration of the phenomena observed on Zn electrodes in (a) alkaline and (b) mild aqueous electrolytes. [90].

In recent years, composite anode materials for aZIBs have also been reported. Kang et al [91] proposed a new composite anode material for aZIBs, which is made by mixing metallic Zn particles with activated carbon (AC), prepared by a simple pre-carbonization and chemical activation process of the pitch mesophase. The anode product induced by activated carbon is pre-deposited on the activated carbon pores instead of on the surface of Zn particles, which greatly

improves the electrochemical reaction kinetics and reversibility of the Zn anode. Constant current charge and discharge results show that, after 80 cycles, the material capacity retention rate of a Zn anode with 12% activated carbon added is 85.6%, which is higher than that of a pure Zn anode (56.7%). Mantia et al [92] created a Zn-Al layered double hydroxide as a substrate base to electrodeposit Zn to improve the electroplating/stripping efficiency of the Zn anode in a neutral electrolyte. The Zn-Al layered double hydroxide electrode's Coulombic efficiency was as high as 98%, which is much higher than that of metallic Zn (about 85%). Chen et al [93] used an optimized neutral electrolyte (0.6 mol/L ZnSO₄ + 0.1 M (NH₄)₂SO₄) as a bath to electroplate the Zn electrode. There was less hydrogen evolution and dendrite formation on the Zn surface. Its advantages can be attributed to the special crystalline morphology and surface texture of electro-galvanized materials [87].

2.2.3 Electrolytes for aZIBs

Since aqueous electrolytes are safer, cheaper, and easier to assemble than nonaqueous electrolytes, ZIBs based on them have received a lot of attention. Furthermore, aqueous electrolytes provide better ionic conductivity in general, which favors high-rate performance. As a result of these characteristics, the aZIB is a promising solution for stationary fast-response balancing systems where weight is less critical than safety, cost, and response time. As previously stated, Zn dendrite and ZnO development are caused by alkaline aqueous electrolytes, resulting in severe capacity fading and low Coulombic efficiency. Strongly acidic electrolytes, on the other hand, will cause corrosion of the Zn anode and current collectors, leading to poor long-term dependability. As a result, neutral or mildly acidic electrolytes appear to be better for use in ZIBs. Different Zn salts including Zn(CF₃SO₃)₂, ZnSO₄, Zn(NO₃)₂, Zn(CH₃COO)₂, ZnF₂, Zn(ClO₄)₂, and ZnCl₂ have been studied by far [43, 44, 45, 46, 47].

Because of its low cost and stability, ZnSO₄ is the most frequent and commonly electrolyte material utilized in ZIBs, and good results have been produced. Lee et al.'s work proposed that the pH fluctuations during discharge/charge prompted a reversible precipitation/dissolution mechanism of ZHS. [40] The initial discharge reaction was shown to be accompanied by an

electrolyte pH rise due to Mn oxide dissolution (Reaction 2.7). ZHS formation began (Reaction 2.8) when the pH reached 5.47.

$\text{Zn}(\text{CF}_3\text{SO}_3)_2$ has a large electrochemical window, similar to ZnSO_4 , and effectively suppresses H_2 evolution in the battery [54]. However, $\text{Zn}(\text{CF}_3\text{SO}_3)_2$ is not extensively used because it is much more expensive than ZnSO_4 . Raising the electrolyte concentration, for both ZnSO_4 and $\text{Zn}(\text{CF}_3\text{SO}_3)_2$, can increase the Coulombic efficiency due to lower water activity, water side reactions, and changed cation/anion solvation and transport, [19, 20]. Several alternative aqueous electrolytes, including ZnCl_2 , $\text{Zn}(\text{ClO}_4)_2$, and $\text{Zn}(\text{NO}_3)_2$, have been utilized for ZIBs, but have their own issues, including electrode deterioration [52, 94, 95].

2.3 Thesis research topic

2.3.1 Mn_2O_3 as the cathode material for aZIBs

Mn (III) oxide is an oxide of Mn with a Mn^{3+} valence state. It usually is black and is an amphoteric oxide. There are two crystal types, i.e., α - Mn_2O_3 and γ - Mn_2O_3 . α - Mn_2O_3 (Fig. 2.5) is more common structure and the most stable form. γ - Mn_2O_3 cannot exist stably for a long time at room temperature and gradually transforms to α - Mn_2O_3 . α - Mn_2O_3 has a bixbyite structure and its basic structural unit is the same as that of MnO_2 , Mn oxide octahedra $[\text{MnO}_6]$ as the key component [96]. Interestingly, unlike MnO_2 or other cathode materials, the bixbyite structure of Mn_2O_3 does not have obvious tunnels, layered structures, or 3D-channels to host the intercalation of Zn^{2+} . The energy storage mechanism α - Mn_2O_3 as the cathode material of aZIB is still under discussion.

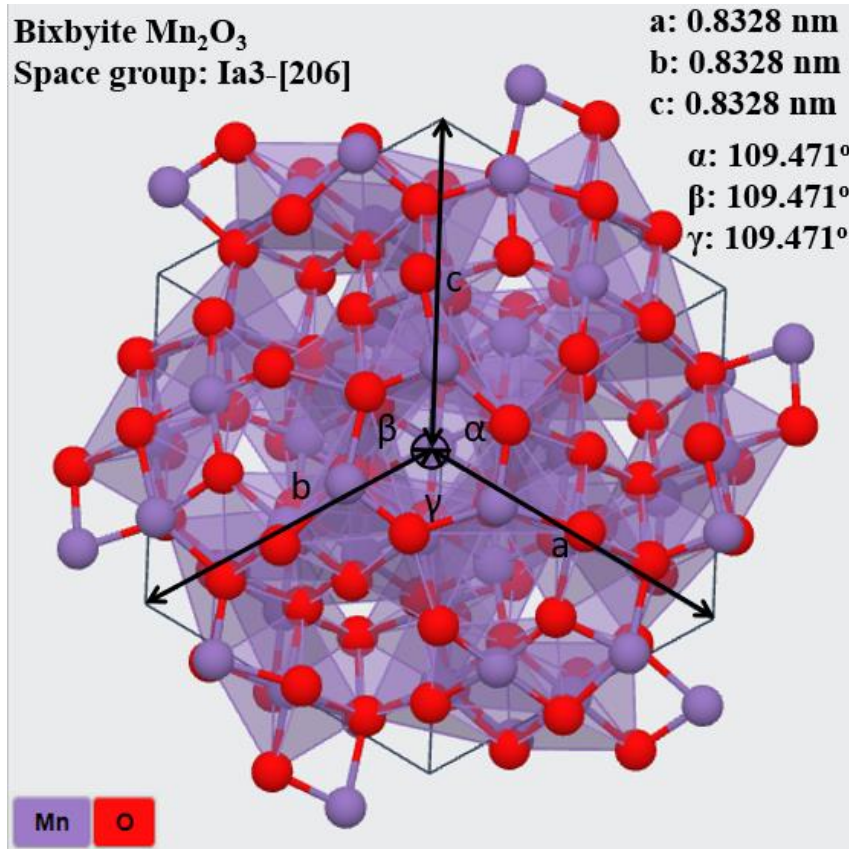


Figure 2.5 Crystal structure of alpha- Mn_2O_3 [97].

Mn_2O_3 was reported for the first time as a cathode material for aZIBs in 2017 by Jiang et al [73]. There are also several more recent studies that have examined the use of Mn_2O_3 as the cathode for ZIBs [74-78]. The electrochemical performance and energy storage mechanisms proposed in these studies are summarized in Tables 2.2 and 2.3. The various researchers all report good electrochemical performance, with specific capacities in excess of 100 mAh/g at current densities less than 200 mA/g (Table 2.2). There is no consensus regarding the charge storage mechanisms for Mn_2O_3 in aZIBs; the proposed mechanisms are briefly summarized in Table 2.3. All researchers report that the discharge process involves some type of intercalation of Zn^{2+} and/or H^+ . Other processes are proposed, including the formation of phases incorporating Zn; e.g., layered-type Zn-birnessite, MnO_2 birnessite, and ZHS. The charge storage mechanism(s) is a major component of this thesis and will be compared and discussed in detail in Section 4.2 and compared with the results from the current study.

Table 2.2. Electrochemical performance comparison of previous studies of bixbyite Mn₂O₃ as the cathode for ZIBs

Specific Capacity (mAh/g)	Current Density (mA/g)													Potential Window & Electrolyte
	50-60	100	150	200	300	500	600	900	1000	1500	1800	2000	3000	
Authors														
Jiang et al [73]		137		100	86	74			57			38		1 V-1.9 V 2 M ZnSO ₄
Mao et al [74]	225	200		175	160	145			120			100	70	0.9 V-1.9 V 2 M ZnSO ₄ + 0.2 M MnSO ₄
Feng et al [75]	292		258		228		206			179			162	1 V-1.8 V 2 M ZnSO ₄ + 0.2 M MnSO ₄
Shen et al [76]		190			150			130			100		85	1 V-1.9 V 2 M ZnSO ₄ + 0.1 M MnSO ₄
Ma et al [77]		228		217					148			131	105	1 V-1.9 V 2 M ZnSO ₄ + 0.1 M MnSO ₄
Yang et al [78]		152		123	105 at 400 mA/g		82 at 800 mA/g			65 at 1600 mA/g		39 at 3200 mA/g		0.8 V-1.9 V 1 M ZnSO ₄
Values are determined from data presented in the specific reference.														

Table 2.3. Charge storage mechanism comparison of previous studies of bixbyite Mn₂O₃ as the cathode for ZIBs

Author Name	Cathode	Anode	Potential Window	Electrolyte	Charge Storage Mechanisms
Jiang et al [73]	Mn ₂ O ₃ (cubic)	Zn Metal	1 V-1.9 V	2 M ZnSO ₄	<ul style="list-style-type: none"> Mn₂O₃ transformed to layered-type Zn-birnessite Zn²⁺ intercalation/extraction
Mao et al [74]	Mn ₂ O ₃ (cubic)	Zn Metal	0.9 V-1.9 V	2 M ZnSO ₄ + 0.2 M MnSO ₄	<ul style="list-style-type: none"> Mn₂O₃ transformed to layered-type Zn-birnessite Zn²⁺ and H⁺ intercalation/extraction
Feng et al [75]	Mn ₂ O ₃ (ortho)	Zn Metal	1 V-1.8 V	2 M ZnSO ₄ + 0.2 M MnSO ₄	<ul style="list-style-type: none"> MnO formed during H⁺ intercalation ZHS formation Zn²⁺ and H⁺ intercalation/extraction
Shen et al [76]	Mn ₂ O ₃ (cubic)	Zn Metal	1 V-1.9 V	2 M ZnSO ₄ + 0.1 M MnSO ₄	<ul style="list-style-type: none"> Zn²⁺ and H⁺ intercalation/extraction
Ma et al [77]	Mn ₂ O ₃ (cubic)	Zn Metal	0.8 V-1.9 V	3 M ZnSO ₄ + 0.2 M MnSO ₄	<ul style="list-style-type: none"> Birnessite MnO₂ formed during cycling and acted as a host for Zn²⁺ and H⁺ intercalation/extraction ZHS formation
Yang et al [78]	Mn ₂ O ₃ (cubic)/ ZnMn ₂ O ₄ (#23-1113)	Zn Metal	0.8 V-1.9 V	1 M ZnSO ₄	<ul style="list-style-type: none"> Mn₂O₃ transformed to layered-type Zn-birnessite ZnMn₂O₄ listed as energy storage cathode

2.3.2 Thesis objectives

The first objective of this work is to synthesize the Mn oxides (Mn₂O₃ and Mn₃O₄) for use as the cathode in aZIBs. The synthesis method is based on the technique used to synthesize the

cathode material for LIBs and sodium-ion batteries (SIBs) established by the author's previous study [98]. From the initial tests, the synthesized Mn oxides exhibited good electrochemical performance as the cathode material for aZIBs, making them promising cathode material candidates for aZIBs.

The second objective is to further study the synthesized Mn_2O_3 as the cathode material for aZIBs and to investigate the electrochemical performance and the discharge/charge mechanism(s) associated with the material. As mentioned in the previous section, various discharge/charge mechanisms have been proposed in the literature, but there is considerable disagreement and no consensus. A new mechanism is proposed in this work and is discussed in relation to the previous work done on Mn_2O_3 .

Chapter 3: Characterization Methods

3.1. Galvanostatic charge and discharge (GCD)

Galvanostatic charge and discharge testing is used to control the electrode material to charge and discharge at a fixed current density within a given voltage interval, record the electrical data changes throughout the electrode potential window, and evaluate the electrochemical performance of the electrode material. The data is plotted with the x-axis representing specific capacity (C, mAh/g) and the y-axis representing voltage (V). Eq. (3.1) [99] is used to estimate the battery's specific capacity:

$$C = I(\text{constant here}) * t/m \quad [3.1]$$

where C is the specific capacity (mAh/g), I is the applied current (mA), which is constant in a CV test, t is the charge and discharge period (h), and m is the active mass of the cathode material (g). GCD testing may reveal the battery's capacity at various applied currents, as well as insight into the redox processes taking place, Coulombic efficiency, cycle performance, and rate capabilities. An example of GCD curves is shown in

3.2 Cyclic Voltammetry (CV)

Cyclic voltammetry (CV) is a common electrochemical characterization technique that can provide quantitative and qualitative information regarding electrode processes. CV involves the application of a linearly sweeping voltage over time between a lower and upper potential limit of interest. The collected data are presented as a graph called a voltammogram, where the x-axis is the potential and the y-axis is current, specific current, or current density. The size and shape of a voltammogram gives information on redox reactions that occur at the electrode. The positive current portion represents an oxidation reaction (charge) and the negative current portion represents a reduction reaction (discharge).

3.3 X-ray Diffraction (XRD)

X-ray diffraction is one of the essential means to analyze the crystal structure of materials. XRD can be divided into single-crystal diffraction analysis and polycrystalline diffraction analysis. Single crystal diffraction analysis is mainly used to analyze the structure, phase, crystal orientation, and integrity of single crystals. Polycrystalline diffraction analysis mainly analyzes the phase, internal stress, and texture of polycrystalline materials. Different materials have specific crystal structures with unique diffraction patterns. The difference between the number, position, and intensity of the diffraction lines on the diffraction spectrum can be used to analyze the structure according to the Bragg equation (Eq. 3.2):

$$2d\sin\theta = n\lambda \quad [3.2]$$

where d represents the distance between the crystal planes of the material, θ is the Bragg angle and represents the angle between the incident X-ray and the diffracted crystal plane, λ is the wavelength of the incident X-rays, and n represents the diffraction order. If the wavelength λ of the incident X-rays is known, the peak position and intensity of the diffraction line can be determined and then compared with appropriate structures in a diffraction database.

3.4 X-ray photoelectron spectroscopy (XPS)

X-ray photoelectron spectroscopy (XPS) is a potent method for determining the chemical state and composition of surfaces. The sample is bombarded with a beam of x-rays of fixed wavelength. The electrons associated with the atoms in the sample absorb the x-rays, and some of the electrons are released from the sample surface; these electrons are known as photoelectrons. The energy of the expelled electrons is measured, providing information on the atomic species and kinds of bonds present in the sample. Photoelectrons have a low energy and can only escape from the near surface region of the sample. As a result, XPS is a surface method, with data obtained only from the sample's top few nanometers.

3.5 Scanning electron microscopy (SEM) and energy dispersive x-ray spectroscopy (EDS)

In materials science, scanning electron microscopy (SEM) is a flexible technique. Because SEM includes the movement and detection of electrons, it must be carried out in a vacuum because air particles obstruct electron transport. A sample must be conductive in order to be imaged in the SEM. To enable imaging of non-conducting samples, the sample can be coated with a conductive substance such as C or Au. SEM works by concentrating electrons into a narrow beam, with energies typically ≤ 20 keV, and scanning it across a surface. When an electron beam collides with a sample, a series of interactions occur, causing electrons and photons to be ejected. Ejected electrons are gathered for each individual point on the sample surface as the beam is scanned across it. The brightness of each point is proportional to the quantity of detected electrons. Locations emitting a large number of electrons appear brighter than those emitting only a few electrons. When an electron beam interacts with a material, several different types of electrons are emitted. Different contrast effects occur depending on the type of electron detected. When an electron beam interacts with the electron shell of an atom, secondary electrons (SE) are released. SEs have a low energy (2-5 eV) and provide information about a sample's topography. When the incoming beam interacts with the nucleus of a sample atom, backscattered electrons (BSE) are released. BSEs have a high energy (1-20 keV) and produce atomic number contrast. Atoms with higher atomic numbers backscatter electrons more effectively than atoms with lower atomic numbers. Photons can be released in the form of characteristic x-rays, which are due to inner shell ionizations followed by electron transitions from higher energy states to lower energy states. These x-rays have characteristic energies related to the elements that produce and can be used to determine the composition of a sample; this approach is known as energy dispersive x-ray spectroscopy (EDS). SEM images typically have a resolution of 1-50 nm, while certain specialist instruments may attain resolutions on the order of angstroms. The kind of signal detected, the spot size, the accelerating voltage, the beam current, and the sample material all influence the resolution. A field emission electron source coupled with an in-lens detector can provide high resolution images of a variety of materials [99].

3.6 Transmission electron microscopy (TEM)

Another useful tool in materials research is transmission electron microscopy (TEM). As with SEM, a high energy electron beam is used for imaging although the beam energy is higher; i.e., 100 – 200 keV. Unlike SEM, the beam is not scanned over the sample surface but is stationary and is allowed to pass through a thin specimen. High resolution imaging is possible with TEM analysis; some instruments can achieve image resolutions of 50 pm. There are several imaging modes. Bright field imaging uses the portion of the electron that passes through the specimen without being scattered to form the image. Dark field imaging uses one of the scattered/diffracted beams from a crystalline sample to form the image. Bright field and dark field images are somewhat complimentary and are effective for imaging defects, such as grain/phase boundaries, second phases, and dislocations. Electron diffraction patterns are also generated as the electron beam passes through the sample, allowing for crystallographic investigation of nanoscale features. The principles of diffraction are similar to those for x-ray diffraction, although the Bragg angles are considerably smaller. As with SEM, characteristic x-rays are generated through electron beam specimen interactions and these can be utilized for composition analysis, with much better spatial resolution than EDS analysis in the SEM. [100] TEM, like SEM, must be carried out in a vacuum. The major limitation of TEM is that the samples must be electron transparent. This means that samples should be no more than 200 nm thick; for high resolution TEM even thinner samples are necessary.

Scanning transmission electron microscopy (STEM) is essentially a cross between SEM and TEM. STEM works by scanning a focused electron beam over an electron transparent sample's surface. The electrons that pass through the sample are collected serially and images are generated in a manner similar to an SEM. The main detectors are a bright field (BF) detector which collects electrons that are not scattered or are scattered at very low angles, and annular dark field detectors (ADF) that collect all the scattered electrons. BF and ADF images are complimentary. There are two types of ADFs; i.e., conventional ADF detectors and high angle ADF (HAADF) detectors. HAADF detectors collect electrons scattered at larger angles, i.e., greater than 50 mrad. The detectors provide mass-thickness contrast and under the appropriate conditions atomic resolution is possible. EDS analysis can also be done in STEM mode. Line scans and composition maps can

be generated, as well as point analysis [100]. EDS analysis in TEM mode only provides analysis of individual points of samples.

3.7 Rotating disk electrode (RDE) and Rotating ring-disk electrode (RRDE)

A rotating disc electrode (RDE) is a working electrode for hydrodynamic voltammetry that is utilized in three electrode systems. [101, 102] During testing, the electrode rotates, causing the analyte to flow to the electrode. Electrochemical investigations of the reaction mechanisms related to redox chemistry, among other chemical phenomena, employ these working electrodes. A conductive disc contained in an inert non-conductive polymer or resin can be coupled to an electric motor that can precisely regulate the electrode's rotation rate. The disc, like any other working electrode, is usually formed from a noble metal or glassy carbon, but any conductive material can be employed depending on the application. The rotation of the disc is commonly expressed in terms of angular velocity. As the disc spins, a portion of the solution known as the hydrodynamic boundary layer is dragged by it, and the ensuing centrifugal force flings the solution away from the electrode's center. The bulk solution flows up perpendicular to the electrode, replacing the boundary layer. A laminar flow of solution towards and over the electrode is the end outcome. The angular velocity of the electrode may be used to alter the rate of solution flow, which can then be mathematically predicted. This flow can quickly establish circumstances where the solution flow, rather than diffusion, controls the steady-state current. In contrast, in experiments like cyclic voltammetry, the steady-state current is constrained by the diffusion of species in the solution. Different electrochemical phenomena, such as multi-electron transfer, the kinetics of sluggish electron transfer, adsorption/desorption phases, and electrochemical reaction processes, can be examined by performing linear sweep voltammetry and other experiments at varied rotation rates.

A rotating ring-disk electrode (RRDE) [102, 103] is a double working electrode used in hydrodynamic voltammetry and is very similar to a rotating disk electrode (RDE). In an RRDE test, one electrode is the disk electrode located in center, and the other electrode is the ring electrode surrounding the disk electrode. During testing, both the ring and disk electrodes rotate at the same rate. The inner electrode is rotated during the experiment, inducing a flux of analyte to the outer ring electrode. This system is used in electrochemical studies for investigating reaction

mechanisms related to redox chemistry and other chemical phenomena. The RRDE setup allows for many additional experiments well beyond the capacity of an RDE setup. For example, if one electrode is subjected to linear sweep voltammetry the other electrode can be kept at a constant potential or also swept in a controlled manner. Step experiments with each electrode acting independently can also be conducted. These, as well as many other extremely elegant experiments, are possible, including those tailored to the needs of a given system. Such experiments are useful in studying multi-electron processes, the kinetics of slow electron transfer, adsorption/desorption steps, and electrochemical reaction mechanisms.

3.8 Atomic absorption spectroscopy (AAS)

Atomic absorption spectroscopy (AAS) is a spectroanalytical procedure for the quantitative determination of chemical elements [104]. AAS is based on the absorption of light by free metallic atoms. AAS detects elements in either liquid or solid samples through the application of characteristic wavelengths of electromagnetic radiation from a light source. Individual elements will absorb wavelengths differently, and the absorbance is measured against standards. In effect, AAS takes advantage of the different radiation wavelengths that are absorbed by different atoms. For liquid samples, analyte ions are first atomized to free atoms, typically by a flame or plasma, so that characteristic wavelengths of the free atoms can be emitted, recorded and defined. During excitation, electrons move up one energy level in their respective atoms when those atoms absorb a specific energy. This energy corresponds to a specific wavelength that is characteristic of the element. Depending on the light wavelength and its intensity, specific elements can be detected and their concentrations measured. AAS has high sensitivity, but does not permit multicomponent analysis. Only one absorbance concentration can be tested during a single trial. AAS detection limits are usually specified by element types and instruments as a range of atom concentration. For the instrument used in this work (Thermo Scientific ICE-3500), the detection limit for Cu is 0.008 $\mu\text{g/mL}$ and the sensitivity is 5 ppm. AAS has many uses in different areas of chemistry, such as clinical analysis of metals in biological fluids and tissues such as whole blood, plasma, urine, saliva, brain tissue, liver, hair, and muscle tissue.

Chapter 4: Mn oxide synthesis

4.1 Synthesis method

The method of synthesizing the desired Mn oxide cathode material is based on the author's previous study involving the cathode material for SIBs [98]. The method has been modified where appropriate.

An acidic metal sulfate solution was prepared, consisting of 0.1 M Mn sulfate monohydrate ($\text{MnSO}_4 \cdot \text{H}_2\text{O}$, $\geq 99\%$) dissolved in water (100 mL). The base, aqueous solution consisted of 100 mL sodium hydroxide (NaOH , $\geq 99\%$) and ammonia ($\text{NH}_3 \cdot \text{H}_2\text{O}$, 28-30%) with a molar ratio of $\text{NaOH}:\text{NH}_3 \cdot \text{H}_2\text{O} = 2.4$ (0.2 M NaOH). The starting solution was obtained by dissolving NaOH and $\text{NH}_3 \cdot \text{H}_2\text{O}$ ($\text{NaOH}:\text{NH}_3 \cdot \text{H}_2\text{O} = 2.4$, 1 M NaOH) in water (40 mL) with the pH carefully adjusted to 10.5 using sulfuric acid (2 M H_2SO_4). The acidic MnSO_4 solution and the base solution were slowly added to the starting solution at a rate of $\approx 2 \text{ mL min}^{-1}$. The pH, (10.5 ± 0.3) was maintained until the reaction was complete. The brown precipitates were then collected by filtration and dried overnight in a vacuum oven at 70°C . The resulting precursor powder was transferred to a box furnace and calcined in air at $400 - 1000^\circ\text{C}$ for 10 h. The whole process is shown in Fig. 4.1.

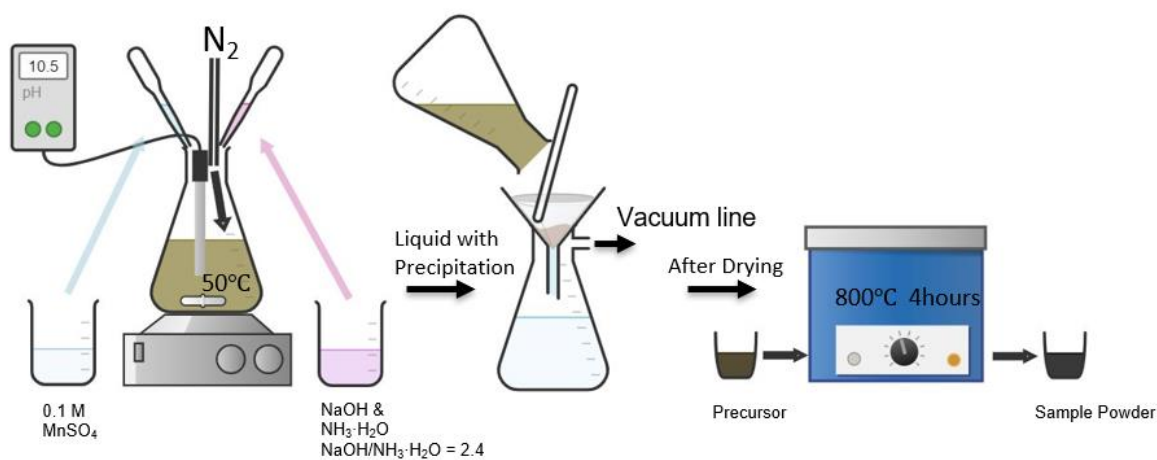


Figure 4.1 Illustration of material synthesise method.

Depending on the calcination temperature, the final product powders were characterized by XRD to be hausmannite Mn_3O_4 (JCPDS 89-4837, 0 to 600°C), bixbyite Mn_2O_3 (JCPDS 41-

1442, 800 to 900 °C), or a mixture of hausmannite Mn_3O_4 and bixbyite Mn_2O_3 (700, 900 and 1000 °C). XRD patterns for the different calcination treatments are shown in Fig. 4.2. Note that both the Mn_3O_4 and Mn_2O_3 powder are highly crystalline. An SEM image and EDS spectrum of the Mn_3O_4 powder after calcination at 400 °C are shown in Fig. 4.3 and an SEM image and EDS spectrum of the Mn_2O_3 powder after 800 °C calcination are shown in Fig. 4.4. The synthesized powders are nanosized with Mn_3O_4 particles having a much smaller size than Mn_2O_3 particles. samples are in round morphology and contain mostly Mn and O. The Mn_3O_4 sample has a Mn:O atomic ratio of ~ 0.89 which is relatively close to the ideal ratio (0.75). The Mn_2O_3 sample has a Mn:O atomic ratio of ~ 0.65 which is close to the ideal ratio (0.67). For both EDS spectra, there are small peaks from C, Na, and S. The C peak is from the carbon tape used to attach the powders to the SEM stub and Na and S are residuals from the chemicals ($MnSO_4$ and $NaOH$) utilized in the synthesis process.

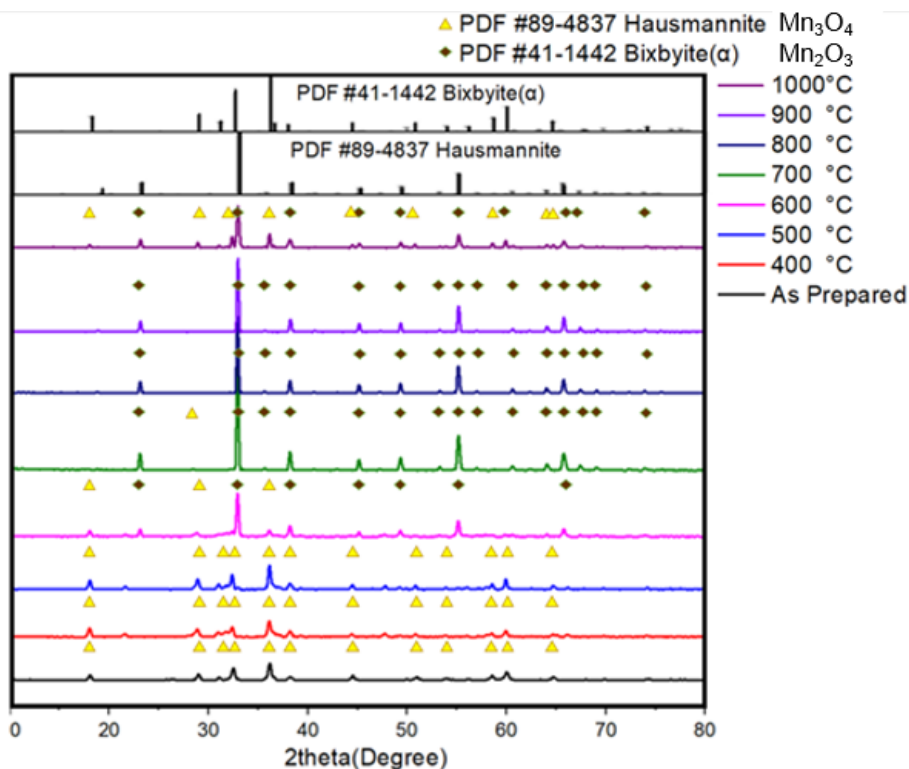


Figure 4.2 XRD patterns for different calcination temperatures.

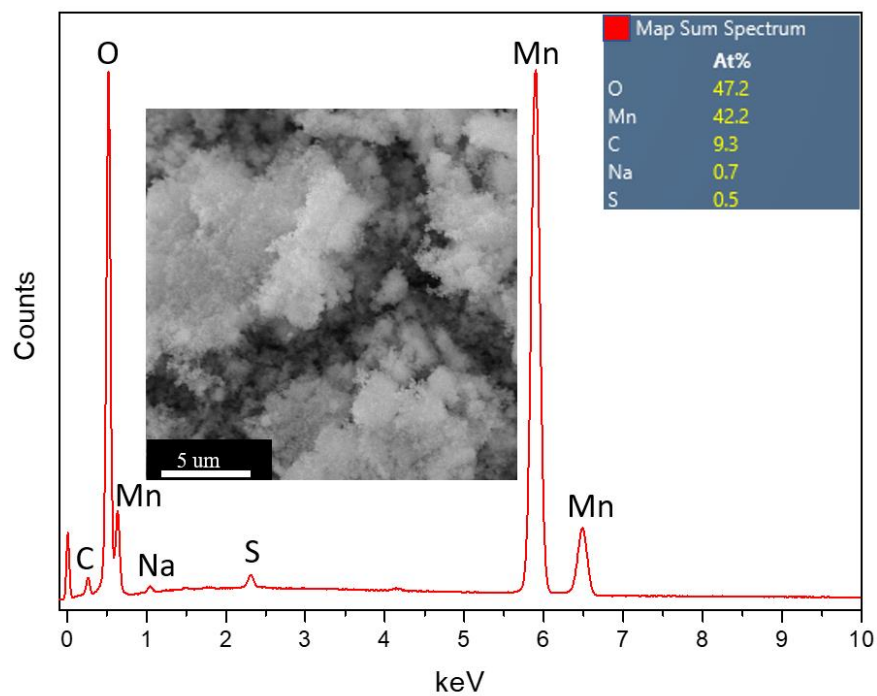


Figure 4.3 SEM image and EDS spectrum of Mn_3O_4 powder after calcination at 400 °C.

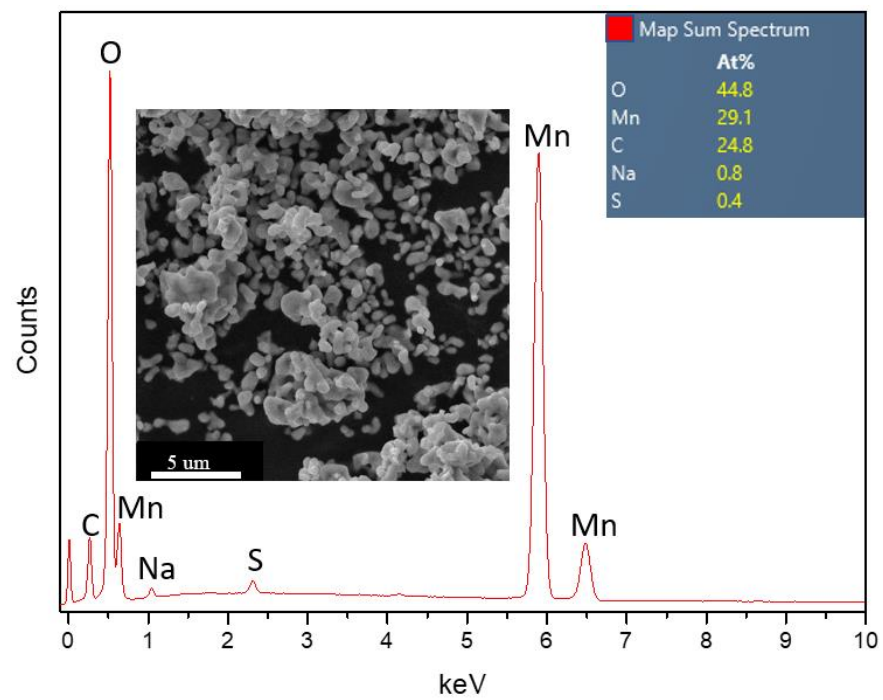


Figure 4.4 SEM image and EDS spectrum of Mn_2O_3 powder after calcination at 800 °C.

4.2 Electrochemical performance of Mn₃O₄ as the cathode material for aZIBs

Both the Mn₃O₄ and Mn₂O₃ powders, calcined at 400 and 800 °C, respectively, were tested as cathode materials for aZIBs. Mn₃O₄ and Mn₂O₃ electrodes were prepared in the same manner by uniformly spreading a slurry (N-methyl-2-pyrrolidone as the solvent), containing the active material (70 wt%), acetylene carbon (20 wt%), and polyvinylidene fluoride (pVdF, 10 wt%) as the binder, on carbon paper (graphite carbon current collector). The electrodes were then dried overnight at 120°C in a vacuum oven. CR2032 coin cells were assembled in air using composite cathode, Zn foil as the anode, Whatman glass fiber paper (GF/D) as the separator, and 2 M ZnSO₄ with 0.2 M MnSO₄ aqueous solution as the electrolyte.

Electrochemical performance results utilizing Mn₃O₄ are shown in Fig. 4.3. Cyclic voltammetry (CV) measurements were carried out by using the as-prepared Zn/Mn₃O₄ cell, with a potential window from 1.0 to 1.8 V a scan rate of 0.5 mV/s. The CV curves are shown in Fig. 4.5a-c. The initial cycle reveals one oxidation peak at 1.58 V and two reduction peaks at 1.39 and 1.23 V, which corresponds to results reported in [72].

The open-circuit voltage of the as-assembled Zn/Mn₃O₄ battery is approximately 1.34 V. Galvanostatic charge-discharge (GCD) curves for the initial eight cycles under an applied 30mA/g current density are shown in Fig. 4.5d. Both the charge and discharge curves clearly exhibit two plateaus which correspond to the peaks in CV plots. The cathode reached a specific capacity of 225mAh/g after 8 cycles. Short-term cycling performance at 200 mA/g is presented in 4.5e. The initial discharge capacity is 100 mAh/g and then it gradually increases to 130 mAh/g at the 18th cycle. The Coulombic efficiency remains at ~99% at 18th cycle. The rate performance of the Zn/Mn₃O₄ cell was also tested and is shown in Fig. 4.5f. The Zn/Mn₃O₄ cell delivers discharge capacities of 211, 155, 131, and 99 mAh/g, respectively, at current densities of 30, 100, 200, and 300 mA/g. The electrochemical performance of the Mn₃O₄ cells is reasonable compared with the current Mn₃O₄ electrode literature [105, 106, 107].

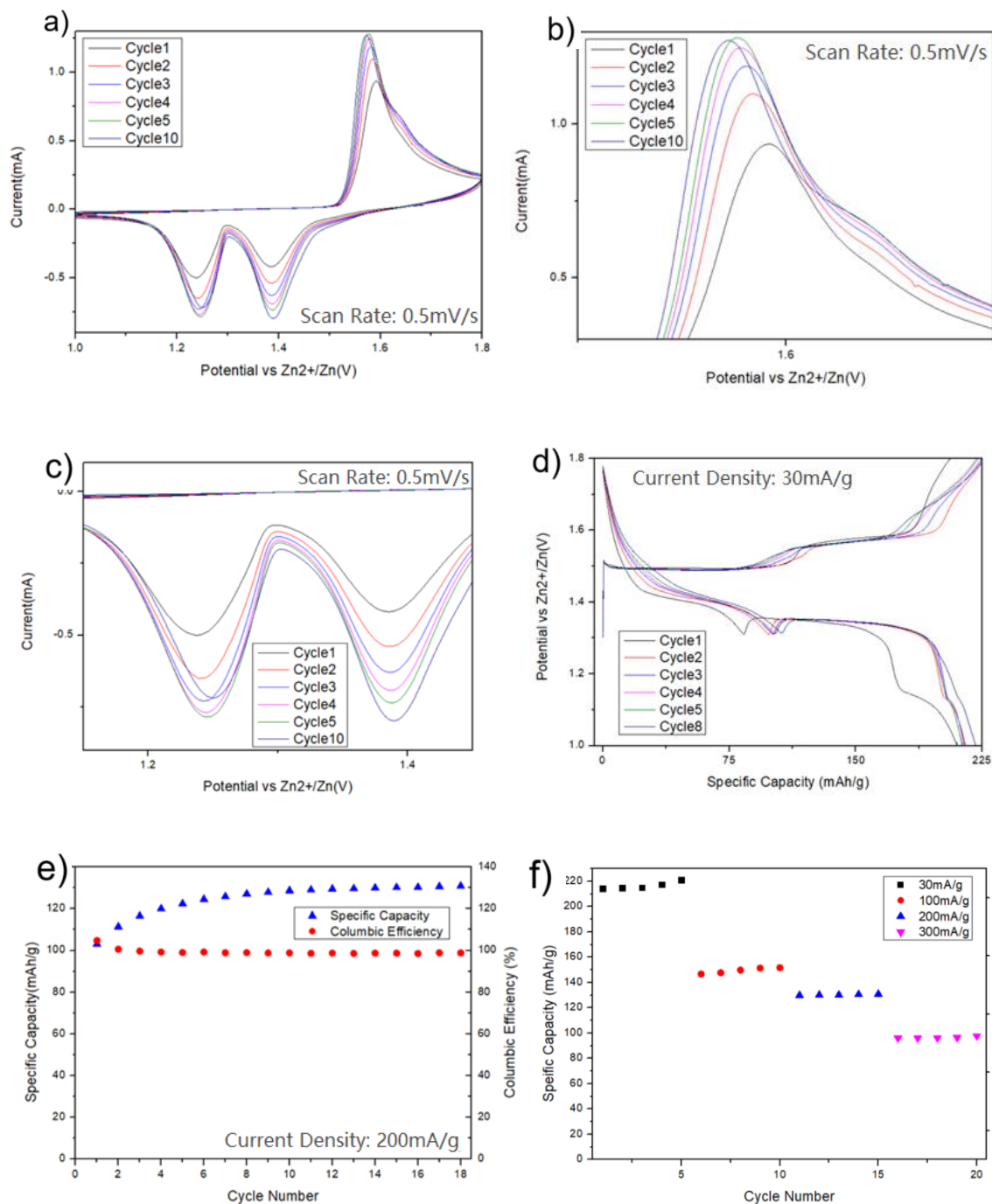


Figure 4.5. a) CV plots at 0.5 mV/s scan rate for Mn₃O₄ as the cathode material. b) Enlarged CV oxidation peaks for a potential window of 1.5-1.7 V. c) Enlarged CV reduction peaks for a potential window of 1.1-1.5 V. d) GCD cycling test under an applied 30 mA/g specific current density. e) Cell cyclability results at an applied specific current of 200 mA/g. f) Rate capability test results at various applied current densities.

After preliminary analysis of Mn_3O_4 and Mn_2O_3 , it was decided to cease work on Mn_3O_4 and to focus efforts on the utilization of synthesized Mn_2O_3 powder as the cathode material for aZIBs. Previous work in Ivey's Group using the Mn_3O_4 cathode exhibited good rate capability [72]. At 300, 600, 1200, 2400, and then again at 300 mA/g current densities, the battery was able to deliver capacities of 201, 180, 164, 143, and 217 mAh/g, respectively. Dhiman et al.'s work utilized a different material synthesis method; i.e., direct electrodeposition onto carbon paper (CP). Compared with the slurry casting method employed here, electrodeposition can be more efficient in covering the CP and create a larger cathode surface area contacting the electrolyte. The specific capacity of the synthesized Mn_3O_4 cathode via the precipitation, calcination, and casting method at 300 mA/g current density is only 99 mAh/g, which is half the capacity reported in Dhiman et al.'s work achieved. There are several ways to improve the electrochemical performance of the Mn_3O_4 cathode synthesized via the method employed in this thesis, such as controlling the mass loading, adjusting the active material to carbon ratio, and synthesizing smaller particles. However, due in part to time constraints and to our interest in exploring the discharge/charge mechanisms associated with Mn_2O_3 , the focus of this thesis is on Mn_2O_3 as a potential cathode material in aZIBs. There is considerable controversy and uncertainty regarding the mechanism(s) as already mentioned.

Chapter 5: Charge storage mechanism and cycling performance of Mn_2O_3

A version of this chapter has been submitted to *Advanced Energy Materials*:

Q. Hou, T. N. T. Tran, Z. Abedi, D. G. Ivey, An Investigation into the Charge Storage Mechanism and Cycling Performance of Mn_2O_3 as the Cathode Material for Zinc-ion Batteries, *Batteries & Supercaps*, submitted April 2022.

5.1 Introduction

Easily exploitable traditional fossil fuels are being depleted and they contribute to the decline in air quality [1]. Therefore, it is imperative to develop new, efficient, clean, and sustainable energy sources to replace traditional sources [2,3]. Batteries have been widely studied as energy devices that can convert chemical energy into electrical energy. Currently, the most widely used batteries include LIBs [4], lead-acid batteries [9], and nickel-cadmium batteries [10]. These batteries all have some shortcomings, which limit their usage. For example, LIBs have cost, safety, and environmental issues, as well as potentially limited supplies of lithium [8]. Lead-acid batteries have low specific energy density, poor cycle performance, and environmental problems [9]. Nickel-cadmium batteries exhibit a memory effect and have environmental issues [108]. As such, none of these batteries fully satisfy the requirements of a secondary battery.

Secondary aqueous ion batteries have attracted researchers' attention due to their low cost, long cycle life, and safe operation. These batteries utilize an aqueous solution as the electrolyte; the aqueous electrolyte is safe, easy to prepare, and has high ionic conductivity. Therefore, secondary aqueous ion batteries are considered as promising candidates for large-scale energy storage. In the past ten years, secondary aqueous ion batteries have received increasing attention for application in the power grid and for wearable devices and biocompatibility [12,13].

Mn oxide is widely used in various industries, for applications such as deoxidization and desulfurization, catalysis, and batteries, due to the different oxidation states (2+, 3+, and 4+) for Mn. For battery electrode materials, the diversity of Mn oxide compositions and crystal structures make it attractive [73,107]. Mn (4+) oxide (MnO_2) has been widely used as the cathode material

in aZIBs. Other oxides with different valence states, such as Mn_3O_4 (2+/3+) and Mn_2O_3 (3+), are also possible cathode candidates. Mn_2O_3 has generated interest because of its high theoretical specific capacity and energy density. Utilization of Mn_2O_3 as the cathode material in an aZIB has been reported by several research groups in recent years [66, 67, 89, 90, 91, 92]. The groups report good electrochemical performance; however, the charge storage mechanism(s) for Mn_2O_3 as the cathode material is not established as different groups have proposed different processes. Some examples include intercalation of H^+ and/or Zn^+ ions as well various chemical and electrochemical reactions.

In this study, highly crystalline bixbyite Mn_2O_3 is synthesized and utilized as the cathode material for aZIBs. In addition to reporting battery performance and cycling behavior, detailed electrochemical and microstructural characterization of Mn_2O_3 during battery discharging and charging is carried out. The analysis is then compared with the work reported in the literature, with the aim of providing further insight into the cathode processes involved during battery operation. A new mechanism, involving only chemical conversion reactions, is proposed.

5.2 Experimental Section

Material synthesis: An acidic metal sulfate solution was prepared, consisting of 0.1 M Mn sulfate monohydrate ($\text{MnSO}_4 \cdot \text{H}_2\text{O}$, $\geq 99\%$) dissolved in water (100 mL). The base, aqueous solution consisted of 100 mL sodium hydroxide (NaOH , $\geq 99\%$) and ammonia ($\text{NH}_3 \cdot \text{H}_2\text{O}$, 28-30 %) with a molar ratio of $\text{NaOH}:\text{NH}_3 \cdot \text{H}_2\text{O} = 2.4$ (0.2 M NaOH). The starting solution was obtained by dissolving NaOH and $\text{NH}_3 \cdot \text{H}_2\text{O}$ ($\text{NaOH}:\text{NH}_3 \cdot \text{H}_2\text{O} = 2.4$, 1 M NaOH) in water (40 mL) with the pH carefully adjusted to 10.5 using sulfuric acid (H_2SO_4 , 2 M). The acidic MnSO_4 solution and the base solution were slowly added to the starting solution at a rate of $\approx 2 \text{ mL min}^{-1}$. A pH, (10.5 ± 0.3), was maintained until the reaction was complete. The brown precipitates were then collected by filtration and dried overnight in a vacuum oven at 70°C . The resulting precursor powder was transferred to a box furnace and calcined in air at 800°C for 10 h.

Electrochemical measurements: Electrodes were prepared by uniformly spreading a slurry (N-methyl-2-pyrrolidone as the solvent), containing the active material (70 wt%), acetylene carbon (20 wt%), and polyvinylidene fluoride (pVdF, 10 wt%) as the binder, on carbon paper (graphite

carbon current collector). The electrodes were then dried overnight at 120°C in a vacuum oven. CR2032 coin cells were assembled in air using the Mn₂O₃ composite cathode, Zn foil as the anode, Whatman glass fiber paper (GF/D) as the separator, and 2 M ZnSO₄ with 0.2 M MnSO₄ aqueous solution as the electrolyte. The coin cells were electrochemically tested using BioLogic SP-300 and VSP-300 potentiostats. Cyclic voltammetry (CV) and galvanostatic discharge–charge (GCD) profiles were obtained from 1 V to 1.9 V vs Zn/Zn²⁺ at multiple scan rates and current densities. A rotating ring-disk electrode (RRDE) was used to investigate the reaction mechanisms during charge and discharge. A Pine Research rotator (AFMSRCE), a rotating electrode controller, and a fixed disk RRDE tip were utilized.

Materials characterization: X-ray diffraction (XRD - Rigaku Ultima IV), with a Cu K α (λ = 1.54056 Å) X-ray source, was utilized to examine the crystal structure of the samples. Oxidation states of the elements in the material were determined using X-ray photoelectron spectroscopy (XPS), via an Al-K α X-ray source with a pass energy of 20 eV (Kratos AXIS Supra XPS Instrument). The spectra were calibrated using the carbon peak at 284.8 eV. Scanning electron microscopy (Tescan Vega3 SEM, operated at 20 kV) and energy dispersive X-ray spectroscopy (EDS) were used to characterize the microstructure and composition of the fabricated samples. Transmission/scanning transmission electron microscopy (JEOL JEM-ARM 200CF TEM/STEM, operated at 200 kV) and EDS mapping were also employed to examine the microstructure and composition of samples at higher magnifications, as well as to generate additional crystal structure information. To investigate possible reactions, a rotating ring-disk electrode (RRDE) with an AFMSRCE Pine Research rotator, a rotating electrode controller, and a fixed disk RRDE tip were used. Atomic absorption spectroscopy (AAS - ThermoFisher iCE 3500) was used to determine the Mn ion concentration within the electrolyte.

5.3 Results and Discussion

5.3.1 Structure and morphology

The crystal structure of the as prepared electrode powder was determined using X-ray diffraction (XRD – Fig. 5.1). All the peaks can be indexed to the bixbyite form of Mn₂O₃ (JCPDS 41-1442, Fig. 5.11). The SEM image presented in Fig. 5.1b shows the pristine Mn₂O₃ powder

particles, which have an average size less than 2 μm . XPS analysis was also carried out to confirm the Mn oxidation state. The Mn 3s high-resolution spectrum is shown in Fig. 5.1c. The Mn valence was confirmed using the amount of Mn 3s peak splitting. The value of 5.44 eV corresponds to Mn^{3+} or Mn_2O_3 [110, 111]. A scanning transmission electron microscope (STEM) bright field (BF) image, along with corresponding energy dispersive X-ray spectroscopy (EDS) maps and a selected area electron diffraction (SAED) pattern (Fig. 5.1d), confirm the XRD and XPS results.

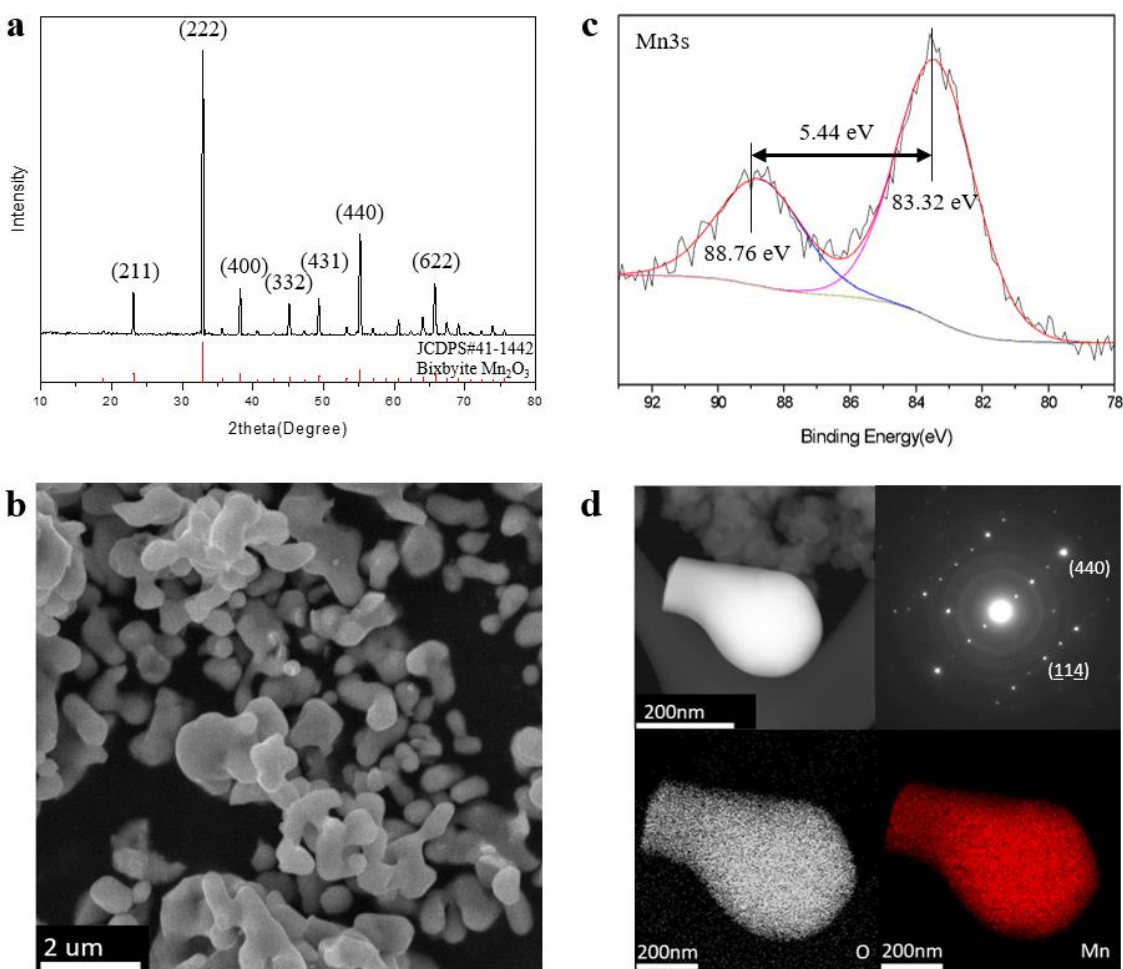


Figure 5.1. Microstructural characterization for as fabricated Mn_2O_3 . (a) XRD pattern; (b) XPS high-resolution Mn 3s spectrum; (c) SEM secondary electron (SE) image of Mn_2O_3 powder; (d) STEM annular dark field (ADF) image, EDS maps for Mn and O, and SAED pattern from the particle shown. The electron diffraction pattern is close to a $[221]$ zone axis for bixbyite.

5.3.2 Electrochemical performance

Cyclic voltammetry (CV) and galvanostatic charge-discharge (GCD) cycling tests were used to determine the electrochemical performance of the as fabricated Mn_2O_3 cathode material. Fig. 5.2a shows the CV curves at a scan rate of 0.25 mV s^{-1} between 1.0 and 1.9 V, with Zn foil as the reference electrode. Two pairs of oxidization/reduction peaks are present, indicating multiple stages for the charge/discharge process. The GCD profiles at current densities ranging from 50 to 2000 mA/g are shown in Fig. 5.2b. The discharge curve exhibits two apparent plateaus at 1.25-1.29 V and 1.35-1.39 V, and the charge curve exhibits plateaus at 1.53-1.55V and 1.57-1.61V. These plateaus correspond with the two pairs of reduction/oxidation peaks in the CV curves.

The rate performance of the electrodes was tested by cycling at multiple current densities of 50, 100, 200, 500, 1000, and 2000 mA/g for 5 cycles each. As shown in Fig. 5.2c, the highly crystalline Mn_2O_3 electrode exhibits excellent rate capability. The electrode delivers discharge capacities of 375, 341, 289, 205, 113, and 65 mAh/g at 50, 100, 200, 500, 1000, and 2000 mA/g, respectively. Also, the capacity of the electrode returns to the original level when the lower current densities are retested, revealing good stability for the electrode. The cells in this work delivered good electrochemical performance, comparable to or better than previous studies (Table 5.1). At lower current densities, the tested single cell has discharge capacities of 375, 341, 289, and 205 mAh/g at 50, 100, 200, and 500 mA/g, respectively, which are better specific capacities relative to previous studies. The performance at higher current densities does not exceed values reported in previous studies, but the performance results are still competitive.

Cycle testing of the electrode was performed at current densities of 500 and 2000 mA/g. Fig. 5.2d shows the cycling performance of the cell at a current density of 500 mA/g for 200 cycles between 1.0 and 1.9 V. A maximum specific capacity of 255 mAh/g can be delivered at this current rate with 93.7% retention of the original capacity after 200 cycles. At 2000 mA/g, the electrode has an initial capacity of 57.2 mAh/g and a final capacity at 41.7 mAh/g after 1100 cycles (73% retention). The Coulombic efficiency is maintained at nearly 100% for the two test conditions, which indicates good stability for the electrode at both lower and higher current densities. Capacity fading phenomena during cycling will be discussed in the last subsection.

Table 5.1. Battery cycling performance comparison for this work and previous studies of bixbyite Mn_2O_3 as the cathode in ZIBs

Specific Capacity (mAh/g)	Current Density (mA/g)													Potential Window & Electrolyte
	50-60	100	150	200	300	500	600	900	1000	1500	1800	2000	3000	
Authors														
Jiang et al [73]		137		100	86	74			57			38		1 V-1.9 V 2 M ZnSO ₄
Mao et al [74]	225	200		175	160	145			120			100	70	0.9 V-1.9 V 2 M ZnSO ₄ + 0.2 M MnSO ₄
Feng et al [75]	292		258		228		206			179			162	1 V-1.8 V 2 M ZnSO ₄ + 0.2 M MnSO ₄
Shen et al [76]		190			150			130			100		85	1 V-1.9 V 2 M ZnSO ₄ + 0.1 M MnSO ₄
Ma et al [77]		228		217					148			131	105	1 V-1.9 V 2 M ZnSO ₄ + 0.1 M MnSO ₄
This work	375	341		289		205			113			65		1 V-1.9 V 2 M ZnSO ₄ + 0.2 M MnSO ₄
Values are determined from data presented in the specific reference.														

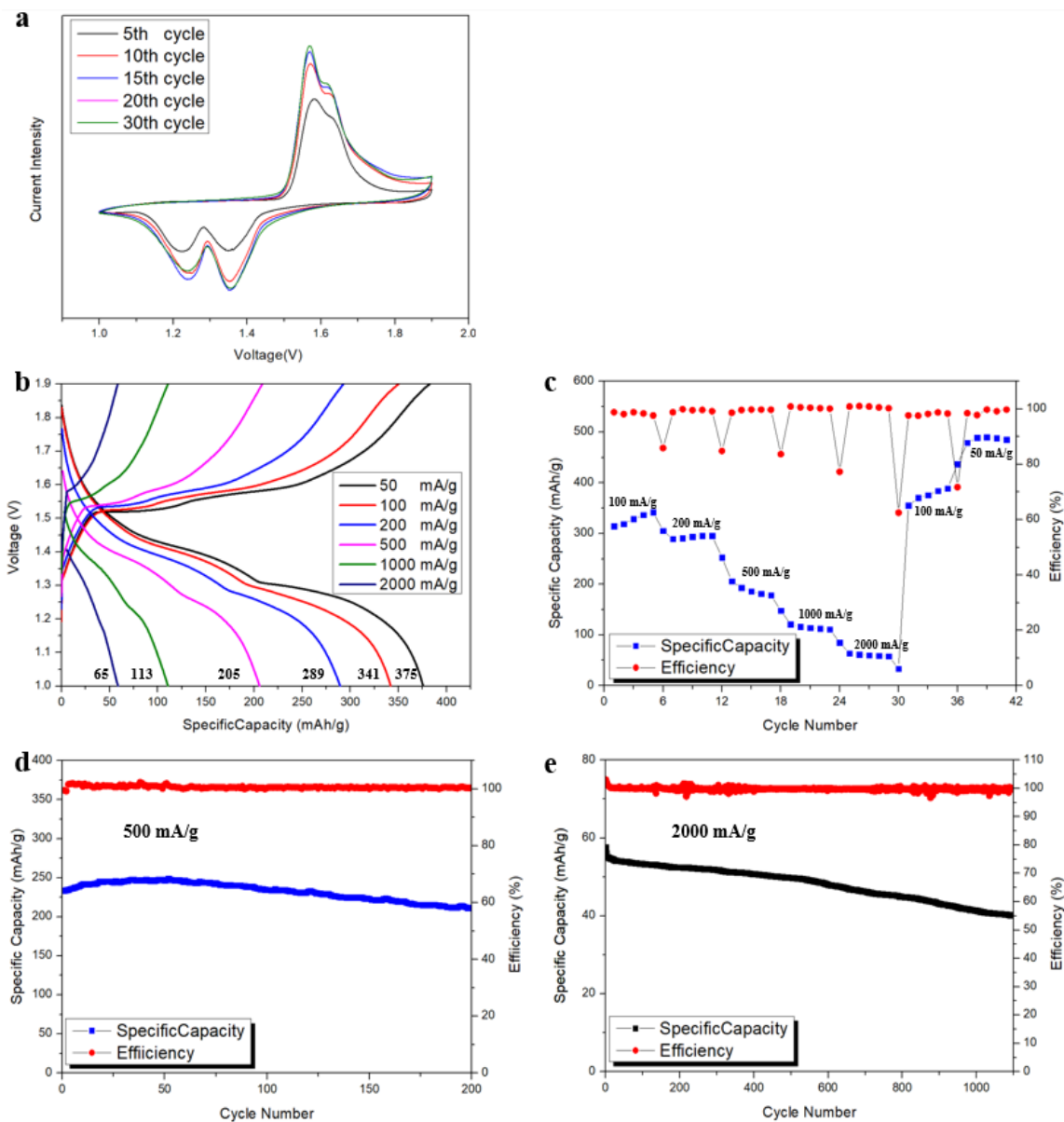


Figure 5.2. (a) CV curves at 0.25 mV s^{-1} . (b) GCD curves at 50, 100, 200, 500, 1000, and 2000 mA/g. (c) Rate capability tests at 50, 100, 200, 500, 1000, and 2000 mA/g and then again at 100 and 50 mA/g. (d) Galvanostatic charge–discharge electrochemical performance at 500 mA/g for 200 cycles. (e) Galvanostatic charge–discharge electrochemical performance at 2000 mA/g for 1100 cycles.

5.3.3 Mechanism investigation

Ex-situ XRD and SEM were carried out to investigate the charge storage mechanism for the Mn_2O_3 cathode of the ZIB. Fig. 5.3a shows the GCD curve for half of the 15th cycle (discharge) and the entire 16th cycle (charge and discharge) at a current density of 200 mA/g. The GCD curve shows two discharge and two charge plateaus for the full cycle, which suggests a two-step reaction mechanism. The discharge plateaus are separated by a “turning point” at position (d). Each of the points on the curve represents stages where the process was stopped, and the electrode was examined ex-situ via XRD and SEM. Select samples were also analyzed using TEM. Fig. 5.3b and 3c, as well as Fig. 5.2.3-2a to 4l, present the ex-situ XRD and SEM analysis for each stage.

Position (a) in Fig. 5.3a corresponds to the fully charged state of the 15th cycle. The peaks in the XRD pattern (Fig. 5.3b) can be indexed to cubic α - Mn_2O_3 (bixbyite) and graphitic carbon (JCPDS 75-2078 – Fig. 5.12). The corresponding SEM image is shown in Fig. 5.2.3-2a and is similar to the electrode morphology before testing. Positions (b) and (c) in Fig. 5.3a show the 1st discharge plateau of the 15th cycle, which precedes the turning point. The XRD patterns for positions (b) and (c) (Fig. 5.3a) can still be indexed to Mn_2O_3 and carbon, with no additional peaks. However, there is a slight change in morphology at position (c) (Fig. 5.2.3-2a), in the form of a few small flakes, which are detectable at higher magnification. Positions (d), (e) and (f) in Fig. 5.3a correspond to the 2nd discharge plateau. Starting at the turning point (d), in addition to the Mn_2O_3 and carbon peaks, the XRD patterns show two additional peaks at 2-theta less than 10° . The intensities of these peaks increase significantly as discharge proceeds (positions (e) and (f)). The peak at 8.6° corresponds to the most intense peak for tetrahydrate Zn sulphate hydroxide ($\text{Zn}_4\text{SO}_4(\text{OH})_6 \cdot 4\text{H}_2\text{O}$ or ZHS*4 H_2O , JCPDS 44-0673 – Fig. 5.13) and the peak at 9.6° corresponds to the most intense peak for trihydrate Zn sulphate hydroxide ($\text{Zn}_4\text{SO}_4(\text{OH})_6 \cdot 3\text{H}_2\text{O}$ or ZHS*3 H_2O , JCPDS 33-0689 – Fig. 5.14). The corresponding SEM images are shown in Fig. 5.2.3-2d to 4f; the formation of ZHS correlates with the appearance of large flakes on the electrode surface during the 2nd discharge plateau (Fig. 5.2.3-2e). The small flakes detected at higher magnification in Fig. 5.2.3-2c and 4d likely correspond to the initial appearance of ZHS.

Positions (g) and (h) in Fig. 5.3a correspond to the almost fully discharged and fully discharged states of the 15th cycle. The ZHS peaks in Fig. 5.3b continue to increase in intensity and reach maximum values at full discharge (position (h)). The corresponding SEM images in Fig. 5.2.3-2g

and 4h show additional ZHS flakes. There are several additional weak peaks that appear in the XRD patterns for positions (g) and (h). These are located at about 17.5°, 19.2°, 21.5°, 27.5°, 28.8°, 34°, 37.5°, and 59° 2-theta and can be attributed to either of the two ZHS phases.

Positions (i), (j) and (k) in Fig. 5.3a correspond to the 1st charge plateau, the 2nd charge plateau, and the fully charged state for the 16th cycle. As with the discharge process, the Mn₂O₃ and carbon peaks remain (Fig. 5.3b), while the intensities of the two strong ZHS peaks (at <10° 2-theta) decrease during charging and completely disappear in the fully charged state, which is an indication that ZHS formation is reversible. The weak ZHS peaks also disappear. The corresponding SEM images are shown in Fig. 5.2.3-2i to 4k; the number and size of ZHS flakes decrease and disappear at full charge. The morphology of the electrode in the fully charged state (Fig. 5.2.3-2k) of the 16th cycle is also similar to the electrode morphology in the previous fully charged state and the morphology before testing. Position (l) in Fig. 5.3a corresponds to the next fully discharged state of the 16th cycle. The two ZHS peaks reappear in the XRD pattern (Fig. 5.3b), as do the ZHS flakes in the SEM image (Fig. 5.3l).

The LHS of Fig. 5.3c shows a magnified view of the 30-50° 2-theta range for the XRD patterns for electrodes during discharge. Pure Mn powder was added to the samples for XRD analysis to act as an internal calibration standard in order to determine any Mn₂O₃ peak shifts that could arise from Zn²⁺ or H⁺ intercalation during discharge. The (411) peak for Mn (Fig. 5.15) at 43.02° 2-theta was used to calibrate the patterns. On the RHS of Fig. 5.3c, an enlarged view of the XRD patterns for the 32-34° 2-theta range is shown. One of the major Mn₂O₃ peaks at ~33.0° is visible and corresponds to the (222) plane. There appears to be a shift to lower angles starting at position (b) from 32.960° to 32.897°, which indicates the possibility of H⁺ and/or Zn²⁺ intercalation into the Mn₂O₃ crystal. Any ion intercalation should increase the d-spacing or reduce the Bragg angle. However, the maximum amount of d-spacing shift for the (222) peak of Mn₂O₃ is only 0.00048 nm, which represents ~0.18% change in the d-spacing. Considering that the ionic radii of the H⁺ and Zn²⁺ ions are 208 pm and 88 pm, respectively, the amount of intercalation appears to be limited. The primary mechanism responsible for the 1st discharge plateau is likely some other process and will be addressed in subsequent paragraphs.

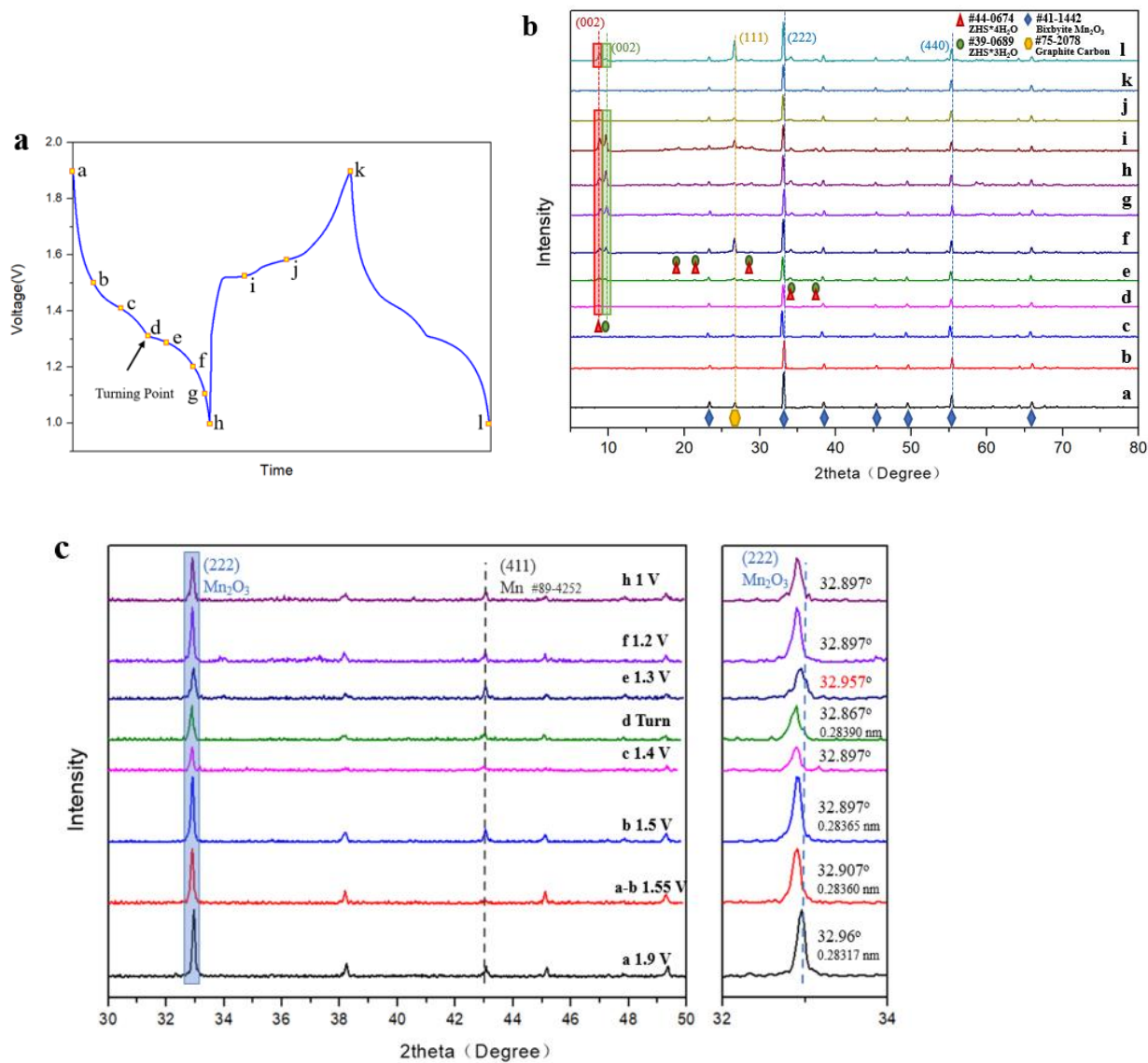


Figure 5.3 (a) GCD curve for the 15th (discharge only) and 16th (charge and discharge) cycles at 200 mA/g. (b) XRD patterns of the cathode for the stages indicated in (a). (c) XRD patterns of the cathode for the discharge conditions in (b) for the 2-theta range of 30° to 50°; the patterns are further enlarged on the right displaying the 2-theta range of 32° to 54° making the (222) peak from Mn₂O₃ more visible. Note the (411) peak for Mn, which was used as an internal standard to quantify any Mn₂O₃ peak shifting.

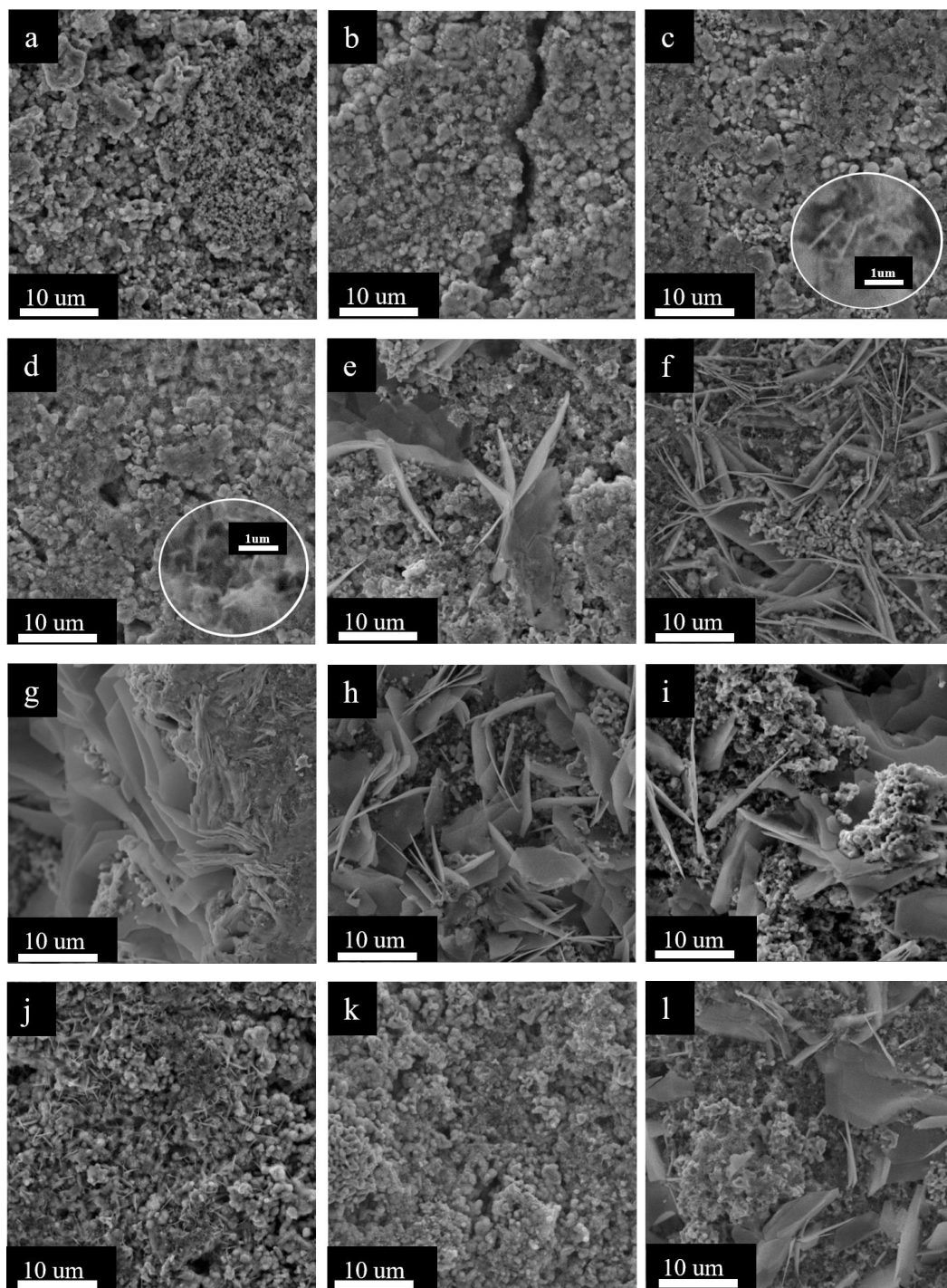


Figure 5.4 Ex-situ SEM images for the various stages shown in Fig. 5.3 during GCD at 200 mA/g. (a) Fully charged state of the 15th cycle; (b) before the first discharge plateau of the 15th cycle; (c) first discharge plateau of the 15th cycle; (d) turning point between the two discharge plateaus of the 15th cycle; (e) second discharge plateau of the 15th cycle; (f) after the second discharge plateau of the 15th cycle; (g) close to full discharge of the 15th cycle; (h) fully discharged state of the 15th cycle; (i) first charge plateau of the 16th cycle; (j) second charge plateau of the 16th cycle; (k) fully charged state of the 16th cycle; (l) fully discharged stage of the 16th cycle.

Further microstructural characterization of select samples was done using TEM/STEM analysis (Fig. 5.5). The samples include the first discharge plateau during the 15th cycle (Fig. 5.4a - position (c) in Fig. 5.3a), the second discharge plateau during the 15th cycle (Fig. 5.4b - position (e) in Fig. 5.3a), the fully discharged state during the 15th cycle (Fig. 5.4c - position (h) in Fig. 5.3a), the first charge plateau during the 16th cycle (Fig. 5.4d - position (i) in Fig. 5.3a), and the fully charged state during the 16th cycle (Fig. 5.4e - position (k) in Fig. 5.3a). For all samples, STEM bright field (BF) images, STEM annular dark field (ADF) images, EDS maps, and electron diffraction patterns were obtained.

Fig. 5.5a shows a sample from the 1st discharge plateau (position (c)). Mn_2O_3 particles are surrounded by another phase which contains Mn, Zn, and O, with smaller amounts of S. An enlarged BF image and an SAED pattern from the red box in the ADF image are also shown. Similar diffraction patterns were obtained from other regions of this sample. Several diffuse rings are present, which indicate that the region is poorly crystalline making indexing difficult. The pattern could not be indexed to any known Zn-S-O or Mn-Zn-S-O phases. The overall EDS spectrum for the enlarged region shows that the major peaks are Mn, Zn, and O, with a much less intense S peak. Since the S concentration is low, it is likely residual S from the electrolyte, which means that the new phase essentially contains Mn, Zn, and O. Attempts were made to index the SAED to known Mn-Zn-O phases; the best fit was to hetaerolite (ZnMn_2O_4 , JCPDS 23-1113 – Fig. 5.16) which is isostructural with hausmannite (Mn_3O_4). One of the rings in the SAED pattern (0.346 nm) corresponds to carbon from the electrode. There is a band of rings with a d-spacing range of ~0.238 to 0.282 nm, which corresponds to multiple d-spacings for hetaerolite and are highlighted in the PDF card for hetaerolite shown in Fig. 5.16. More detailed indexing of the electron diffraction pattern is shown in Fig. 5.17. Further discussion of hetaerolite formation will be provided in a later section. Hetaerolite was not identified in the XRD patterns (Fig. 5.3) and this will be addressed a bit later in the paper.

Fig. 5.5b shows two regions of a sample from the 2nd discharge plateau (position (e)). For the first STEM ADF image, a Mn_2O_3 particle, as well as the Mn-Zn-O phase, identified in the previous paragraph as hetaerolite, are present. There is an additional phase, which is likely ZHS that was identified by XRD (Fig. 5.3b) and SEM (large flakes in Fig. 5.2.3-2) analysis. The second STEM ADF image in Fig. 5.4b shows hetaerolite as well as one of the ZHS flakes. The EDS maps and

overall EDS spectrum, from the second image, show strong Zn, S, and O signals with little or no Mn signal for the flake, which corresponds to ZHS. The SAED pattern from the second image has diffraction rings that can be indexed to both hetaerolite and ZHS.

The fully discharged state (position (h)) is shown in Fig. 5.5c. EDS maps and an SAED pattern from the enlarged region, indicated by the square, are also shown. This region is mostly ZHS with a Mn_2O_3 particle (top LHS of the STEM ADF image). There is still hetaerolite present distributed between the ZHS regions, which means that hetaerolite does not decompose at lower discharge potentials.

A STEM ADF image of the sample from the 1st charge plateau (position (i) - cycle 16) is shown in Fig. 5.5d. Hetaerolite partially surrounds an Mn_2O_3 particle, with ZHS in the lower left portion of the image (EDS spectra). The SAED pattern has rings that can be indexed to both hetaerolite and ZHS. Note the same band of rings (from ~ 0.240 to 0.283 nm) which appeared in the other SAED patterns with hetaerolite. The results indicate that hetaerolite is still present and ZHS has not completely decomposed at this point, which is consistent with the XRD and SEM results (Figs. 3b and 4i).

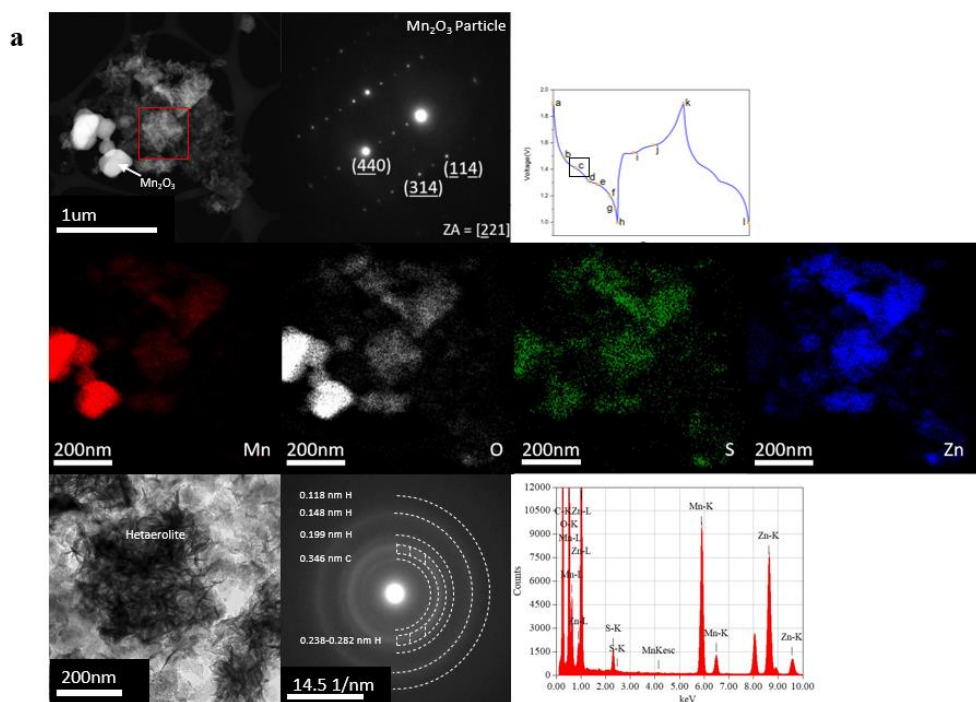
A sample corresponding to the fully charge state (position (k)) is shown in Fig. 5.5e. The first image shows Mn_2O_3 with some hetaerolite adjacent to it, which indicates that hetaerolite formation is not fully reversible. The second image shows another region of hetaerolite, including an SAED pattern and EDS maps and an overall EDS spectrum. The Mn and Zn signals are strong, while the S signal is weaker which is similar to the hetaerolite region in Fig. 5.4a.

The TEM/STEM results essentially corroborate the XRD results. Mn_2O_3 particles were observed for all discharge/charge states and were confirmed through EDS mapping and electron diffraction. There was no clear evidence of $\text{Zn}^{2+}/\text{H}^+$ intercalation in Mn_2O_3 , although the XRD results showed a slight shift of the Mn_2O_3 peaks to lower angles which could be an indication of limited intercalation – perhaps Zn^{2+} and/or H^+ . ZHS was detected by both XRD and TEM analysis. A poorly crystalline Mn-Zn-O rich phase (hetaerolite) was identified from the TEM analysis; it first appeared in the first discharge plateau sample, remained throughout discharge, and did not fully decompose on charging.

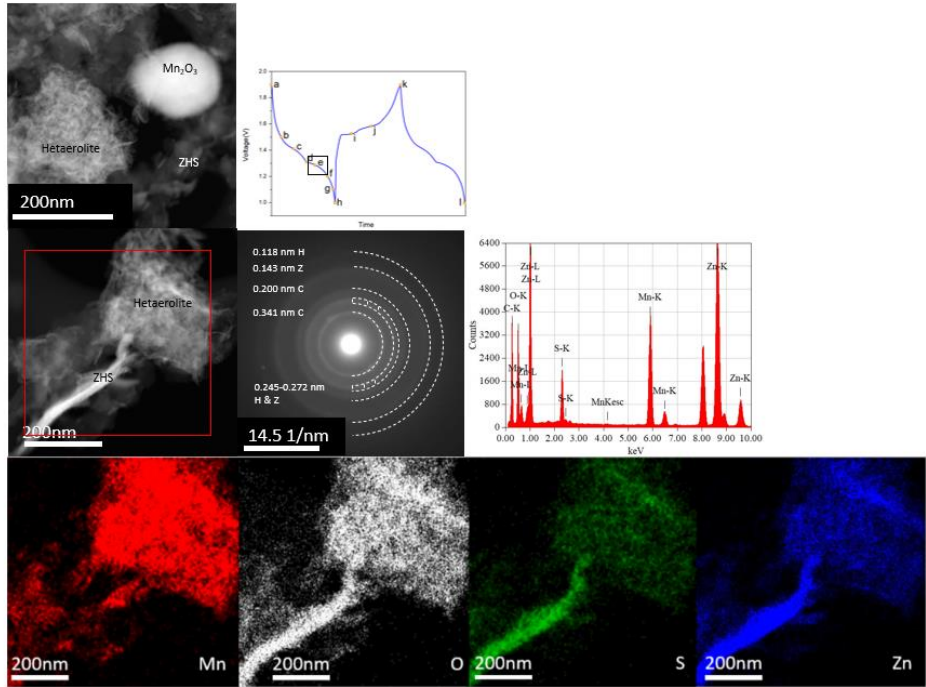
Hetaerolite was not detected during the XRD analysis, which was due in part to the poor crystallinity of the phase. However, electron diffraction patterns with a band of multiple diffuse rings, corresponding to a range of d-spacings from ~0.230 nm to ~0.280 nm, were obtained. The band of d-spacings (0.230 nm to 0.280 nm) would correspond to 2-theta values of ~31.9° to ~39.1° in the XRD patterns. Within this angular range, several reflections for Mn₂O₃ and ZHS appear, including two major reflections ((222) and (400)) for bixbyite Mn₂O₃ at 32.9° and 38.2° and several minor reflections for ZHS. These ZHS reflections are indicated by the blue shaded regions in Fig. 5.13 and 5.14. The hetaerolite electron diffraction patterns also have rings with d-spacings (in decreasing order) of about 0.199 - 0.204 nm, 0.117 nm, 0.115 nm, 0.111-0.112 nm, and 0.101-0.103 nm. These d-spacings would correspond to 2-theta values for XRD of about 44.6° to 45.5°, 82.6°, 84.1° and over 85°. Peaks at 45.1 - 45.3° overlap with or are very close to the (332) plane for Mn₂O₃ and the (010) plane for graphitic carbon, leading to interference. In addition, the Mn-Zn-O phase is poorly crystalline, so sharp, intense XRD peaks are unlikely. Peaks at 2-theta angles exceeding 80° are out of the 2-theta angular range examined by XRD (Fig. 5.3b). As such, additional X-ray scans were done in the 2-theta angular range of 80-85° for select samples and the patterns are shown in Fig. 5.6 Two weak peaks are visible at 82.5° and 83.9° 2-theta, which correlate with the SAED rings with d-spacings of 0.117 nm and 0.115 nm and can be indexed to hetaerolite (316) and (008) crystal planes. The two hetaerolite peaks are also present for the rest of discharge states and the initial charge states but are weak for the fully charged state (position (a)).

Further confirmation for the formation of hetaerolite was obtained by preparing an electrode with Ti as the current collector. All previous electrodes used carbon as the current collector, which resulted in carbon being mixed with the electrode material (Mn₂O₃ plus any phases that formed during discharge). Note that TEM samples were prepared by scraping the electrode material from the current collector which invariably led to some carbon being removed as well and carbon rings appearing in SAED patterns. The use of Ti as the current collector eliminated this carbon source. Fig. 5.7 shows a sample from the discharge turning point (position (d) of the 15th cycle) of an electrode with a Ti foil current collector. A Mn₂O₃ oxide particle is visible and is surrounded by hetaerolite, which was confirmed by the SAED pattern and EDS analysis. A high resolution (HR) TEM image from part of the hetaerolite is also shown. The poor crystallinity of the hetaerolite

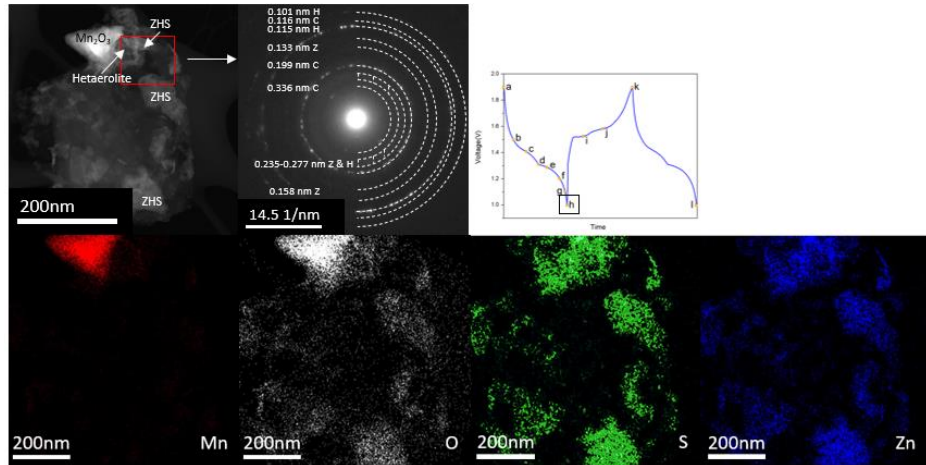
phase is evident, although there are localized crystalline regions. The d-spacing of 0.267 nm corresponds to (103) planes for hetaerolite. Fig. 5.18 shows additional TEM analysis for the fully discharged (15th cycle) and fully charged states (16th cycle) for electrodes with a Ti current collector. Regions with hetaerolite were identified in both cases.



b



c



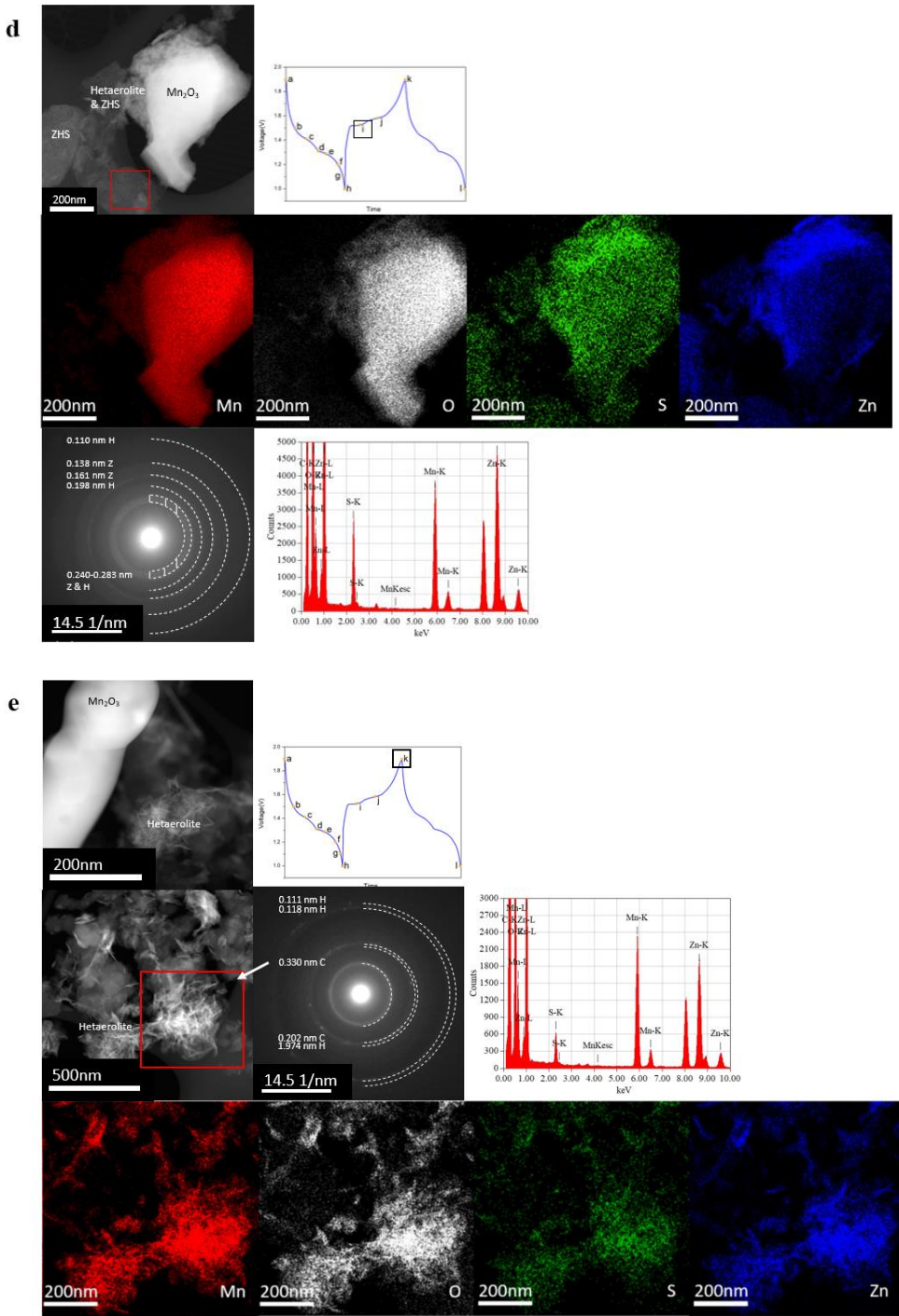


Figure 5.5 Ex-situ STEM ADF images, EDS maps, overall EDS spectra and SAED patterns of the Mn₂O₃ electrode at different stages of discharge and charge: (a) First discharge plateau (position (c)) of the 15th cycle; (b) second discharge plateau (position (e)) of the 15th cycle; (c) fully discharged state of the 15th cycle (position (h)); (d) first charge plateau stage of the 16th cycle (position (i)); (e) fully charged stage of the 16th cycle (position (k)). Note that the C, H and Z labels for the diffraction patterns correspond to carbon, hetaerolite, and ZHS, respectively.

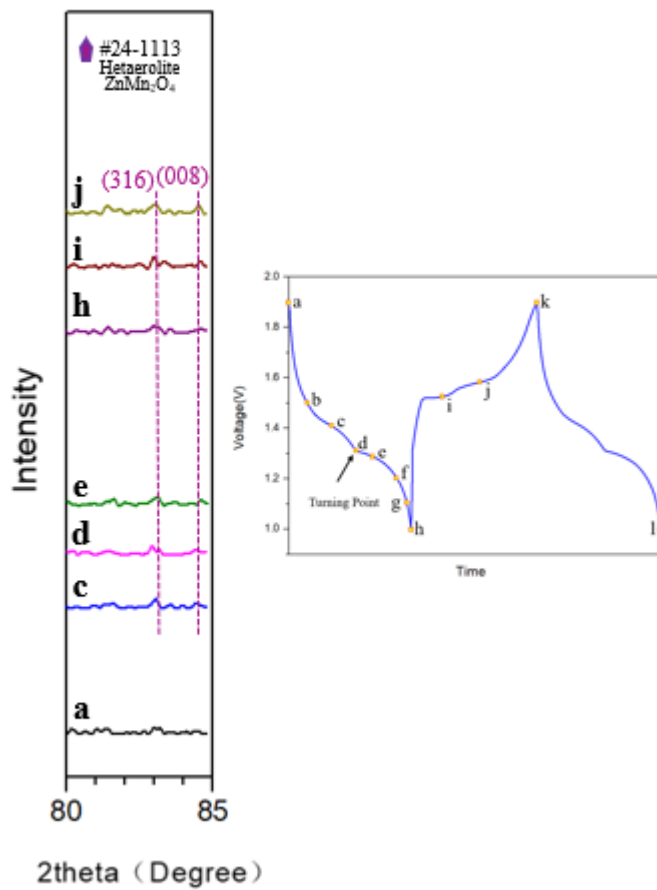


Figure 5.6 XRD patterns of the cathode for 2-theta in the 80° to 85° range for the stages shown.

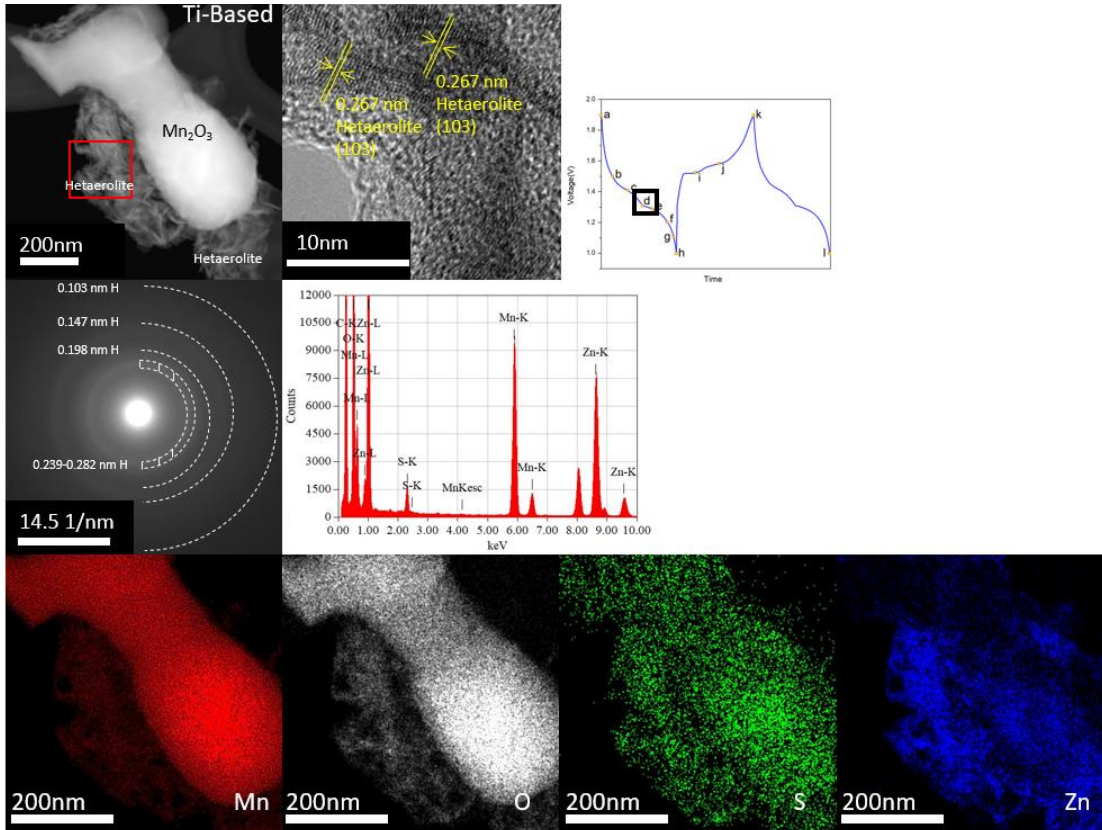


Figure 5.7 Ex-situ STEM ADF image, EDS maps, overall EDS spectrum, SAED pattern, and HRTEM image of the electrode with a Ti current collector at position (d) (turning point) of discharge for the 15th cycle.

Based on the microstructural analysis and electrochemical results, the following discharge/charge processes are proposed. During initial discharge (from position (a) to position (b) in Fig. 5.3a), there appears to be some intercalation. This could be H⁺ and/or Zn²⁺ ions. The amount of shift is small (the d-spacing increases from 0.28317 nm to 0.28365-0.28390 nm or less than 0.2% change) and remains about the same as discharge proceeds. In any case, the amount of intercalation is minimal. As discharge continues, from position (b) through (c) and (d) (the first plateau in Fig. 5.3a), hetaerolite forms through a chemical conversion reaction with bixbyite (Mn₂O₃). There are no electrons involved.



This reaction has been identified by Rubel et al [22] in their study on the electrochemical stability of ZnMn₂O₄. Their proposed Mn-Zn-H₂O Pourbaix diagram is redrawn in part in Fig. 5.8

for the pH range of 3 to 8, where line 1 corresponds to Reaction [5.1]. Note that potentials utilized during discharge in this work correspond to a range of 1.9 V to 1.0 V vs. Zn/Zn²⁺ and the initial pH of the electrolyte is 3.27 (labeled as a vertical line in Fig. 5.7). Based on the Pourbaix diagram, decomposition of Mn₂O₃ to hetaerolite (ZnMn₂O₄) occurs at pH values close to 5 and above. The increase in pH needed for the reaction could occur through the partial dissolution of Mn₂O₃, which generates hydroxyl ions.

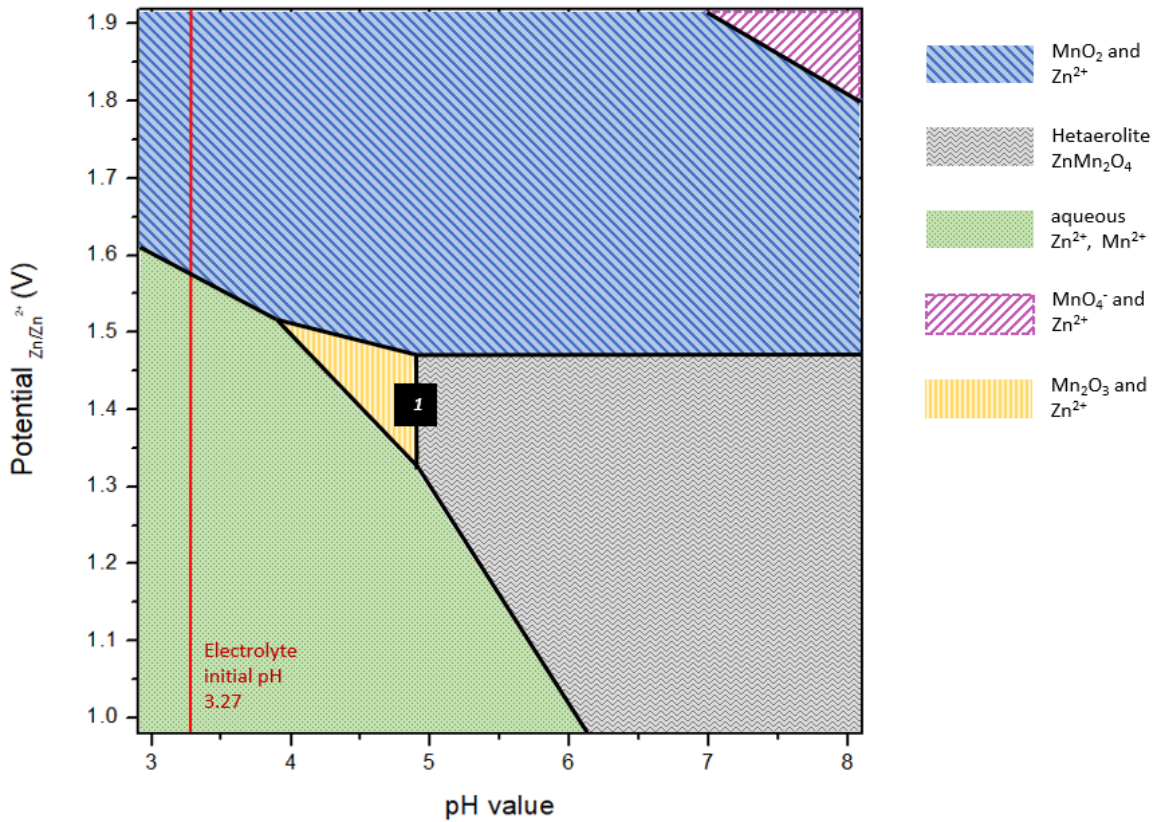
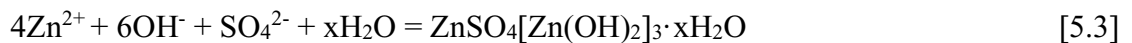


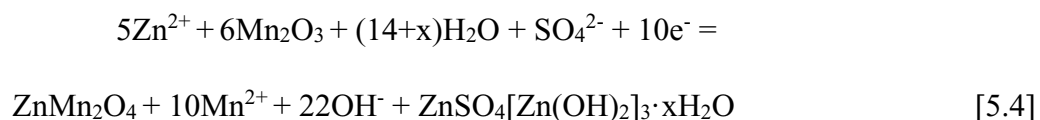
Figure 5.8 Mn-Zn-H₂O Pourbaix diagram with ZnMn₂O₄ phase boundaries; redrawn from [105] .



As discharge continues, from position (d) through the 2nd plateau at positions (e)-(f) and finally to position (h) (Fig. 5.3a), ZHS forms according to the following chemical reaction [54]:



The overall cathode and anode reaction during discharge can then be written as:



To confirm the hypothesis that the source of hydroxyl ions is Mn oxide dissolution, a rotating ring-disk electrode (RRDE) test was performed. The RRDE test was set up by utilizing the Mn_2O_3 -based electrode as the working electrode and monitoring the current from the ring electrode. During linear sweep voltammetry (LSV) of the disk electrode, the reaction products are swept to the outer ring electrode by rotation of the motor. The potentiostat can monitor the current generated by the product at the ring electrode. The LSV curve and corresponding ring electrode current, obtained by scanning from the open circuit potential (OCV) of 1.4 V to 0.9 V, are shown in Fig. 5.9 The Pt ring electrode was maintained at 1.91 V to ensure that any aqueous Mn^{2+} ions produced by the dissolution reaction are oxidized back to Mn^{3+} . A significant current is detected on the ring electrode at ~ 1.36 V, which corresponds to the onset of significant Mn dissolution and the potential of the 1st discharge plateau. The current continues to increase during the discharge process which suggests that Mn oxide dissolution occurs throughout the entire discharge process. Mn oxide dissolution during discharge can locally increase the pH value in the vicinity of the Mn_2O_3 electrode. When the pH value reaches a high enough value, Mn_2O_3 can transform to hetaerolite.

Mn_2O_3 dissolution during battery cycling was confirmed through atomic absorption spectroscopy (AAS) measurements (Fig.5.10). Samples of the electrolyte were analyzed at various fully charged states of cycling, from 0 to 50 cycles where 0 cycles correspond to the pristine electrolyte before testing. Note that the original Mn concentration in the electrolyte, as measured by AAS, is 0.2143 M which is close to the 0.2 M concentration of MnSO_4 added. With cycling, there is a clear increase in Mn concentration in the electrolyte, which not only indicates that Mn_2O_3 dissolution is occurring but that the dissolution reaction (Reaction 5.2 above) is not fully reversible. The accumulation of Mn in the electrolyte during cycling will affect the battery performance and cyclability.

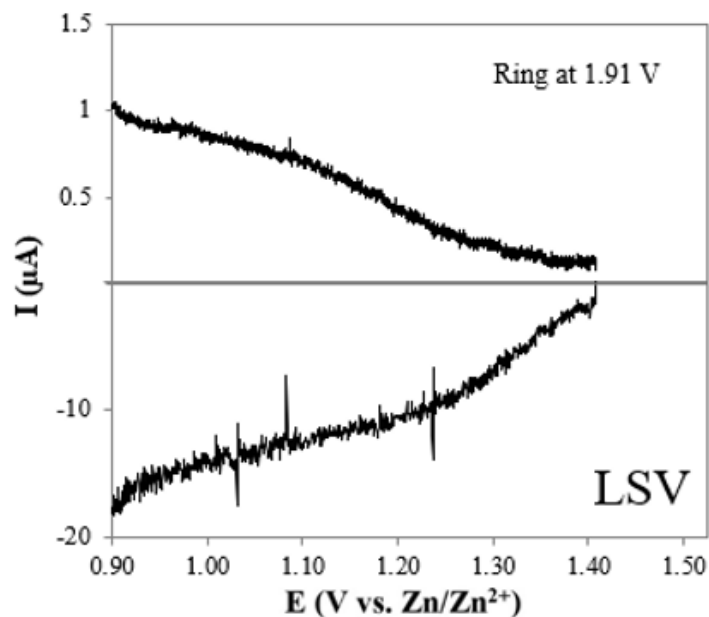


Figure 5.9 RRDE profile for the Mn_2O_3 electrode with a scan rate at 1 mV s^{-1} in $2 \text{ M ZnSO}_4 + 0.2 \text{ M MnSO}_4$ solution, stirred at 900 rpm with the Pt ring electrode maintained at 1.91 V vs Zn/Zn^{2+} .

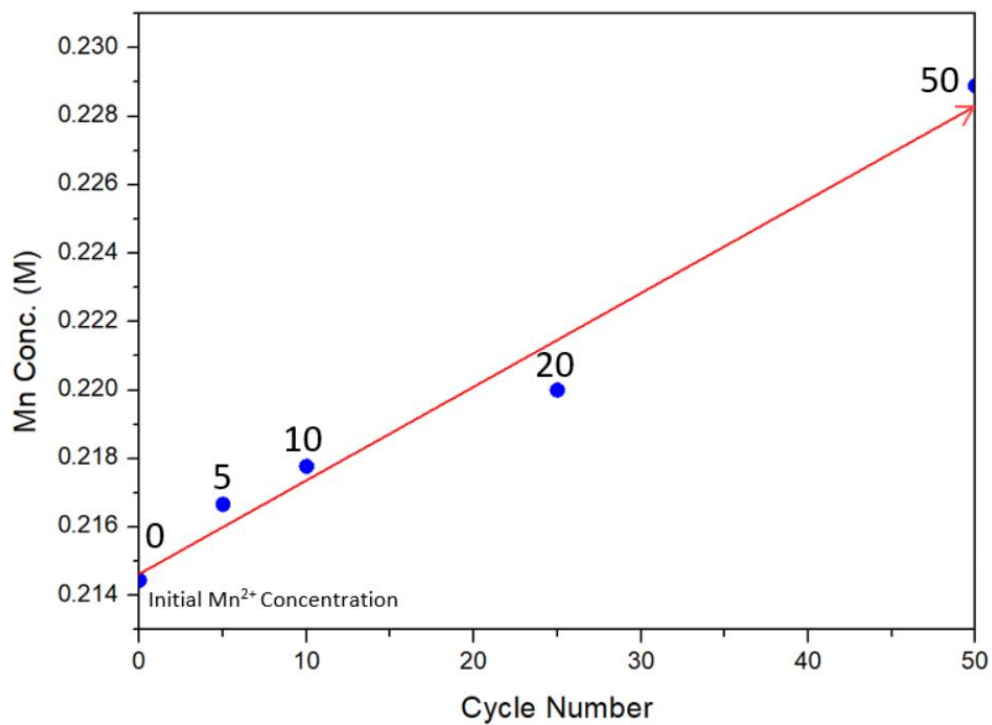


Figure 5.10 AAS results showing the Mn concentration in the electrolyte after various battery cycles.

There have been several previous studies that have examined the use of Mn_2O_3 as the cathode for ZIBs [73-78]. The mechanisms proposed in these studies are summarized in Table 5.2 and discussed in the following paragraphs in relation to the results from the current study. Note that for all these studies, the CV and GCD curves are similar with two plateaus during both the discharge and charge processes. In addition, the researchers all propose that the discharge process involves some type of intercalation of Zn^{2+} and/or H^+ ions. This is in contrast to our work, where intercalation is not a major contributor to the discharge process. Instead, both plateaus are proposed to be due to chemical processes, involving the formation/decomposition of heterolite (ZnMn_2O_4) and Zn sulphate hydroxide (ZHS).

Table 5.2. Charge storage mechanism comparison for this work and previous studies of bixbyite Mn_2O_3 as the cathode for ZIBs

Author Name	Cathode	Anode	Potential Window	Electrolyte	Charge Storage Mechanisms
Jiang et al [73]	Mn_2O_3 (cubic)	Zn Metal	1 V-1.9 V	2 M ZnSO_4	<ul style="list-style-type: none"> Mn_2O_3 transformed to layered-type Zn-birnessite Zn ion intercalation/extraction
Mao et al [74]	Mn_2O_3 (cubic)	Zn Metal	0.9 V-1.9 V	2 M ZnSO_4 + 0.2 M MnSO_4	<ul style="list-style-type: none"> Mn_2O_3 transformed to layered-type Zn-birnessite Zn^{2+} and H^+ intercalation/extraction
Feng et al [75]	Mn_2O_3 (ortho)	Zn Metal	1 V-1.8 V	2 M ZnSO_4 + 0.2 M MnSO_4	<ul style="list-style-type: none"> MnO formed during H^+ intercalation ZHS formation Zn^{2+} and H^+ intercalation/extraction
Shen et al [76]	Mn_2O_3 (cubic)	Zn Metal	1 V-1.9 V	2 M ZnSO_4 + 0.1 M MnSO_4	<ul style="list-style-type: none"> Zn^{2+} and H^+ intercalation/extraction
Ma et al [77]	Mn_2O_3 (cubic)	Zn Metal	0.8 V-1.9 V	3 M ZnSO_4 + 0.2 M MnSO_4	<ul style="list-style-type: none"> Birnessite MnO_2 formed during cycling and acted as a host for Zn^{2+} and H^+ intercalation/extraction ZHS formation
Yang et al [78]	Mn_2O_3 (cubic)/ ZnMn_2O_4 (#23-1113)	Zn Metal	0.8 V-1.9 V	1 M ZnSO_4	<ul style="list-style-type: none"> Mn_2O_3 transformed to layered-type Zn-birnessite ZnMn_2O_4 listed as energy storage cathode
This work	Mn_2O_3 (cubic)	Zn Metal	1 V-1.9 V	2 M ZnSO_4 + 0.2 M MnSO_4	<ul style="list-style-type: none"> Heterolite formation and ZHS formation (chemical reactions)

The initial work done on Mn_2O_3 electrodes was by Jiang et al in 2017 [73]. They reported the formation during discharge of flake-like features on the surface of the Mn_2O_3 electrode; these are very similar in appearance to the flakes on our electrodes which were identified as ZHS. They attributed the flakes to layered Zn-birnessite, which was proposed to form from the original Mn_2O_3 through intercalation. Their identification was based on XRD analysis of the electrode before and after discharge. After discharge, three additional peaks at 12.2° (0.725 nm), 25.3° (0.352 nm), and 35.0° (0.256 nm) were present relative to the pristine electrode. These peaks were

identified as belonging to Zn-birnessite, although the manner in which the pattern was indexed was not shown. The three peaks could be also indexed to ZHS, as was shown in this work. In addition, Jiang et al only showed EDS analysis from one particle in the TEM with no electron diffraction; EDS analysis in the SEM over a larger region would have been more convincing. Jiang et al also claimed that their electrode was fully reversible, i.e., the Mn_2O_3 to Zn-birnessite reaction; however, weak peaks at 25.3 and 35.0° remained after full charging. One difference between Jiang et al.'s work and this work is that their electrolyte did not contain MnSO_4 , which is interesting because the absence of MnSO_4 in the electrolyte would likely enhance Mn dissolution, making ZHS formation more likely.

Feng et al also examined Mn_2O_3 as the electrode for ZIBs [75]. They claimed that their Mn_2O_3 had an orthorhombic crystal structure; however, their XRD pattern matches well with the cubic form (bixbyite, PDF #41-1442) which is the stable form of Mn_2O_3 . All other references [73, 74, 76, 77, 78], as well as the current work, show that Mn_2O_3 has the more common cubic structure. Their capacity curves are similar in shape to the ones in this work and those by Jiang et al [73] as well as the other references. Only one SEM image of the electrode was shown along with several TEM images of limited areas. Feng et al propose that Zn^{2+} is reversibly removed from the electrode, based on XPS and XRD data. The XPS results indicate a $\text{Mn}^{3+}/\text{Mn}^{2+}$ ratio of ~ 2 before discharge. This is puzzling, since the pristine material should have a Mn valence of $3+$. For the XRD patterns, Feng et al report that the Mn_2O_3 peaks shift to lower angles during discharge, which they attribute to lattice expansion due to Zn^{2+} intercalation. This may be the case; however, there is no indication that the patterns were calibrated with some type of standard. The XRD patterns in this work were calibrated using Mn powder, specifically the (411) reflection, to ensure that any peak shifts were not due to measurement errors. Feng et al also report that orthorhombic MnO forms during discharge, although the stable form of MnO is cubic (NaCl-type structure). This assertion is based on XRD peaks at 35.2° (0.255 nm), 52.5° (0.174 nm), and 58.0° (0.159 nm). The closest orthorhombic MnO peaks are at 36.4° , 52.6° , and 58.6° , corresponding to (021), (201), and (152) planes, respectively. These peaks could be indexed to ZHS. Feng et al have indicated that ZHS forms during discharge, but they provided no images to show the morphology. In addition, the lowest 2-theta angle in their XRD patterns is 30° , which is not low enough to show the major ZHS peaks which appear at 2-theta less than 10° . Their TEM images supposedly show MnO, based

on lattice measurement spacings, but there are no EDS spectra or electron diffraction patterns for confirmation. In the end, the authors propose that during discharge that there is a combination of Zn^{2+} intercalation in Mn_2O_3 , MnO formation, and ZHS formation with all processes being reversible.

A recent study on Mn_2O_3 was published by Mao et al [74]. They report both H^+ and Zn^{2+} ion intercalation into Mn_2O_3 during discharge, with H^+ intercalation occurring at higher voltages (1st plateau) and Zn^{2+} intercalation at lower voltages (2nd plateau). Their evidence for Zn^{2+} intercalation is a “large” shift of the (222) and (400) peaks for Mn_2O_3 to lower angles in the XRD patterns. The shift is only ~0.6%, which brings into question whether the shift is actually large. In addition, there is no indication that the XRD patterns were calibrated to ensure that shift measurements are indeed real. Their XRD patterns show extra peaks at ~10°, 15°, 20°, and 25° 2-theta, which they attribute to the intercalated structure, but they did not index those peaks to any particular structure. Their SEM images, after discharge, show numerous surface flakes which are claimed to be the Zn intercalated phase. There is no EDS analysis to support this. The flakes resemble the ZHS flakes seen in our work and the work by Jiang et al [73]. They also claim that Zn sulfate forms at lower potentials and current densities.

Ma et al have investigated the intercalation mechanism in bixbyite ($\alpha\text{-Mn}_2\text{O}_3$). Their electrolyte had a higher ZnSO_4 concentration (3 M) than this work and others and utilized a stainless-steel current collector. Their mechanism study focused on the 1st discharge/charge and 2nd discharge/charge cycles. Their 1st discharge cycle had only one plateau, with two plateaus for subsequent cycles. For the 1st discharge cycle, they report that Mn_2O_3 undergoes an irreversible transition to $\text{L-Zn}_x\text{MnO}_2$ (involves partial reduction of Mn from 3+ to 2+) coupled with Mn^{2+} and OH^- dissolution leading to ZHS formation. As with other researchers, Ma et al used XRD to study the discharge/charge processes. During discharge, three new peaks appeared at 2-theta angles of 12.7° (0.697 nm), 25.4° (0.350 nm), and 37.2° (0.242 nm), which were attributed to layered $\text{L-Zn}_x\text{MnO}_2$. Three other new peaks also appeared, at 8.5° (1.040 nm), 33.8° (0.265 nm), and 25.2 to 29.5° (0.353 nm to 0.303 nm) and were attributed to ZHS. The capacity for the 2nd discharge was slightly higher than that for the 1st discharge, which was explained as being due to an amorphous Mn (4+) compound. The layered-type $\text{L-Zn}_x\text{MnO}_2$ that formed allowed for reversible Zn^{2+} de-/intercalation during further cycles. This reversible process occurs along with repeated dissolution-

deposition of Mn^{2+} on the cathode surface and H^+ intercalation/extraction. A self-regulating process of electrolyte assisted formation/dissolution of flake-like ZHS occurs as well. Ma et al also report that MnO_2 , derived from $\text{L-Zn}_x\text{MnO}_2$ and Mn^{2+} dissolved in the electrolyte, is the actual host for the intercalation of H^+ , rather than $\alpha\text{-Mn}_2\text{O}_3$ itself.

There are two other papers that have examined Mn_2O_3 electrodes. In both cases, there was no detailed microstructural analysis; the authors referenced the work by Jiang et al when proposing mechanisms. In the work by Shen et al [76], MnO_2 was compared with Mn_2O_3 and the two potential plateaus during discharge of Mn_2O_3 are claimed to be due to H^+ and Zn^{2+} ion intercalation, respectively [77]. Yang et al [78] synthesized a composite material of $\text{ZnMn}_2\text{O}_4/\text{Mn}_2\text{O}_3$ and claim that Mn_2O_3 undergoes a phase transformation to Zn birnessite (ZnMn_2O_3), with Zn^{2+} intercalation to Zn birnessite being responsible for the charge storage mechanism.

5.4 Conclusions

In this work, highly crystalline Mn_2O_3 (bixbyite) was synthesized via precipitation and calcination and was utilized as the cathode for an aZIB. Multiple characterization methods were used to determine the morphology and structure of the cathode, before and after cycling. The cells delivered good electrochemical performance, cyclability, and stability. Discharge capacities of testing cells reached as high as 375 mAh/g at 50 mA/g current density and 65 mAh/g at 2000 mA/g current density. A specific capacity of 211 mAh/g was achieved after 200 cycles at a current density of 500 mA/g, corresponding to 93% capacity retention. In addition, 73% capacity retention was realized after 1100 cycles at a current density of 2000 mA/g. A new energy storage mechanism for bixbyite Mn_2O_3 was proposed. Microstructural analysis, using X-ray diffraction (XRD) and electron microscopy, showed that intercalation of either Zn^{2+} or H^+ in Mn_2O_3 may occur to some extent but is not the principal mechanism during discharge. Instead, the mechanism proposed here involves two chemical conversion reactions resulting in the formation of hetaerolite (ZnMn_2O_4) during the 1st discharge plateau followed by Zn hydrate sulfate (ZHS) formation during the 2nd discharge plateau. Capacity fading during cycling of the Mn_2O_3 electrode is linked to Mn_2O_3 dissolution and incomplete reversibility of the hetaerolite reaction.

5.5. Supporting information

PDF#41-1442: QM=Common(+); d=Diffraction; I=(Unknown)												PDF Card	
Bixbyite-C, syn													
Mn ₂ O ₃													
Radiation=CuKα1				Lambda=1.5406				Filter=					
Calibration=				2T=18.845-118.327				I/Ic(RIR)=4.5					
Ref: Level-1 PDF													
Cubic, Ia-3(206)								Z=16		mp=			
CELL: 9.4091 x 9.4091 x 9.4091 <90.0 x 90.0 x 90.0>								P.S=					
Density(c)=4.95		Density(m)=		Mwt=		Vol=833.0							
Ref: Ibid.													
Strong Lines: 2.72/X 1.66/3 3.84/2 2.35/1 1.42/1 1.85/1 2.01/1													
48 Lines, Wavelength to Compute Theta = 1.54056?(Cu), I%-Type = (Unknown)													
#	d(?)	I(f)	(h k l)	2-Theta	Theta	1/(2d)	#	d(?)	I(f)	(h k l)	2-Theta	Theta	1/(2d)
1	4.7050	1.0	(2 0 0)	18.845	9.423	0.1063	25	1.1949	1.0	(6 5 1)	80.277	40.139	0.4184
2	3.8420	16.0	(2 1 1)	23.131	11.566	0.1301	26	1.1761	1.0	(8 0 0)	81.831	40.915	0.4251
3	2.7160	100.0	(2 2 2)	32.951	16.476	0.1841	27	1.1582	1.0	(8 1 1)	83.375	41.687	0.4317
4	2.5140	2.0	(3 2 1)	35.684	17.842	0.1989	28	1.1409	1.0	(8 2 0)	84.932	42.466	0.4383
5	2.3520	14.0	(4 0 0)	38.234	19.117	0.2126	29	1.1247	1.0	(6 5 3)	86.452	43.226	0.4446
6	2.2194	1.0	(4 1 1)	40.616	20.308	0.2253	30	1.1088	1.0	(8 2 2)	88.006	44.003	0.4509
7	2.1041	1.0	(4 2 0)	42.949	21.474	0.2376	31	1.0938	1.0	(8 3 1)	89.534	44.767	0.4571
8	2.0053	8.0	(3 3 2)	45.178	22.589	0.2493	32	1.0792	2.0	(6 6 2)	91.082	45.541	0.4633
9	1.9202	1.0	(4 2 2)	47.300	23.650	0.2604	33	1.0654	1.0	(7 5 2)	92.605	46.302	0.4693
10	1.8452	9.0	(4 3 1)	49.347	24.674	0.2710	34	1.0520	1.0	(8 4 0)	94.143	47.072	0.4753
11	1.7182	2.0	(5 2 1)	53.270	26.635	0.2910	35	1.0391	1.0	(8 3 3)	95.684	47.842	0.4812
12	1.6629	28.0	(4 4 0)	55.189	27.595	0.3007	36	1.0266	1.0	(8 4 2)	97.236	48.618	0.4870
13	1.6136	1.0	(4 3 3)	57.027	28.514	0.3099	37	1.0147	1.0	(9 2 1)	98.774	49.387	0.4928
14	1.5682	1.0	(6 0 0)	58.837	29.419	0.3188	38	1.0030	1.0	(6 6 4)	100.345	50.172	0.4985
15	1.5263	3.0	(6 1 1)	60.619	30.310	0.3276	39	0.9919	1.0	(8 5 1)	101.895	50.948	0.5041
16	1.4876	1.0	(6 2 0)	62.370	31.185	0.3361	40	0.9704	1.0	(9 3 2)	105.080	52.540	0.5153
17	1.4520	4.0	(5 4 1)	64.078	32.039	0.3444	41	0.9602	1.0	(8 4 4)	106.683	53.341	0.5207
18	1.4180	13.0	(6 2 2)	65.806	32.903	0.3526	42	0.9505	1.0	(9 4 1)	108.269	54.134	0.5260
19	1.3872	3.0	(6 3 1)	67.460	33.730	0.3604	43	0.9409	1.0	(10 0 0)	109.902	54.951	0.5314
20	1.3581	2.0	(4 4 4)	69.107	34.553	0.3682	44	0.9316	1.0	(10 1 1)	111.550	55.775	0.5367
21	1.3307	1.0	(5 4 3)	70.740	35.370	0.3757	45	0.9226	1.0	(10 2 0)	113.211	56.606	0.5419
22	1.3050	1.0	(6 4 0)	72.350	36.175	0.3831	46	0.9139	1.0	(9 4 3)	114.884	57.442	0.5471
23	1.2807	1.0	(7 2 1)	73.948	36.974	0.3904	47	0.9054	1.0	(10 2 2)	116.589	58.295	0.5522
24	1.2575	1.0	(6 4 2)	75.548	37.774	0.3976	48	0.8971	1.0	(10 3 1)	118.327	59.163	0.5574

Figure 5.11. JCPDS 41-1442, Bixbyite Mn₂O₃ standard PDF card.

PDF#75-2078: QM=Calculated; d=Calculated; I=(Unknown)												PDF Card	
Graphite													
C													
Radiation=CuKα1				Lambda=1.5406				Filter=					
Calibration=				2θ=26.611-87.327				I/Ic(RIR)=2.32					
Ref. Level-1 PDF													
Rhombohedral, R-3m(166)										Z=2		mp=	
CELL: 3.635 x 3.635 x 3.635 <39.49 x 39.49 x 39.49>										P.S=			
Density(c)=2.281		Density(m)=		Mwt=		Vol=17.5							
Ref. Ibid.													
Strong Lines: 3.35/X 2.08/1 1.96/1 1.67/1													
10 Lines, Wavelength to Compute Theta = 1.54056?(Cu), I%-Type = (Unknown)													
#	d(?)	I(f)	(h k l)	2-Theta	Theta	1/(2d)	#	d(?)	I(f)	(h k l)	2-Theta	Theta	1/(2d)
1	3.3470	100.0	(1 1 1)	26.611	13.305	0.1494	6	1.4602	1.4	(2 2 1)	63.675	31.838	0.3424
2	2.0808	11.3	(0 1 0)	43.453	21.727	0.2403	7	1.2280	3.2	(-1 1 0)	77.695	38.847	0.4072
3	1.9585	7.2	(1 1 0)	46.320	23.160	0.2553	8	1.1893	1.0	(2 3 2)	80.736	40.368	0.4204
4	1.6735	5.0	(2 2 2)	54.810	27.405	0.2988	9	1.1529	4.9	(1 2 0)	83.847	41.923	0.4337
5	1.6228	4.0	(1 1 2)	56.675	28.337	0.3081	10	1.1157	0.7	(3 3 3)	87.327	43.663	0.4482

Figure 5.12. JCPDS 75-2078, graphitic carbon standard PDF card.

PDF#44-0673: QM=Common(+); d=Diffractometer; l=(Unknown)													PDF Card	
Zinc Sulfate Hydroxide Hydrate Zn4SO4(OH)6I4H2O														
Radiation=CuKa1					Lambda=1.5406					Filter=				
Calibration=					2T=8.520-66.978					I/Ic(RIR)=				
Ref: Level-1 PDF														
Triclinic(Unknown),										Z=4		mp=		
CELL: 8.364 x 8.366 x 20.677 <90.06 x 89.93 x 120.11>										P.S=				
Density(c)=2.82			Density(m)=			Mwt=			Vol=1251.6					
Ref: Ibid.														
Strong Lines: 5.18/X 10.37/X 3.11/X 2.65/9 3.25/7 2.42/7 3.45/6 5.94/4														
41 Lines, Wavelength to Compute Theta = 1.54056?(Cu), I%-Type = (Unknown)														
#	d(?)	I(f)	(h k l)	2-Theta	Theta	1/(2d)	#	d(?)	I(f)	(h k l)	2-Theta	Theta	1/(2d)	
1	10.3700	100.0	(0 0 2)	8.520	4.260	0.0482	22	2.0060	3.0	(3 1 0)	45.162	22.581	0.2493	
2	7.2400	2.0	(0 1 0)	12.215	6.107	0.0691	23	1.9870	3.0	(-1 0 10)	45.618	22.809	0.2516	
3	5.9400	40.0	(1-1 2)	14.902	7.451	0.0842	24	1.9750	4.0	(-3 0 6)	45.911	22.955	0.2532	
4	5.1800	100.0	(0 0 4)	17.104	8.552	0.0965	25	1.9340	5.0	(-2-2 4)	46.942	23.471	0.2585	
5	4.2100	32.0	(1-1 4)	21.085	10.542	0.1188	26	1.8780	29.0	(-3 1 8)	48.430	24.215	0.2662	
6	4.1900	32.0	(-1 2 0)	21.187	10.593	0.1193	27	1.7840	4.0	(-4 4 2)	51.160	25.580	0.2803	
7	3.8800	5.0	(1-2 2)	22.902	11.451	0.1289	28	1.7340	7.0	(-4 1 6)	52.747	26.374	0.2884	
8	3.6300	4.0	(-2 2 0)	24.502	12.251	0.1377	29	1.7240	9.0	(0 0 12)	53.077	26.538	0.2900	
9	3.4500	62.0	(0 0 6)	25.802	12.901	0.1449	30	1.7070	2.0	(-4 0 4)	53.648	26.824	0.2929	
10	3.2500	74.0	(-1 2 4)	27.420	13.710	0.1538	31	1.6500	30.0	(2 1 10)	55.658	27.829	0.3030	
11	3.1100	98.0	(-1 0 6)	28.680	14.340	0.1608	32	1.6470	30.0	(3 2 1)	55.768	27.884	0.3036	
12	2.9640	7.0	(0 2 4)	30.126	15.063	0.1687	33	1.6010	6.0	(-4 0 6)	57.518	28.759	0.3123	
13					16.364	0.1829	34	1.5780	29.0	(4 1 0)	58.436	29.218	0.3169	
14					16.924	0.1890	35	1.5610	22.0	(-5 1 2)	59.136	29.568	0.3203	
15					17.983	0.2004	36	1.5100	9.0	(-1-4 4)	61.344	30.672	0.3311	
16					18.434	0.2053	37	1.4950	5.0	(-2-3 6)	62.027	31.013	0.3344	
17					18.576	0.2068	38	1.4800	7.0	(-4 0 8)	62.726	31.363	0.3378	
18	2.1970	14.0	(-2 1 8)	41.049	20.524	0.2276	39	1.4590	24.0	(3-1 12)	63.734	31.867	0.3427	
19	2.1840	6.0	(-3 0 4)	41.304	20.652	0.2289	40	1.4350	5.0	(1 4 6)	64.929	32.465	0.3484	
20	2.1430	24.0	(-2 3 6)	42.132	21.066	0.2333	41	1.3960	4.0	(-3-2 8)	66.978	33.489	0.3582	
21	2.0680	3.0	(0 0 10)	43.737	21.868	0.2418								

Figure 5.13. JCPDS 44-0673, ZHS*4H₂O standard PDF card.

PDF#39-0689: QM=Common(+); d=Diffractometer; I=(Unknown)												PDF Card	
Zinc Sulfate Hydroxide Hydrate Zn4SO4(OH)6I3H2O													
Radiation=CuKα1				Lambda=1.5406				Filter=					
Calibration=				2θ=9.512-64.879				I/Ic(RIR)=					
Ref: Level-1 PDF													
Triclinic, I-1(2)								Z=4		mp=			
CELL: 8.367 x 8.393 x 18.569 <90.29 x 89.71 x 120.53>								P.S=					
Density(c)=3.03		Density(m)=		Mwt=		Vol=1123.2							
Ref: Ibid.													
Strong Lines: 3.30/X 9.29/X 4.64/X 3.10/5 2.49/5 3.48/5 2.73/4 1.60/3													
61 Lines, Wavelength to Compute Theta = 1.54056?(Cu), I%-Type = (Unknown)													
#	d(?)	I(f)	(h k l)	2-Theta	Theta	1/(2d)	#	d(?)	I(f)	(h k l)	2-Theta	Theta	1/(2d)
1	9.2900	100.0	(0 0 2)	9.512	4.756	0.0538	32	2.1440	2.0	(-3 3 4)	42.111	21.056	0.2332
2	6.7400	20.0	(0 1 1)	13.125	6.562	0.0742	33	2.0920	1.0	(-4 2 0)	43.210	21.605	0.2390
3	5.7400	5.0	(1 -1 2)	15.424	7.712	0.0871	34	2.0540	9.0	(3 -1 6)	44.050	22.025	0.2434
4	4.6400	95.0	(0 0 4)	19.112	9.556	0.1078	35	2.0440	9.0	(-3 1 6)	44.277	22.139	0.2446
5	4.1700	7.0	(1 1 0)	21.290	10.645	0.1199	36	2.0220	8.0	(0 -3 5)	44.785	22.393	0.2473
6	4.1100	5.0	(1 -2 1)	21.604	10.802	0.1217	37	1.9990	1.0	(1 3 0)	45.329	22.664	0.2501
7	4.0800	5.0	(-2 1 1)	21.765	10.882	0.1225	38	1.9160	9.0	(2 -4 4)	47.410	23.705	0.2610
8	3.9300	8.0	(1 -1 4)	22.606	11.303	0.1272	39	1.9090	9.0	(-2 4 4)	47.594	23.797	0.2619
9	3.8000	4.0	(-1 -1 2)	23.390	11.695	0.1316	40	1.9040	24.0	(-2 3 7)	47.727	23.863	0.2626
10	3.6200	3.0	(0 2 0)	24.571	12.286	0.1381	41	1.9000	24.0	(1 2 7)	47.834	23.917	0.2632
11	3.4800	49.0	(2 -1 3)	25.576	12.788	0.1437	42	1.8560	16.0	(0 0 10)	49.041	24.521	0.2694
12	3.3000	100.0	(-1 0 5)	26.997	13.498	0.1515	43	1.7970	7.0	(-1 1 10)	50.764	25.382	0.2782
13	3.1000	52.0	(-1 -1 4)	28.775	14.387	0.1613	44	1.7720	22.0	(1 -4 5)	51.532	25.766	0.2822
14					15.641	0.1750	45	1.7670	22.0	(-3 1 8)	51.688	25.844	0.2830
15					16.056	0.1795	46	1.6810	7.0	(3 1 6)	54.546	27.273	0.2974
16					16.376	0.1830	47	1.6790	7.0	(-4 0 4)	54.616	27.308	0.2978
17					16.557	0.1850	48	1.6530	17.0	(2 -3 9)	55.549	27.774	0.3025
18					16.608	0.1855	49	1.6450	17.0	(-2 3 9)	55.842	27.921	0.3040
19					16.977	0.1895	50	1.6050	32.0	(1 -4 7)	57.361	28.681	0.3115
20					17.104	0.1909	51	1.6020	32.0	(-4 3 7)	57.478	28.739	0.3121
21					17.798	0.1984	52	1.5840	25.0	(-4 5 1)	58.194	29.097	0.3157
22					18.028	0.2009	53	1.5800	25.0	(-5 4 1)	58.355	29.178	0.3165
23					18.481	0.2058	54	1.5660	25.0	(-4 -1 1)	58.928	29.464	0.3193
24					18.884	0.2101	55	1.5620	25.0	(0 -4 6)	59.094	29.547	0.3201
25					19.134	0.2128	56	1.5600	25.0	(1 -5 2)	59.177	29.589	0.3205
26	2.2440	6.0	(3 0 3)	40.151	20.076	0.2228	57	1.5470	6.0	(0 0 12)	59.725	29.862	0.3232
27	2.2370	4.0	(-2 1 7)	40.283	20.141	0.2235	58	1.5410	17.0	(4 -5 3)	59.981	29.991	0.3245
28	2.2180	14.0	(2 -3 5)	40.643	20.321	0.2254	59	1.5370	17.0	(3 -1 10)	60.153	30.077	0.3253
29	2.2120	14.0	(3 -2 5)	40.758	20.379	0.2260	60	1.4430	15.0	(2 -3 11)	64.526	32.263	0.3465
30	2.1960	17.0	(1 2 5)	41.068	20.534	0.2277	61	1.4360	17.0	(-2 3 11)	64.879	32.439	0.3482
31	2.1500	2.0	(3 -3 4)	41.988	20.994	0.2326							

Figure 5.14. JCPDS 39-0689, ZHS*3H₂O standard PDF card.

PDF#89-4252: QM=Calculated; d=Calculated; I=(Unknown)												PDF Card	
Manganese													
Mn													
Radiation=CuKa1				Lambda=1.5406				Filter=					
Calibration=				2T=14.041-89.198				I/Ic(RIR)=5.19					
Ref: Level-1 PDF													
Cubic, I-43m(217)										Z=58		mp=	
CELL: 8.9125 x 8.9125 x 8.9125 <90.0 x 90.0 x 90.0>										P,S=			
Density(c)=7.44		Density(m)=		Mwt=		Vol=707.9							
Ref: Ibid.													
Strong Lines: 2.10/X 1.90/2 1.21/2 1.75/1 1.82/1 1.26/1													
31 Lines, Wavelength to Compute Theta = 1.54056?(Cu), I%-Type = (Unknown)													
#	d(?)	I(f)	(h k l)	2-Theta	Theta	1/(2d)	#	d(?)	I(f)	(h k l)	2-Theta	Theta	1/(2d)
1	6.3021	0.1	(1 1 0)	14.041	7.021	0.0793	17	1.4854	0.9	(6 0 0)	62.471	31.236	0.3366
2	4.4563	0.1	(2 0 0)	19.908	9.954	0.1122	18	1.4458	0.9	(6 1 1)	64.386	32.193	0.3458
3	3.6385	0.7	(2 1 1)	24.444	12.222	0.1374	19	1.4092	0.2	(6 2 0)	66.270	33.135	0.3548
4	3.1511	0.9	(2 2 0)	28.299	14.149	0.1587	20	1.3752	0.1	(5 4 1)	68.127	34.063	0.3636
5	2.8184	0.2	(3 1 0)	31.722	15.861	0.1774	21	1.3436	1.5	(6 2 2)	69.960	34.980	0.3721
6	2.5728	0.9	(2 2 2)	34.842	17.421	0.1943	22	1.3141	0.5	(6 3 1)	71.772	35.886	0.3805
7	2.3820	0.9	(3 2 1)	37.735	18.867	0.2099	23	1.2864	3.9	(4 4 4)	73.566	36.783	0.3887
8	2.2281	4.1	(4 0 0)	40.450	20.225	0.2244	24	1.2604	5.1	(5 5 0)	75.342	37.671	0.3967
9	2.1007	100.0	(4 1 1)	43.022	21.511	0.2380	25	1.2359	0.1	(6 4 0)	77.105	38.553	0.4046
10	1.9929	0.1	(4 2 0)	45.475	22.738	0.2509	26	1.2128	16.4	(7 2 1)	78.855	39.428	0.4123
11	1.9001	22.7	(3 3 2)	47.830	23.915	0.2631	27	1.1910	2.7	(6 4 2)	80.596	40.298	0.4198
12	1.8193	8.4	(4 2 2)	50.099	25.050	0.2748	28	1.1703	1.4	(7 3 0)	82.327	41.163	0.4273
13	1.7479	12.7	(4 3 1)	52.296	26.148	0.2861	29	1.1319	2.4	(6 5 1)	85.769	42.885	0.4417
14	1.6272	0.9	(5 2 1)	56.508	28.254	0.3073	30	1.1141	0.1	(8 0 0)	87.485	43.742	0.4488
15	1.5755	0.3	(4 4 0)	58.537	29.269	0.3174	31	1.0970	0.8	(7 4 1)	89.198	44.599	0.4558
16	1.5285	0.5	(4 3 3)	60.524	30.262	0.3271							

Figure 5.15 JCPDS 89-4252 Mn standard PDF card.

PDF#24-1133: QM=Common(+); d=Diffractometer; I=(Unknown)												PDF Card	
Hetaerolite, syn ZnMn ₂ O ₄													
Radiation=CuKα1				Lambda=1.5406				Filter=					
Calibration=				2θ=18.201-104.681				I/Ic(RIR)=2.7					
Ref. Level-1 PDF													
Tetragonal, I41/amd(141)										Z=4		mp=	
CELL: 5.7204 x 5.7204 x 9.245 <90.0 x 90.0 x 90.0>										P.S=			
Density(c)=5.18		Density(m)=		Mwt=		Vol=302.5							
Ref. Ibid.													
Strong Lines: 2.47/X 2.71/7 3.05/5 1.52/4 1.56/3 2.86/2 1.43/2 2.02/2													
40 Lines, Wavelength to Compute Theta = 1.54056?(Cu), I%-Type = (Unknown)													
#	d(?)	I(f)	(h k l)	2-Theta	Theta	1/(2d)	#	d(?)	I(f)	(h k l)	2-Theta	Theta	1/(2d)
1	4.8700	10.0	(1 0 1)	18.201	9.101	0.1027	21	1.2944	2.0	(3 3 2)	73.038	36.519	0.3863
2	3.0470	45.0	(1 1 2)	29.286	14.643	0.1641	22	1.2790	2.0	(4 2 0)	74.063	37.031	0.3909
3					15.613	0.1747	23	1.2652	9.0	(4 1 3)	75.009	37.504	0.3952
4					16.482	0.1842	24	1.2328	4.0	(4 2 2)	77.338	38.669	0.4056
5					18.202	0.2028	25	1.2161	3.0	(4 0 4)	78.603	39.302	0.4112
6					18.465	0.2056	26	1.2043	1.0	(3 2 5)	79.525	39.763	0.4152
7					19.470	0.2164	27	1.1733	5.0	(3 1 6)	82.068	41.034	0.4261
8	2.0220	16.0	(2 2 0)	44.785	22.393	0.2473	28	1.1553	3.0	(0 0 8)	83.631	41.816	0.4328
9	1.7980	7.0	(2 0 4)	50.733	25.367	0.2781	29	1.1351	2.0	(4 3 1)	85.469	42.734	0.4405
10	1.7600	15.0	(1 0 5)	51.909	25.955	0.2841	30	1.1192	2.0	(4 2 4)	86.982	43.491	0.4467
11	1.6840	12.0	(3 1 2)	54.440	27.220	0.2969	31	1.1100	5.0	(4 1 5)	87.887	43.943	0.4505
12	1.6210	9.0	(3 0 3)	56.743	28.372	0.3085	32	1.0901	3.0	(5 1 2)	89.920	44.960	0.4587
13	1.5640	25.0	(3 2 1)	59.011	29.505	0.3197	33	1.0725	6.0	(4 3 3)	91.814	45.907	0.4662
14	1.5220	40.0	(2 2 4)	60.808	30.404	0.3285	34	1.0553	2.0	(5 2 1)	93.759	46.879	0.4738
15	1.4390	4.0	(1 1 6)	64.727	32.363	0.3475	35	1.0150	5.0	(3 2 7)	98.734	49.367	0.4926
16	1.4299	17.0	(4 0 0)	65.190	32.595	0.3497	36	1.0113	6.0	(1 0 9)	99.224	49.612	0.4944
17	1.4105	2.0	(3 2 3)	66.200	33.100	0.3545	37	1.0043	3.0	(5 2 3)	100.167	50.084	0.4979
18	1.3721	1.0	(4 1 1)	68.304	34.152	0.3644	38	1.0031	2.0	(2 2 8)	100.331	50.166	0.4985
19	1.3565	2.0	(2 0 6)	69.200	34.600	0.3686	39	0.9842	2.0	(4 2 6)	103.007	51.503	0.5080
20	1.3273	4.0	(3 0 5)	70.948	35.474	0.3767	40	0.9730	5.0	(4 3 5)	104.681	52.340	0.5139

Figure 5.16 JCPDS 24-1113, hetaerolite ZnMn₂O₄ standard PDF card.

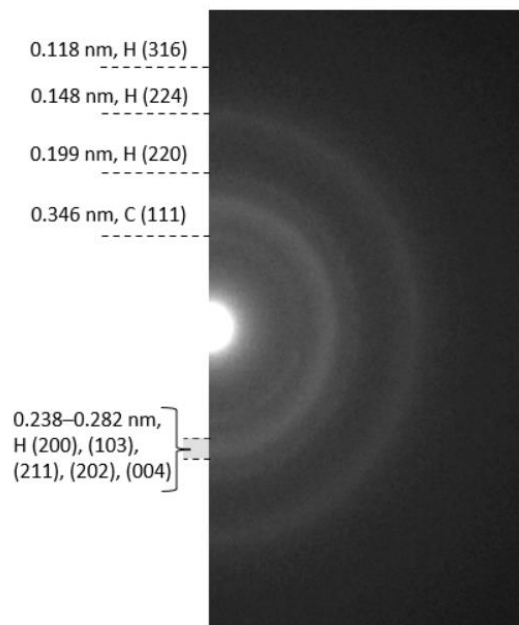


Figure 5.17 Indexing of the SAED pattern in Fig. 5.4a.

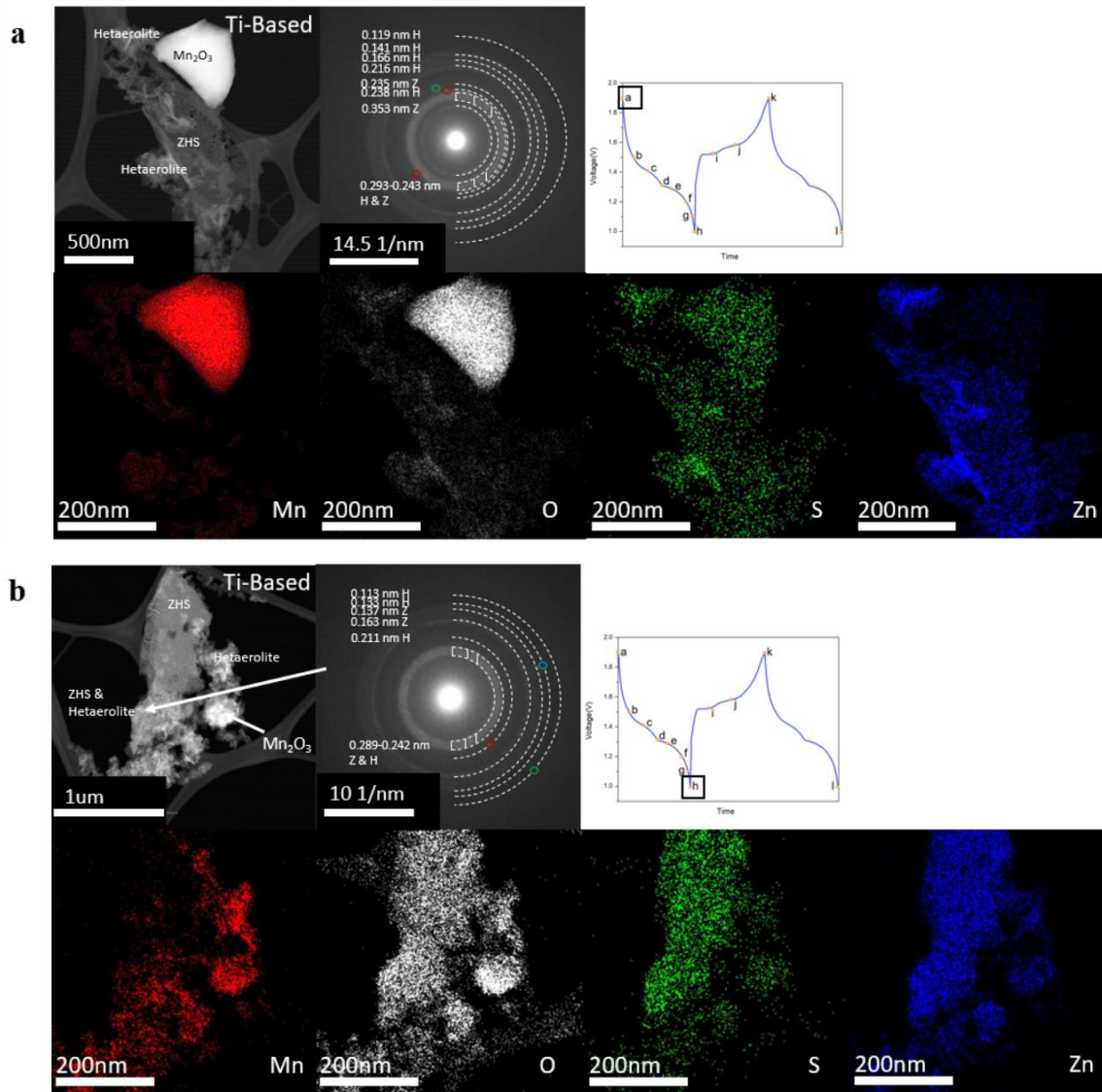


Figure 5.18 Ex-situ STEM ADF images, EDS maps, and SAED patterns of the electrode with a Ti current collector at different stages of discharge and charge: (a) Fully charged stage of the 16th cycle (position a). (b) Fully discharged state of the 15th cycle (position h).

Chapter 6: Conclusions and Recommendations

6.1 Conclusions

This thesis presents work on the synthesis highly crystalline Mn oxide, i.e., Mn_3O_4 and Mn_2O_3 . The synthesized Mn oxide was then used to develop high performing cathode materials for aZIBs and to investigate the discharge/charge mechanism(s) associated with Mn_2O_3 .

6.1.1 Synthesis method and products

- The synthesis method was based on the technique used to synthesize cathode materials for LIBs and SIBs established by the author's previous study. Mn oxide precursors were prepared by precipitation. The final product was formulated by high-temperature calcination of the precursor precipitate. The final product was characterized using multiple characterization methods. The final product depended on the calcination temperature, with hausmannite Mn_3O_4 (0 – 600 °C), bixbyite Mn_2O_3 (700 – 900 °C), or a mixture of Mn_3O_4 and Mn_2O_3 (1000 °C) generated.
- Both hausmannite Mn_3O_4 and bixbyite Mn_2O_3 were highly crystalline and were tested as candidates for the cathode in aZIBs. After preliminary testing, further investigation focused on Mn_2O_3 .

6.1.2 Charge storage mechanism and cycling performance of Mn_2O_3

- Electrodes were prepared by uniformly spreading a slurry, containing Mn_2O_3 (70 wt%), acetylene carbon (20 wt%), and polyvinylidene fluoride (pVdF, 10 wt%) as the binder, on a graphite carbon current collector. CR2032 coin cells were assembled in air using the Mn_2O_3 composite as the cathode, Zn foil as the anode, Whatman glass fiber paper (GF/D) as the separator, and 2 M ZnSO_4 with 0.2 M MnSO_4 aqueous solution as the electrolyte. Cyclic voltammetry (CV) and galvanostatic charge/discharge (GCD) profiles were obtained from 1 V to 1.9 V vs Zn/Zn^{2+} at multiple scan rates and current densities. The

electrode delivered discharge capacities of 375, 341, 289, 205, 113, and 65 mAh/g at 50, 100, 200, 500, 1000, and 2000 mA/g, respectively.

- A new energy storage mechanism for bixbyite Mn_2O_3 was proposed in this work. Microstructural analysis, using x-ray diffraction (XRD) and electron microscopy, showed that intercalation of either Zn^{2+} or H^+ in Mn_2O_3 may occur to some extent but is not the principal mechanism during discharge. Instead, the mechanism proposed here involves two chemical conversion reactions resulting in the formation of hetaerolite (ZnMn_2O_4) during the 1st discharge plateau followed by ZHS formation during the 2nd discharge plateau. Capacity fading during cycling of the Mn_2O_3 electrode was linked to Mn_2O_3 dissolution and incomplete reversibility of the hetaerolite reaction.

6.2 Future Work and Recommendations

6.2.1 Synthesis method and products

- Due to the temperature and environment limitations of the furnace in Ivey's research group, calcination can only be done in air and the highest temperature for the furnace is 1000°C. The synthesis method presented in this thesis has the potential to form other Mn oxide phases in other gas environments and/or at higher temperatures.
- The highly crystalline Mn_3O_4 powder could be further investigated as a cathode material of aZIBs.

6.2.2 Charge storage mechanism and cycling performance of Mn_2O_3

- Due to poor crystallinity and peak overlap with other known phases, identification of the hetaerolite phase formed during the first discharge plateau was difficult by XRD. A synchrotron XRD system, such as the one at the Canadian Light Source (CLS) could provide better patterns and facilitate hetaerolite identification. Because of their high monochromatic radiation flux and highly collimated beams, synchrotron XRD systems have high signal/noise ratios and high angular resolution, which allow for the analysis of complex structural details and peak broadening effects.

- The electrolyte utilized in this work was 2 M ZnSO_4 with 0.2 M MnSO_4 . According to the Pourbaix diagram mentioned in Section 5.3, the concentration of the ZnSO_4 could affect the electrolyte's pH value, which would change the conditions for forming hetaerolite. In future studies, adjusting the ZnSO_4 concentration could provide further insight into the relationship between electrolyte concentration and charge storage mechanism.
- The main purpose of MnSO_4 in the electrolyte is to reduce Mn oxide dissolution during battery operation. From this study, Mn oxide dissolution is critical to producing OH^- to form ZHS and to provide chemical "storage" of Zn^{2+} on the electrode surface instead of intercalation of Zn ions inside the electrode structure. Further study could be done to investigate the effect of MnSO_4 concentration (including no MnSO_4) on Mn oxide dissolution and battery performance.
- RRDE tests were performed on the as-prepared Mn_2O_3 powder. The initial potential used was the system's open-circuit voltage (OCV), ~ 1.4 V. During LSV testing (discharging the electrode), the reaction products were swept to the outer ring electrode by rotation of the motor. The RRDE setup only used a tiny amount of the Mn_2O_3 powder so that most of the Mn_2O_3 powder was consumed by the reaction during the LSV test. As a result, the reaction could not be reversed even if the electrode potential was reversed. In future investigations, a method of recharging the discharged powder could be developed to generate a full discharge LSV curve and reveal more details of the Mn oxide dissolution reaction.

References

1. McDuffie, E. E.; Martin, R. V.; Spadaro, J. V.; Burnett, R.; Smith, S. J.; O'Rourke, P.; Hammer, M. S.; Donkelaar, A. V.; Bindle, L.; Shah, V.; Jaeglé, L.; Luo, G.; Yu, F.; Adeniran, J. A.; Lin, J.; Brauer, M. Source Sector and Fuel Contributions to Ambient PM_{2.5} and Attributable Mortality Across Multiple Spatial Scales. *Nature Communications* **2021**, *12* (1).
2. Shaqsi, A. Z. A.; Sopian, K.; Al-Hinai, A. Review of Energy Storage Services, Applications, Limitations, and Benefits. *Energy Reports* **2020**, *6*, 288–306.
3. Alias, N.; Mohamad, A. A. Advances of Aqueous Rechargeable Lithium-Ion Battery: A Review. *Journal of Power Sources* **2015**, *274*, 237–251
4. Kim, T.; Song, W.; Son, D.-Y.; Ono, L. K.; Qi, Y. Lithium-Ion Batteries: Outlook on Present, Future, and Hybridized Technologies. *Journal of Materials Chemistry A* **2019**, *7* (7), 2942–2964.
5. Maeda, K.; Nogami, M.; Arafune, K.; Yamamoto, T.; Itoh, K.; Fukui, K.; Kuramochi, H. Application of Industrial Crystallization Model for Charge–Discharge Cycle of Lead–Acid Batteries at High Pressure. *Journal of Chemical Engineering of Japan* **2015**, *48* (10), 815–820.
6. Yazvinskaya, N. N.; Galushkin, D. N.; Isaev, I. R. Probability of Thermal Runaway in High-Capacity Nickel-Cadmium Batteries with Pocket Electrodes. *IOP Conference Series: Materials Science and Engineering* **2021**, *1029*, 012091.
7. Ono, K. Energetically Self-Sustaining Electric Power Generation System Based on the Combined Cycle of Electrostatic Induction Hydrogen Electrolyzer and Fuel Cell. *Electrical Engineering in Japan* **2015**, *195* (1), 10–23.
8. Kim, H.; Hong, J.; Park, K.-Y.; Kim, H.; Kim, S.-W.; Kang, K. Aqueous Rechargeable Li and Na Ion Batteries. *Chemical Reviews* **2014**, *114* (23), 11788–11827.
9. May, G. J.; Davidson, A.; Monahov, B. Lead Batteries for Utility Energy Storage: A Review. *Journal of Energy Storage* **2018**, *15*, 145–157.
10. Jeyaseelan, C.; Jain, A.; Khurana, P.; Kumar, D.; Thatai, S. Ni-Cd Batteries. *Rechargeable Batteries* **2020**, 177–194.
11. Linden, D.; Reddy, T. B. *Handbook of Batteries*; McGraw-Hill: New York, 2002.
12. Zhang, Y.; Bai, W.; Cheng, X.; Ren, J.; Weng, W.; Chen, P.; Fang, X.; Zhang, Z.; Peng, H. Flexible and Stretchable Lithium-Ion Batteries and Supercapacitors Based on Electrically Conducting Carbon Nanotube Fiber Springs. *Angewandte Chemie International Edition* **2014**, *53* (52), 14564–14568.
13. Yang, C.; Ji, X.; Fan, X.; Gao, T.; Suo, L.; Wang, F.; Sun, W.; Chen, J.; Chen, L.; Han, F.; Miao, L.; Xu, K.; Gerasopoulos, K.; Wang, C. Flexible Aqueous Li-Ion Battery with High Energy and Power Densities. *Advanced Materials* **2017**, *29* (44), 1701972.
14. Trahey, L.; Brushett, F. R.; Balsara, N. P.; Ceder, G.; Cheng, L.; Chiang, Y.-M.; Hahn, N. T.; Ingram, B. J.; Minter, S. D.; Moore, J. S.; Mueller, K. T.; Nazar, L. F.; Persson, K. A.; Siegel, D. J.; Xu, K.; Zavadil, K. R.; Srinivasan, V.; Crabtree, G. W. Energy Storage Emerging: A Perspective from the Joint Center for Energy Storage Research. *Proceedings of the National Academy of Sciences* **2020**, *117* (23), 12550–12557.
15. Armand, M.; Tarascon, J.-M. Building Better Batteries. *Nature* **2008**, *451* (7179), 652–657.

16. Lukatskaya, M. R.; Feldblyum, J. I.; Mackanic, D. G.; Lissel, F.; Michels, D. L.; Cui, Y.; Bao, Z. Concentrated Mixed Cation Acetate “Water-in-Salt” Solutions as Green and Low-Cost High Voltage Electrolytes for Aqueous Batteries. *Energy & Environmental Science* **2018**, *11* (10), 2876–2883.
17. “Water-in-Salt” Electrolyte Enabled High Voltage Aqueous Li-Ion Chemistries. *ECS Meeting Abstracts* **2016**. YAN J, WANG J, LIU H, et al Rechargeable hybrid aqueous batteries. *Journal of Power Sources*, 2012, 216: 222–226.
18. Li, W.; Dahn, J. R.; Wainwright, D. S. Rechargeable Lithium Batteries with Aqueous Electrolytes. *Science* **1994**, *264* (5162), 1115–1118.
19. Suo, L.; Borodin, O.; Gao, T.; Olguin, M.; Ho, J.; Fan, X.; Luo, C.; Wang, C.; Xu, K. “Water-in-Salt” Electrolyte Enables High-Voltage Aqueous Lithium-Ion Chemistries. *Science* **2015**, *350* (6263), 938–943.
20. Suo, L.; Borodin, O.; Wang, Y.; Rong, X.; Sun, W.; Fan, X.; Xu, S.; Schroeder, M. A.; Cresce, A. V.; Wang, F.; Yang, C.; Hu, Y.-S.; Xu, K.; Wang, C. “Water-in-Salt” Electrolyte Makes Aqueous Sodium-Ion Battery Safe, Green, and Long-Lasting. *Advanced Energy Materials* **2017**, *7* (21), 1701189.
21. Liu, J.; Kan, W. H.; Ling, C. D. Insights into the High Voltage Layered Oxide Cathode Materials in Sodium-Ion Batteries: Structural Evolution and Anion Redox. *Journal of Power Sources* **2021**, *481*, 229139.
22. Sun, Y.; Shi, P.; Chen, J.; Wu, Q.; Liang, X.; Rui, X.; Xiang, H.; Yu, Y. Development and Challenge of Advanced Nonaqueous Sodium Ion Batteries. *EnergyChem* **2020**, *2* (2), 100031.
23. Wu, W.; Mohamed, A.; Whitacre, J. F. Microwave Synthesized NaTi₂(PO₄)₃ as an Aqueous Sodium-Ion Anode. *Journal of The Electrochemical Society* **2013**, *160* (3).
24. Wu, W.; Yan, J.; Wise, A.; Rutt, A.; Whitacre, J. F. Using Intimate Carbon to Enhance the Performance of NaTi₂(PO₄)₃ Anode Materials: Carbon Nanotubes vs Graphite. *Journal of The Electrochemical Society* **2014**, *161* (4).
25. Wessells, C. D.; Huggins, R. A.; Cui, Y. Copper Hexacyanoferrate Battery Electrodes with Long Cycle Life and High Power. *Nature Communications* **2011**, *2* (1).
26. Wessells, C. D.; Peddada, S. V.; Huggins, R. A.; Cui, Y. Nickel Hexacyanoferrate Nanoparticle Electrodes For Aqueous Sodium and Potassium Ion Batteries. *Nano Letters* **2011**, *11* (12), 5421–5425.
27. Wessells, C. D.; McDowell, M. T.; Peddada, S. V.; Pasta, M.; Huggins, R. A.; Cui, Y. Tunable Reaction Potentials in Open Framework Nanoparticle Battery Electrodes for Grid-Scale Energy Storage. *ACS Nano* **2012**, *6* (2), 1688–1694.
28. Su, D.; McDonagh, A.; Qiao, S.-Z.; Wang, G. High-Capacity Aqueous Potassium-Ion Batteries for Large-Scale Energy Storage. *Advanced Materials* **2016**, *29* (1), 1604007.
29. Aurbach, D.; Lu, Z.; Schechter, A.; Gofer, Y.; Gizbar, H.; Turgeman, R.; Cohen, Y.; Moshkovich, M.; Levi, E. Prototype Systems for Rechargeable Magnesium Batteries. *Nature* **2000**, *407* (6805), 724–727.
30. Shuai, H.; Xu, J.; Huang, K. Progress in Retrospect of Electrolytes for Secondary Magnesium Batteries. *Coordination Chemistry Reviews* **2020**, *422*, 213478.
31. Huie, M. M.; Bock, D. C.; Takeuchi, E. S.; Marschilok, A. C.; Takeuchi, K. J. Cathode Materials for Magnesium and Magnesium-Ion Based Batteries. *Coordination Chemistry Reviews* **2015**, *287*, 15–27.

32. Mohtadi, R.; Tutusaus, O.; Arthur, T. S.; Zhao-Karger, Z.; Fichtner, M. The Metamorphosis of Rechargeable Magnesium Batteries. *Joule* **2021**.
33. Sun, X.; Duffort, V.; Mehdi, B. L.; Browning, N. D.; Nazar, L. F. Investigation of the Mechanism of Mg Intercalation in Birnessite in Nonaqueous and Aqueous Rechargeable Mg-Ion Batteries. *Chemistry of Materials* **2016**, *28* (2), 534–542.
34. Rashad, M.; Asif, M.; Ahmed, I.; He, Z.; Yin, L.; Wei, Z. X.; Wang, Y. Quest for Carbon and Vanadium Oxide Based Rechargeable Magnesium-Ion Batteries. *Journal of Magnesium and Alloys* **2020**, *8* (2), 364–373.
35. Novák, P.; Desilvestro, J. Electrochemical Intercalation of Magnesium in Metal Oxides and Sulfides from Aprotic Electrolytes. *Journal of The Electrochemical Society* **1993**, *140* (1), 140–144.
36. Novák, P.; Scheifele, W.; Joho, F.; Haas, O. Electrochemical Intercalation of Magnesium into Hydrated Vanadium Bronzes. *Journal of The Electrochemical Society* **1995**, *142* (8), 2544–2550.
37. Novák, P.; Scheifele, W.; Haas, O. Magnesium Intercalation Batteries — an Alternative to Lithium? *Journal of Power Sources* **1995**, *54* (2), 479–482.
38. McLarnon, F. R.; Cairns, E. J. The Secondary Alkaline Zinc Electrode. *Journal of The Electrochemical Society* **1991**, *138* (2), 645–656.
39. Kordesh, K.; Weissenbacher, M. Rechargeable Alkaline Manganese Dioxide/Zinc Batteries. *Journal of Power Sources* **1994**, *51* (1-2), 61–78.
40. Lee, B.; Lee, H. R.; Kim, H.; Chung, K. Y.; Cho, B. W.; Oh, S. H. Elucidating the Intercalation Mechanism of Zinc Ions into α -MnO₂ for Rechargeable Zinc Batteries. *Chemical Communication* **2015**, *51*(45), 9265–9268.
41. Wang, K.; Gao, S.; Du, Z.; Yuan, A.; Lu, W.; Chen, L. MnO₂-Carbon Nanotube Composite for High-Areal-Density Supercapacitors with High Rate Performance. *Journal of Power Source* **2016**, *305*, 30–36.
42. Parker, J. F.; Chervin, C. N.; Pala, I. R.; Machler, M.; Burz, M. F.; Long, J. W.; Rolison, D. R. Rechargeable Nickel–3D Zinc Batteries: An Energy-Dense, Safer Alternative to Lithium-Ion. *Science* **2017**, *356* (6336), 415–418.
43. Lee, B.; Seo, H. R.; Lee, H. R.; Yoon, C. S.; Kim, J. H.; Chung, K. Y.; Cho, B. W.; Oh, S. H. Critical Role of PH Evolution of Electrolyte in the Reaction Mechanism for Rechargeable Zinc Batteries. *ChemSusChem* **2016**, *9* (20), 2948–2956.
44. Kumar, G. Electrochemical Characterization of Poly(Vinylidene fluoride)-Zinc Triflate Gel Polymer Electrolyte and Its Application in Solid-State Zinc Batteries. *Solid State Ionics* **2003**, *160* (3-4), 289–300.
45. Li, G.; Yang, Z.; Jiang, Y.; Jin, C.; Huang, W.; Ding, X.; Huang, Y. Towards Polyvalent Ion Batteries: A Zinc-Ion Battery Based on NASICON Structured Na₃V₂(PO₄)₃. *Nano Energy* **2016**, *25*, 211–217.
46. Liu, Z.; Bertram, P.; Endres, F. Bio-Degradable Zinc-Ion Battery Based on a Prussian Blue Analogue Cathode and a Bio-Ionic Liquid-Based Electrolyte. *Journal of Solid State Electrochemistry* **2017**, *21* (7), 2021–2027.
47. Liu, Z.; Pulletikurthi, G.; Endres, F. A Prussian Blue/Zinc Secondary Battery with a Bio-Ionic Liquid–Water Mixture as Electrolyte. *ACS Applied Materials & Interfaces* **2016**, *8* (19), 12158–12164.

48. Wei, C.; Xu, C.; Li, B.; Du, H.; Kang, F. Preparation and Characterization of Manganese Dioxides with Nano-Sized Tunnel Structures for Zinc Ion Storage. *Journal of Physics and Chemistry of Solids* **2012**, *73* (12), 1487–1491.
49. Song, M.; Tan, H.; Chao, D.; Fan, H. J. Recent Advances in Zn-Ion Batteries. *Advanced Functional Materials* **2018**, *28* (41), 1802564.
50. Kumar, G. Electrochemical Characterization of Poly(Vinylidene fluoride)-Zinc Triflate Gel Polymer Electrolyte and Its Application in Solid-State Zinc Batteries. *Solid State Ionics* **2003**, *160* (3-4), 289–300.
51. Xu, C.; Li, B.; Du, H.; Kang, F. Energetic Zinc Ion Chemistry: The Rechargeable Zinc Ion Battery. *Angewandte Chemie* **2011**, *124* (4), 957–959.
52. Alfaruqi, M. H.; Mathew, V.; Gim, J.; Kim, S.; Song, J.; Baboo, J. P.; Choi, S. H.; Kim, J. Electrochemically Induced Structural Transformation in a γ -MnO₂ Cathode of a High Capacity Zinc-Ion Battery System. *Chemistry of Materials* **2015**, *27* (10), 3609–3620.
53. Xu, C.; Chiang, S. W.; Ma, J.; Kang, F. Investigation on Zinc Ion Storage in Alpha Manganese Dioxide for Zinc Ion Battery by Electrochemical Impedance Spectrum. *Journal of The Electrochemical Society* **2012**, *160* (1).
54. Xu, C.; Du, H.; Li, B.; Kang, F.; Zeng, Y. Reversible Intercalation Properties of Zinc Ion into Manganese Dioxide and Its Application for Energy Storage. *Electrochemical and Solid-State Letters* **2009**, *12* (4).
55. Xu, C.; Li, B.; Du, H.; Kang, F. Energetic Zinc Ion Chemistry: The Rechargeable Zinc Ion Battery. *Angewandte Chemie* **2011**, *124* (4), 957–959.
56. Alfaruqi, M. H.; Gim, J.; Kim, S.; Song, J.; Jo, J.; Kim, S.; Mathew, V.; Kim, J. Enhanced Reversible Divalent Zinc Storage in a Structurally Stable α -MnO₂ Nanorod Electrode. *Journal of Power Sources* **2015**, *288*, 320–327.
57. Lee, B.; Yoon, C. S.; Lee, H. R.; Chung, K. Y.; Cho, B. W.; Oh, S. H. Electrochemically-Induced Reversible Transition from the Tunneled to Layered Polymorphs of Manganese Dioxide. *Scientific Reports* **2014**, *4* (1).
58. Manceau, A.; Drits, V. A.; Silvester, E.; Bartoli, C.; Lanson, B. Structural Mechanism of Co (Super 2) Oxidation by the Phylломanganate Buserite. *American Mineralogist* **1997**, *82* (11-12), 1150–1175.
59. Lee, B.; Seo, H. R.; Lee, H. R.; Yoon, C. S.; Kim, J. H.; Chung, K. Y.; Cho, B. W.; Oh, S. H. Critical Role of pH Evolution of Electrolyte in the Reaction Mechanism for Rechargeable Zinc Batteries. *ChemSusChem* **2016**, *9* (20), 2948–2956.
60. Pan, H.; Shao, Y.; Yan, P.; Cheng, Y.; Han, K. S.; Nie, Z.; Wang, C.; Yang, J.; Li, X.; Bhattacharya, P.; Mueller, K. T.; Liu, J. Reversible Aqueous Zinc/Manganese Oxide Energy Storage from Conversion Reactions. *Nature Energy* **2016**, *1* (5).
61. Zhao, S.; Han, B.; Zhang, D.; Huang, Q.; Xiao, L.; Chen, L.; Ivey, D. G.; Deng, Y.; Wei, W. Unravelling the Reaction Chemistry and Degradation Mechanism in Aqueous Zn/MnO₂ Rechargeable Batteries. *Journal of Materials Chemistry A* **2018**, *6* (14), 5733–5739.
62. Alfaruqi, M. H.; Islam, S.; Gim, J.; Song, J.; Kim, S.; Pham, D. T.; Jo, J.; Xiu, Z.; Mathew, V.; Kim, J. A High Surface Area Tunnel-Type α -MnO₂ Nanorod Cathode by a Simple Solvent-Free Synthesis for Rechargeable Aqueous Zinc-Ion Batteries. *Chemical Physics Letters* **2016**, *650*, 64–68.
63. Lee, J.; Ju, J. B.; Cho, W. I.; Cho, B. W.; Oh, S. H. Todorokite-Type MnO₂ as a Zinc-Ion Intercalating Material. *Electrochimica Acta* **2013**, *112*, 138–143.

64. Tran, T. N.; Jin, S.; Cuisinier, M.; Adams, B. D.; Ivey, D. G. Reaction Mechanisms for Electrolytic Manganese Dioxide in Rechargeable Aqueous Zinc-Ion Batteries. *Scientific Reports* **2021**, *11* (1).
65. Alfaruqi, M. H.; Gim, J.; Kim, S.; Song, J.; Pham, D. T.; Jo, J.; Xiu, Z.; Mathew, V.; Kim, J. A Layered δ -MnO₂ Nanoflake Cathode with High Zinc-Storage Capacities for Eco-Friendly Battery Applications. *Electrochemistry Communications* **2015**, *60*, 121–125.
66. Han, S.-D.; Kim, S.; Li, D.; Petkov, V.; Yoo, H. D.; Phillips, P. J.; Wang, H.; Kim, J. J.; More, K. L.; Key, B.; Klie, R. F.; Cabana, J.; Stamenkovic, V. R.; Fister, T. T.; Markovic, N. M.; Burrell, A. K.; Tepavcevic, S.; Vaughey, J. T. Mechanism of Zn Intercalation into Nanostructured δ -MnO₂: A Nonaqueous Rechargeable Zn Metal Battery. *Chemistry of Materials* **2017**, *29* (11), 4874–4884.
67. Yuan, C.; Zhang, Y.; Pan, Y.; Liu, X.; Wang, G.; Cao, D. Investigation of the Intercalation of Polyvalent Cations (Mg²⁺, Zn²⁺) into λ -MnO₂ for Rechargeable Aqueous Battery. *Electrochimica Acta* **2014**, *116*, 404–412.
68. Zhang, N.; Cheng, F.; Liu, Y.; Zhao, Q.; Lei, K.; Chen, C.; Liu, X.; Chen, J. Cation-Deficient Spinel ZnMn₂O₄ Cathode in Zn(CF₃SO₃)₂ Electrolyte for Rechargeable Aqueous Zn-Ion Battery. *Journal of the American Chemical Society* **2016**, *138* (39), 12894–12901.
69. Islam, S.; Alfaruqi, M. H.; Mathew, V.; Song, J.; Kim, S.; Kim, S.; Jo, J.; Baboo, J. P.; Pham, D. T.; Putro, D. Y.; Sun, Y.-K.; Kim, J. Facile Synthesis and the Exploration of the Zinc Storage Mechanism of β -MnO₂ Nanorods with Exposed (101) Planes as a Novel Cathode Material for High Performance Eco-Friendly Zinc-Ion Batteries. *Journal of Materials Chemistry A* **2017**, *5* (44), 23299–23309.
70. Zhang, N.; Cheng, F.; Liu, J.; Wang, L.; Long, X.; Liu, X.; Li, F.; Chen, J. Rechargeable Aqueous Zinc-Manganese Dioxide Batteries with High Energy and Power Densities. *Nature Communications* **2017**, *8* (1).
71. Hao, J.; Mou, J.; Zhang, J.; Dong, L.; Liu, W.; Xu, C.; Kang, F. Electrochemically Induced Spinel-Layered Phase Transition of Mn₃O₄ in High Performance Neutral Aqueous Rechargeable Zinc Battery. *Electrochimica Acta* **2018**, *259*, 170–178.
72. Dhiman, A.; Ivey, D. G. Electrodeposited Manganese Oxide on Carbon Paper for Zinc-Ion Battery Cathodes. *Batteries & Supercaps* **2019**, *3* (3), 293–305.
73. Jiang, B.; Xu, C.; Wu, C.; Dong, L.; Li, J.; Kang, F. Manganese Sesquioxide as Cathode Material for Multivalent Zinc Ion Battery with High Capacity and Long Cycle Life. *Electrochimica Acta* **2017**, *229*, 422–428.
74. Mao, M.; Wu, X.; Hu, Y.; Yuan, Q.; He, Y.-B.; Kang, F. Charge Storage Mechanism of MOF-Derived Mn₂O₃ as High Performance Cathode of Aqueous Zinc-Ion Batteries. *Journal of Energy Chemistry* **2021**, *52*, 277–283.
75. Feng, D.; Gao, T.-N.; Zhang, L.; Guo, B.; Song, S.; Qiao, Z.-A.; Dai, S. Boosting High-Rate Zinc-Storage Performance by the Rational Design of Mn₂O₃ Nanoporous Architecture Cathode. *Nano-Micro Letters* **2019**, *12* (1).
76. Shen, H.; Liu, B.; Nie, Z.; Li, Z.; Jin, S.; Huang, Y.; Zhou, H. A Comparison Study of MnO₂ and Mn₂O₃ as Zinc-Ion Battery Cathodes: an Experimental and Computational Investigation. *RSC Advances* **2021**, *11* (24), 14408–14414.
77. Ma, Y.; Ma, Y.; Diemant, T.; Cao, K.; Liu, X.; Kaiser, U.; Behm, R. J.; Varzi, A.; Passerini, S. Unveiling the Intricate Intercalation Mechanism in Manganese Sesquioxide as Positive Electrode in Aqueous Zn-Metal Battery. *Advanced Energy Materials* **2021**, *11* (35), 2100962.

78. Yang, S.; Zhang, M.; Wu, X.; Wu, X.; Zeng, F.; Li, Y.; Duan, S.; Fan, D.; Yang, Y.; Wu, X. The Excellent Electrochemical Performances of ZnMn₂O₄/Mn₂O₃: The Composite Cathode Material for Potential Aqueous Zinc Ion Batteries. *Journal of Electroanalytical Chemistry* **2019**, *832*, 69–74.
79. Zhou, Z.; Wang, L.; Liang, J.; Zhang, C.; Peng, W.; Li, Y.; Zhang, G.; Zhang, F.; Fan, X. Two-Dimensional Hierarchical Mn₂O₃@Graphene as a High Rate and Ultrastable Cathode for Aqueous Zinc-Ion Batteries. *Journal of Materials Chemistry C* **2021**, *9* (4), 1326–1332.
80. Wang, J.; Yang, Y.; Zhang, Y.; Li, Y.; Sun, R.; Wang, Z.; Wang, H. Strategies towards the Challenges of Zinc Metal Anode in Rechargeable Aqueous Zinc Ion Batteries. *Energy Storage Materials* **2021**, *35*, 19–46.
81. Chen, R.; Luo, R.; Huang, Y.; Wu, F.; Li, L. Advanced High Energy Density Secondary Batteries with Multi-Electron Reaction Materials. *Advanced Science* **2016**, *3* (10), 1600051.
82. Zhang, X. G. Electrochemistry of Zinc Oxide. *Corrosion and Electrochemistry of Zinc* **1996**, 93–124.
83. Wang, F.; Borodin, O.; Gao, T.; Fan, X.; Sun, W.; Han, F.; Faraone, A.; Dura, J. A.; Xu, K.; Wang, C. Highly Reversible Zinc Metal Anode for Aqueous Batteries. *Nature Materials* **2018**, *17* (6), 543–549.
84. Hu, L.; Xiao, P.; Xue, L.; Li, H.; Zhai, T. The Rising Zinc Anodes for High-Energy Aqueous Batteries. *EnergyChem* **2021**, *3* (2), 100052.
85. Jia, H.; Wang, Z.; Tawiah, B.; Wang, Y.; Chan, C.-Y.; Fei, B.; Pan, F. Recent Advances in Zinc Anodes for High-Performance Aqueous Zn-Ion Batteries. *Nano Energy* **2020**, *70*, 104523.
86. Kundu, D.; Adams, B. D.; Duffort, V.; Vajargah, S. H.; Nazar, L. F. A High-Capacity and Long-Life Aqueous Rechargeable Zinc Battery Using a Metal Oxide Intercalation Cathode. *Nature Energy* **2016**, *1* (10).
87. Yan, J.; Wang, J.; Liu, H.; Bakenov, Z.; Gosselink, D.; Chen, P. Rechargeable Hybrid Aqueous Batteries. *Journal of Power Sources* **2012**, *216*, 222–226.
88. Zuo, Y.; Wang, K.; Pei, P.; Wei, M.; Liu, X.; Xiao, Y.; Zhang, P. Zinc Dendrite Growth and Inhibition Strategies. *Materials Today Energy* **2021**, 100692.
89. Bass, K.; Mitchell, P.; Wilcox, G.; Smith, J. Methods for the Reduction of Shape Change and Dendritic Growth in Zinc-Based Secondary Cells. *Journal of Power Sources* **1991**, *35* (3), 333–351.
90. Hoang Huy, V. P.; Hieu, L. T.; Hur, J. Zn Metal Anodes for Zn-Ion Batteries in Mild Aqueous Electrolytes: Challenges and Strategies. *Nanomaterials* **2021**, *11* (10), 2746.
91. Li, H.; Xu, C.; Han, C.; Chen, Y.; Wei, C.; Li, B.; Kang, F. Enhancement on Cycle Performance of Zn Anodes by Activated Carbon Modification for Neutral Rechargeable Zinc Ion Batteries. *Journal of The Electrochemical Society* **2015**, *162* (8).
92. González, M.; Trócoli, R.; Pavlovic, I.; Barriga, C.; Mantia, F. L. Layered Double Hydroxides as a Suitable Substrate to Improve the Efficiency of Zn Anode in Neutral pH Zn-Ion Batteries. *Electrochemistry Communications* **2016**, *68*, 1–4.
93. Sun, K. E. K.; Hoang, T. K. A.; Doan, T. N. L.; Yu, Y.; Chen, P. Highly Sustainable Zinc Anodes for a Rechargeable Hybrid Aqueous Battery. *Chemistry - A European Journal* **2017**, *24* (7), 1667–1673.

94. Kasiri, G.; Trócoli, R.; Bani Hashemi, A.; La Mantia, F. An Electrochemical Investigation of the Aging of Copper Hexacyanoferrate during the Operation in Zinc-Ion Batteries. *Electrochimica Acta* **2016**, *222*, 74–83.
95. Kasiri, G.; Trócoli, R.; Bani Hashemi, A.; La Mantia, F. An Electrochemical Investigation of the Aging of Copper Hexacyanoferrate during the Operation in Zinc-Ion Batteries. *Electrochimica Acta* **2016**, *222*, 74–83.
96. Ashoka, S.; Chithaiah, P.; Tharamani, C. N.; Chandrappa, G. T. Synthesis and Characterisation of Microstructural α - Mn_2O_3 Materials. *Journal of Experimental Nanoscience* **2010**, *5* (4), 285–293.
97. Mn_2O_3 (cubic, IA-3, 206) <https://materialsproject.org/materials/mp-542877/> (accessed Apr 16, 2022).
98. Mu, L.; Hou, Q.; Yang, Z.; Zhang, Y.; Rahman, M. M.; Kautz, D. J.; Sun, E.; Du, X.-W.; Du, Y.; Nordlund, D.; Lin, F. Water-Processable $\text{P2-Na}_{0.67}\text{Ni}_{0.22}\text{Cu}_{0.11}\text{Mn}_{0.56}\text{Ti}_{0.11}\text{O}_2$ Cathode Material for Sodium Ion Batteries. *Journal of The Electrochemical Society* **2019**, *166* (2).
99. Goldstein, J.; Newbury, D. E.; Joy, D. C.; Lyman, C. E.; Echlin, P.; Lifshin, E.; Sawyer, L.; Michael, J. R. *Scanning Electron Microscopy and X-Ray Microanalysis Third Edition*; Springer US: New York, NY, 2003.
100. Fultz, B.; Howe, J. M. *Transmission Electron Microscopy and Diffractometry of Materials*; Springer: Heidelberg, 2013.
101. Guha, S. Simulation Studies on a Rotating Ring Disk Electrode: Effects of Ionic Migration with Kinetic Complication-Disk Results. *AIChE Journal* **2021**, *68* (3).
102. Jia, Z.; Yin, G.; Zhang, J. Rotating Ring-Disk Electrode Method. *Rotating Electrode Methods and Oxygen Reduction Electrocatalysts* **2014**, 199–229.
103. Guha, S. Simulation Studies on a Rotating Ring Disk Electrode System: Role of Supporting Electrolyte in Determination of Relevance of Ionic Migration. *AIChE Journal* **2012**, *59* (4), 1390–1399.
104. Freedman, J. C. Biophysical Chemistry of Physiological Solutions. *Cell Physiology Source Book* **2012**, 3–17.
105. Hao, J.; Mou, J.; Zhang, J.; Dong, L.; Liu, W.; Xu, C.; Kang, F. Electrochemically Induced Spinel-Layered Phase Transition of Mn_3O_4 in High Performance Neutral Aqueous Rechargeable Zinc Battery. *Electrochimica Acta* **2018**, *259*, 170–178.
106. Guo, X.; Fang, G.; Zhang, W.; Zhou, J.; Shan, L.; Wang, L.; Wang, C.; Lin, T.; Tang, Y.; Liang, S. Mechanistic Insights of Zn^{2+} Storage in Sodium Vanadates. *Advanced Energy Materials* **2018**, *8*(27), 1801819.
107. Zhu, C.; Fang, G.; Zhou, J.; Guo, J.; Wang, Z.; Wang, C.; Li, J.; Tang, Y.; Liang, S. Binder-Free Stainless Steel@ Mn_3O_4 Nanoflower Composite: a High-Activity Aqueous Zinc-Ion Battery Cathode with High-Capacity and Long-Cycle-Life. *Journal of Materials Chemistry A* **2018**, *6*(20), 9677–9683.
108. Mahmud, M.; Huda, N.; Farjana, S.; Lang, C. Comparative Life Cycle Environmental Impact Analysis of Lithium-Ion (Li-Ion) and Nickel-Metal Hydride (NiMH) Batteries. *Batteries* **2019**, *5* (1), 22.
109. Biesinger, M. C.; Payne, B. P.; Grosvenor, A. P.; Lau, L. W.; Gerson, A. R.; Smart, R. S. Resolving Surface Chemical States in XPS Analysis of First Row Transition Metals, Oxides and Hydroxides: Cr, Mn, Fe, Co and Ni. *Applied Surface Science* **2011**, *257* (7), 2717–2730.

110. Ilton, E. S.; Post, J. E.; Heaney, P. J.; Ling, F. T.; Kerisit, S. N. XPS Determination of Mn Oxidation States in Mn (Hydro)Oxides. *Applied Surface Science* **2016**, *366*, 475–485.
111. Rubel, O.; Tran, T. N. T.; Gourley, S.; Anand, S.; Bommel, A. V.; Adams, B. D.; Ivey, D. G.; Higgins, D. Electrochemical stability of ZnMn₂O₄: Understanding Zn-ion rechargeable battery capacity and degradation, *arXiv preprint arXiv:2203.10175* **2022**, <https://doi.org/10.48550/arXiv.2203.10175>.